Doctoral Dissertation

Atomic and Electronic Structures of the Bi-adsorbed and In-adsorbed Si(110) surfaces

（ビスマス及びインジウム吸着Si(110)表面の構造と電子状態の研究）

September 2016

Artoni Kevin Roquero ANG

Graduate School of Materials Science
Nara Institute of Science and Technology

Supervisor: Prof. Hiroshi Daimon

Table of Contents

Chapter 1. Introduction

1.1. Background

The developments and progress made in surface and interface science in the past century has truly been quite remarkable. Initially a sub-set of condensed matter physics, surface and interface physics can now stand on its own as a mature research discipline. The ideas and concepts derived from surface and interface physics now make significant contributions, not only to condensed matter physics, but also to other fields such as microelectronics, catalysis and even corrosion research.

Modern surface science has now expanded to cover a wider range of scientific fields. The experimental techniques used in surface science are now being applied in studying new physics in novel two-dimensional or even one-dimensional materials. For example, since the first reports about the successful isolation of a single layer of graphene [1], countless studies have been done using scanning tunneling microscopy (STM) [2] and angle-resolved photoelectron spectroscopy (ARPES) [3] to study its surface and electronic structures [4]. Several other novel materials are being rigorously studied using these techniques, such as topological insulators [5], Weyl semimetals [6] and various low dimensional material systems [7].

In semiconductor surface and interface science, its long history and development has been tightly connected to the evolution of semiconductor device physics. Since the initial studies on metal-semiconductor contacts in the late 1800s, there has been countless studies done on semiconductor surfaces and interfaces [8, 9]. On silicon surfaces, a huge amount of scientific resources has been spent investigating the fundamental properties of the various surfaces of Si. This rapid growth can be traced to

the immense pressure in the semiconducting industry to improve integrated circuits exponentially, as predicted by the now famous "Moore's law" [10, 11]

The low index Si surfaces have been studied so extensively, that almost everything that needs to be known about them is already known. For example, the atomic structure of the clean Si(111) surface has been so thoroughly investigated that more than 100 atomic positions of the Si(111)7×7 reconstruction were precisely described by the Dimer-Adatom-Stacking fault (DAS) model proposed in 1985 by Takayanagi *et al*. [12]. The electronic structure of this surface has also been completely revealed by ARPES [13] and the nature of the surface states has been identified by scanning tunneling spectroscopy (STS) [9]. The Si(001) surface has also been extensively studied, where the Si(001)2×1 surface can be described by tilted dimers [9]. The electronic structure has also been widely investigated and the nature of the surface states on the band structure has been identified [9, 14].

Aside from the clean Si surfaces, numerous metal-adsorbed Si surfaces have also been shown to exhibit varying surface reconstructions with different properties [8, 9, 15]. Numerous studies on metal-adsorbed Si surfaces have been done to understand the various surface reconstructions [15] and their various physical properties. Different Indium-induced surface reconstructions on the Si(111) surface have showed a one dimensional (1D) metallic surface that undergoes a 1D charge density wave (CDW) driven phase transition at low temperatures [16] and the formation of quantized 2D electronic structures called "hole subbands" [17]. Bismuth adsorption on Si surfaces have shown atomically perfect nanowires on the Si(001) surface [18], thin films with Rashba-type spin splitting [19] and Rashba-type spin splitting on one-dimensional edge states [20] on Si(111).

Despite this breadth of knowledge about Si surfaces, it is surprising to note that there is very little known about the Si(110) surface. Until now, there is still no widely accepted structural model for the Si(110)16×2 surface. Several models have been proposed but none of them can convincingly explain all the available experimental data. After the initial structural studies on the clean Si(110) surface in the late 80's [21], the interest on this surface started decreasing.

The initial diffraction experiments on the Si(110) surface presented conflicting periodicities of the unit cell of the clean Si(110) reconstructed surface. It was only in 1986 that diffraction pattern of an atomically clean Si(110)16×2 pattern was reported [21]. It was later reported that the previous conflicting diffraction patterns were due to Ni-induced reconstructions from small amounts of Ni contamination [22]. Difficulties in preparing the clean Si(110)16×2 surface, the large and complicated 16×2 unit cell, and an overall lack of motivation in studying the Si(110) surface resulted in it being largely ignored. This was followed by sporadic studies about the structures of various metal-adsorbed reconstructions on the Si(110) surface, but the extent of the studies were not as extensive as the studies on the other low index Si surfaces.

Having the lowest field effect electron mobility among the low index Si surfaces, there was little interest on the Si(110) surface from the semiconductor industry, further slowing down the progress on this surface. There were reports showing that the hole mobility on the Si(110) surface is the highest [23, 24], but difficulties in forming high quality oxide films on this surface made it unattractive for FET applications.

Recently however, the tremendous growth in the semiconducting industry has started to slow down. Further scaling down of MOSFET devices has become more difficult as the current devices approach the ~10 nm region [11]. Simply making them

smaller and adding more FETs on the devices would no longer be possible. Several ideas have been proposed and developed to solve the scaling down problem. Such ideas include: non-planar FET structures [25], strained-Si based FETs [26], and the use of different Si orientations. The high hole mobility (Table 1-1) of the Si(110) surface has made it an ideal substrate material for p-channel MOSFET [27, 28, 29, 30].

Table 1-1 . Summary of field-effect mobility of electrons and holes taken at various substrate orientation and current directions obtained at RT [24].

	(100)	**(111)**	**(110)**
μ_{FE} **(electron)** **(cm^2/V·sec)**	~450	~320	~310 ⊥ $[\bar{1}10]$
			~230 ∥ $[\bar{1}10]$
μ_{FE} **(hole)** **(cm^2/V·sec)**	~100	~140	~160 ⊥ $[\bar{1}10]$
			~230 ∥ $[\bar{1}10]$

These new ideas in the semiconductor industry has renewed the interest on the Si(110) surface. This and the recent publication about the preparation method necessary to produce a single domain, well-ordered Si(110)16×2 surface [31] has brought about renewed interest on this surface. Several recent papers have been published studying the surface and electronic structures of the clean and metal-adsorbed Si(110). These studies have provided interesting results on the Si(110) surface such as one-dimensional metallic states on Si(110)2×5-Au [32] and one-dimensional giant Rashba spin-split states on Si(110)"6"×5-Pt [33]. However, there is still a significant lack of experiments on both the clean and metal-adsorbed Si(110) surfaces.

1.2. Objectives and outline of the thesis

Based on the fact the knowledge about the Si(110) surface is very limited in spite of the increased interest in the Si(110) surface as a possible Si(110) MOSFET

material, the purpose of this thesis was set to understand the atomic and electronic structures of the Si(110) surface. The specific objectives of this thesis are three-fold:

1. Determine the nature of the electronic states of the clean Si(110)16×2 surface.

The electronic structure of the Si(110)16×2 surface has been revealed by ARPES by previous reports in the literature. However, the nature of the states in the projected bulk bands has not been fully identified. A full understanding of the origins of these electronic states is important to understand and determine the surface structure of the Si(110)16×2 surface.

2. Investigate the surface and electronic structures of Bi-adsorbed Si(110) surfaces.

Metal adsorption on Si surfaces modifies or creates new electronic structures different from the clean surfaces. Recent interest in developing Si-based spintronic devices [34] has increased the interest on Si surfaces with metals with strong spin-orbit coupling such as bismuth (Bi). Hence, bismuth growth and the different Bi-induced reconstructions on the Si(110) surface were investigated. The electronic properties of these surfaces were investigated using ARPES to see how the adsorbed Bi affects the electronic properties of the surface.

3. Investigate the surface and electronic structures of In-adsorbed Si(110) surfaces.

Indium (In) adsorbed Si surfaces have shown interesting properties such as the formation of hole subband structures. In growth on the Si(110) surface was investigated and the electronic structure of these surfaces will then be investigated by ARPES.

Accomplishing these goals will provide key results in understanding the surface and electronic structures of the Si(110) surfaces.

Outline

Chapter 1 describes the background and motivation of the thesis. Chapter 2, provides a brief overview and a review of the basic principles of the experiments used in this study. Experimental details of the experimental chambers used in this study are also provided in this chapter.

Chapter 3 starts with a detailed review of the Si(110) surface. The ARPES spectra of a well-ordered clean Si(110)16×2 surface will be obtained, scanned across several high symmetry directions. The surface-sensitivity of the electronic states observed by ARPES was investigated by changing the surface reconstruction by the adsorption of various metals. The nature of these states was identified and several proposals about their bonding origins are provided.

In the latter part of this study, the surface and electronic structures of metal-adsorbed Si(110) surfaces were investigated. Chapter 4 provides the first comprehensive study of the surface and electronic structures of Bi-adsorbed Si(110) surfaces. The growth of Bismuth on the Si(110) surface was investigated *in situ* using RHEED. From these results, the first complete phase diagram for the Bi/Si(110) surface with a wide Bi coverage and substrate temperature range was produced. The electronic structures of these surfaces were investigated by ARPES and the corresponding surface states were identified. The RHEED and ARPES results were integrated to propose structural models for the Bi-adsorbed Si(110) surfaces. These models adequately explained the RHEED and ARPES data, and can also be used to describe similar surface reconstructions on the Si(110) adsorbed with different metals.

In chapter 5, attempts to clarify In-induced surface reconstructions on the Si(110) surface were made by *in situ* RHEED study of the growth of indium on the

Si(110) surface. Two surface reconstructions were confirmed by the experiments. The electronic structures of these surfaces were investigated by ARPES and the surface states from these reconstructions were revealed. The In-induced band bending on the surface was also investigated.

The results and conclusions of this thesis are summarized in chapter 5. Future outlook and suggestions for further development are also provided. The findings of this thesis will provide significant contribution in the understanding of clean and metal-adsorbed Si(110).

Chapter 2. Experiments and basic principles

In this chapter, the experiments used in this study are briefly introduced and the fundamental principles behind these experiments will be discussed.

In section 2.1, angle-resolved photoelectron spectroscopy (ARPES) is introduced. The principles behind the photoemission process and the instrumentations required are discussed to give the reader a simple overview.

In section 2.2, reflection high-energy electron diffraction (RHEED) is introduced, and the basic principles behind this experiment were discussed.

Section 2.3 gives an overview of ultra-high vacuum and briefly discusses the main parts of a typical UHV chamber. The UHV chambers used in these experiments are briefly described in this section.

2.1. Angle Resolved Photoelectron Spectroscopy (ARPES)

In this section, the fundamental theory behind angle-resolved photoemission spectroscopy (ARPES), and some overview about the experimental set up will be provided. The discussions in this section are based on *Photoelectron Spectroscopy: Principles and Applications* by Stefan Hüfner [35], and the review articles by Damascelli [36] and Hüfner *et al.* [37], unless specified otherwise.

2.1.1. Angle resolved photoelectron spectroscopy: theory

The photoemission process was first detected in 1887 by Hertz, in a simple experimental set-up where a current was induced by the photoelectrons emitted from a solid upon ultraviolet (UV) irradiation. This was later followed by several more experiments and Einstein's paper on the photoelectron effect where he described the quantum nature of light. When light is incident on a sample, an electron can absorb that

photon and escape from the material. This electron can escape the material with a maximum kinetic energy,

$$E_{kin} = h\upsilon - \phi \qquad (1)$$

where v is the photon frequency, h is Plack's constant (4.135×10^{-15} eV·s). ϕ is the material work function (in eV), which measures the potential barrier at the surface for a valence electron to escape to the vacuum.

Kinetics of photoemission

In a typical photoemission experiment, a monochromatized light source (gas discharge lamps or synchrotron radiation sources) is incident on a sample and electrons are emitted via the photoelectron effect, escape into the vacuum in different directions and are analyzed by an electron analyzer.

The electron analyzer collects these electrons and measures their kinetic energies E_{kin} for a given emission angle. From this information, the wave vector or momentum $\boldsymbol{K} = \boldsymbol{p}/\hbar$ of the photoelectrons *in the vacuum* can be determined. Its magnitude can be given by,

$$K = \frac{\sqrt{2mE_{kin}}}{\hbar} \qquad (2),$$

and the different vector components can be given by,

$$K_x = \frac{1}{\hbar}\sqrt{2mE_{kin}}\sin\theta\cos\varphi \qquad (3),$$

$$K_y = \frac{1}{\hbar}\sqrt{2mE_{kin}}\sin\theta\sin\varphi \qquad (4)$$

$$K_z = \frac{1}{\hbar}\sqrt{2mE_{kin}}\cos\theta \qquad (5)$$

where the x- and y- axis are in-plane directions and the z-axis is out of plane. The geometry of the photoemission process is shown in the schematic diagram in Fig. 2.1.

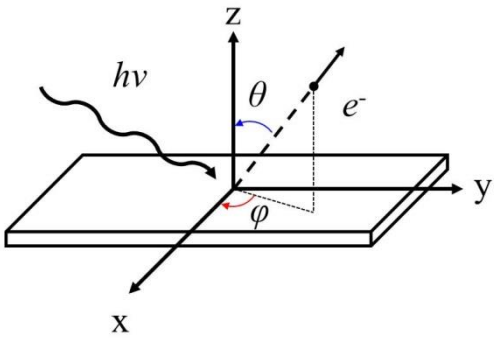

Figure 2.1. Schematic diagram of the geometry of the photoemission process, where in-plane angle φ and out-of-plane angle υ are shown.

The end goal of ARPES is to get the *E(**k**)* dispersion of the electrons *inside* the solid. To get this dispersion information, energy and momentum conservation laws are applied.

In a simple non-interacting electron picture, the energy conservation law can relate the kinetic energy E_{kin} of the electron *in the vacuum* to the binding energy E_B of the electron *inside* the solid. This is shown in the energy diagram in Fig. 2.2, and can be expressed as,

$$E_{kin} = h\upsilon - \phi - |E_B| \qquad (6).$$

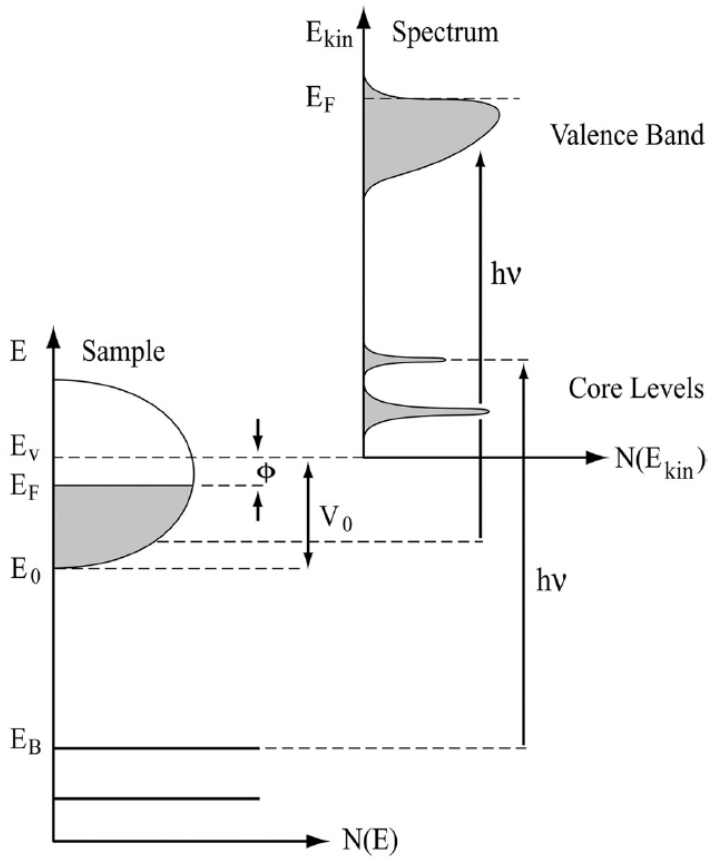

Figure 2.2. Kinetics of the photoemission process. Taken from ref. [36].

Next, by taking advantage of the in-plane (x-y plane) translational symmetry, the parallel component of the electron momentum is conserved in the process.

$$k_{\parallel} = K_{\parallel} = \frac{1}{\hbar}\sqrt{2mE_{kin}}\sin\theta \qquad (7)$$

where $\boldsymbol{k}_{\parallel}$ is the electron crystal momentum in the extended-zone scheme. In most scenarios, the photon momentum is very small compared to the photoelectron momentum and is typically ignored.

In the perpendicular direction, the presence of a surface potential, whose gradient is perpendicular to the surface, means that the perpendicular momentum requires an additional surface potential term,

$$k_{\perp} = \frac{1}{\hbar}\sqrt{2m(E_{kin}\cos^2\theta + V_o)} \qquad (8)$$

where V_0 is the inner potential. To obtain the $k_\perp$ dispersion, the value of V_0 must be obtained. A simple method to achieve this is by experimentally observing the periodicity of $E(\boldsymbol{k}_\perp)$ with varying incident photon energies.

Three step model

The photocurrent produced in a typical photoemission spectroscopy (PES) experiment results from the excitation of an electron in an initial state Ψ_i^N to one of the possible final states Ψ_f^N by a photon with a vector potential $\boldsymbol{A}$. The transition probability ω_{fi} of this excitation can be approximated by Fermi's golden rule:

$$\omega_{fi} = \frac{2\pi}{\hbar}\left|\langle\Psi_f^N|H_{int}|\Psi_i^N\rangle\right|^2 \delta\left(E_f^N - E_i^N - h\upsilon\right) \qquad (9)$$

where $E_i^N = E_i^{N-1} - E_B^k$ and $E_f^N = E_f^{N-1} + E_{kin}$ are the initial- and final-state energies of the N-particle system. The interactions with the photon can be treated as a perturbation given by,

$$H_{int} = \frac{e}{2mc}(\boldsymbol{A}\cdot\boldsymbol{p} + \boldsymbol{p}\cdot\boldsymbol{A}) = \frac{e}{mc}\boldsymbol{A}\cdot\boldsymbol{p} \qquad (10)$$

where $\boldsymbol{p}$ is the electronic momentum operator. This Hamiltonian is derived by replacing the momentum operator with $\boldsymbol{p} - {}^{e}/_{c}\,\boldsymbol{A}$, for a system of electrons in an electromagnetic field. The negligible quadratic term of the vector potential $\boldsymbol{A}$ is dropped.

This photoemission process can then be discussed within the so-called *three-step model*, where the photoemission process is divided into three independent and sequential steps:

1.) Optical excitation of the electron in the bulk, where the electrons interacts with a photon of vector potential $\boldsymbol{A}$.

2.) Travel of the excited electrons to the surface. This step includes the probability of an electron reaching the surface without scattering. Electrons interacting inelastically with the system can be considered secondary electrons that add to the high energy background of the system.

3.) Escape of the photoelectron into the vacuum. This step is described by a transition probability through the surface that depends on the energy of the photoelectron and the work function of the material. ($\hbar^2 \boldsymbol{k}_\perp{}^2/2m > |E_0| + \phi$)

Sudden approximation

However, this *three-step model* assumes non-interacting electrons in the system. In the transition probability ω_{fi} in eq. (9), the wavefunctions were factored into terms for the photoelectron and the (N-1) terms for the electrons left in the system. This assumption becomes trivial, because once the photoelectron leaves the sample, the system will then relax. This problem is simplified by the *sudden approximation*, where the photoemission process is assumed to be *sudden*, with no interactions between the photoelectron and the system it left behind. In this approximation, the final state can be written as

$$\Psi_f^N = \mathcal{A}\phi_f^k \Psi_f^{N-1} \qquad (11)$$

where $\mathcal{A}$ is an asymmetric operator which antisymmetrizes the N-electron wave function so that it satisfies the Pauli principle. ϕ_f^k is the photoelectron's wave function and Ψ_f^{N-1} is the final state wave function of the (N-1) electrons left in the system. In the sudden approximation, the initial and final states of the system are equal and the transition probability can be expressed as

$$\omega_{fi} \propto \left|\langle \phi_f^k | H_{int} | \phi_i^k \rangle\right|^2 \qquad (12).$$

When electrons in the solid interact, the total photoemission intensity can be expressed as a summation over all interacting states in the system for all kinetic energy E_{kin} and momenta k,

$$I(\mathbf{k}, E_{kin}) = \sum_{f,i} \omega_{f,i} \propto \sum_{f,i} \left|\langle \phi_f^k | H_{int} | \phi_i^k \rangle\right|^2 \sum_m \left|\langle \Psi_m^{N-1} | \Psi_i^{N-1} \rangle\right|^2 \delta\left(E_{kin} + E_m^{N-1} - E_i^N - h\upsilon\right) \quad (13)$$

where $\left|\langle \phi_f^k | H_{int} | \phi_i^k \rangle\right|^2 \equiv M_{f,i}^k$ is the one-electron dipole matrix element, and $\langle \Psi_m^{N-1} | \Psi_i^{N-1} \rangle$ is the (N-1) overlap integral. In non-interacting systems, $\sum_m \left|\langle \Psi_m^{N-1} | \Psi_i^{N-1} \rangle\right|^2$ becomes 1 at a single value of m and is zero everywhere else, and if at the same time, $\sum_{f,i} \left|\langle \phi_f^k | H_{int} | \phi_i^k \rangle\right|^2$ is not zero, then the spectral function will consist only of a series of sharp delta functions at a given momentum and energy. If on the other hand, the system interacts, the middle term in eq. (13) will be non-zero in more m values, and the corresponding ARPES spectra will be a convolution between the delta functions and interacting states.

One-particle spectral function

For correlated electron systems, one alternative approach is the use of Green's formalism. In this formalism, the intensity measured in an ARPES experiment can be expressed as,

$$I(\boldsymbol{k}, \omega) = I_0(\boldsymbol{k}, \upsilon, \boldsymbol{A}) f(\omega) A(\boldsymbol{k}, \omega) \quad (14)$$

where $\boldsymbol{k}$ is the in-plane electron momentum, ω is the electron energy measured from the Fermi level and $I_0(\boldsymbol{k}, \upsilon, \boldsymbol{A})$ is proportional to the squared one-electron matrix element $\left|M_{f,i}^k\right|^2$, $A(\boldsymbol{k}, \omega)$ is the one-particle spectral function and $f(\omega) = \left(e^{\omega/k_B T}\right)^{-1}$ is the Fermi function.

The one-electron matrix element $\left|M_{f,i}^k\right|^2$ is responsible for the dependence of the photoemission data on the experimental conditions, i.e., photon energy and polarization

vector-sample geometry. By using the commutation relation $\hbar \boldsymbol{p}/m = -i[x, H]$, $\left|M_{f,i}^{k}\right|^2$ can be expressed as,

$$\left|M_{f,i}^{k}\right|^2 = \left|\langle \phi_f^k | \varepsilon \cdot \mathrm{x} | \phi_i^k \rangle\right|^2 \qquad (15)$$

where ε is a unit vector along the polarization vector of the vector potential $\boldsymbol{A}$. To have a non-zero photoemission intensity, the whole integral in the overlap integral must be an even function upon reflection with respect to the mirror plane.

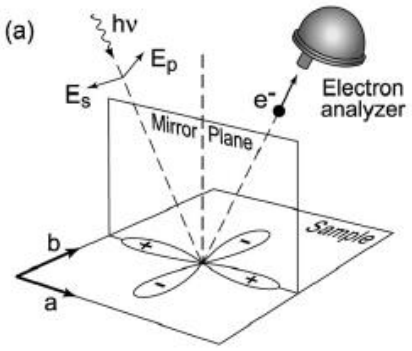

Figure 2.3. Mirror plane emission form a d_{x2-y2} orbital, with respect to the photon polarization and electron analyzer. Taken from ref. [36]

2.1.2. Angle resolved photoelectron spectroscopy: experiment

A typical ARPES system consists of a light source, an electron lens, a hemispherical electron analyzer and the UHV chamber, as shown in Fig. 2.4.

Light sources

Typical light sources include gas discharge lamps for laboratory-based ARPES systems, or synchrotron light sources. Gas discharge lamps can provide photons with discrete energy levels, depending on the emission spectrum of the gas used. This emission is then monochromatized before reaching the sample surface. One example of this gas discharge lamp is a discharge lamp that uses He plasmas generated by electron cyclotron resonance (ECR). He lamps can provide He Iα and He IIα discharges with

photon energies 21.2 eV and 40.81 eV respectively. He discharge lamps provide unpolarized radiation, which gives an added advantage in that the matrix element $\left|M_{f,i}^{k}\right|^{2}$ is never zero and will thus have access to all the energy bands.

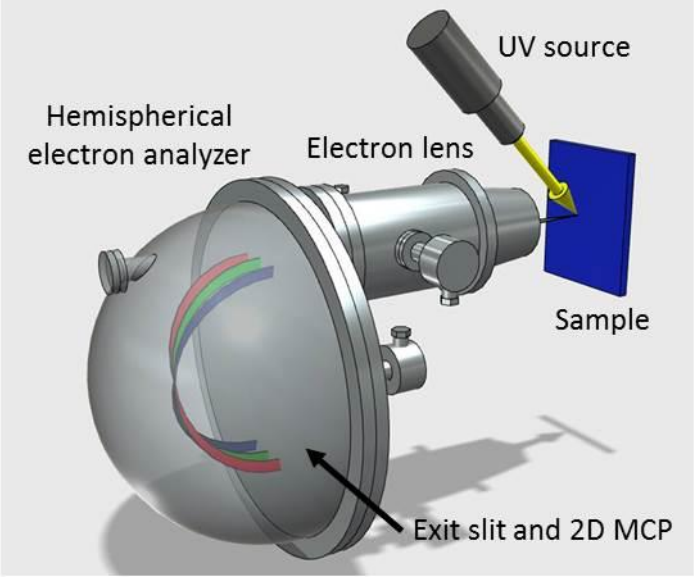

Figure 2.4. Schematic diagram of a typical ARPES system [38].

Synchrotron light sources on the other hand, can provide photons over a continuous energy range from UV to hard X-rays, allowing photon-dependent (and thus $k_{\perp}$-dependent) ARPES measurements. Synchrotron light sources can also provide linearly polarized radiation that can provide additional information about the symmetries of the electron atomic orbitals involved. Synchrotron sources also have spot sizes much smaller than gas discharge lamps. New laser based ARPES systems are also now available, having the similar advantages as the synchrotron based light sources.

One key aspect in the selection of light source to be used in ARPES experiments is the energy of the incident photon. As shown in Fig. 2.5, by varying the photon energy, the surface sensitivity of the measurement can be changed. This allows the scanning of the $E(\boldsymbol{k}_{\perp})$ dispersion via the use of different photon energies.

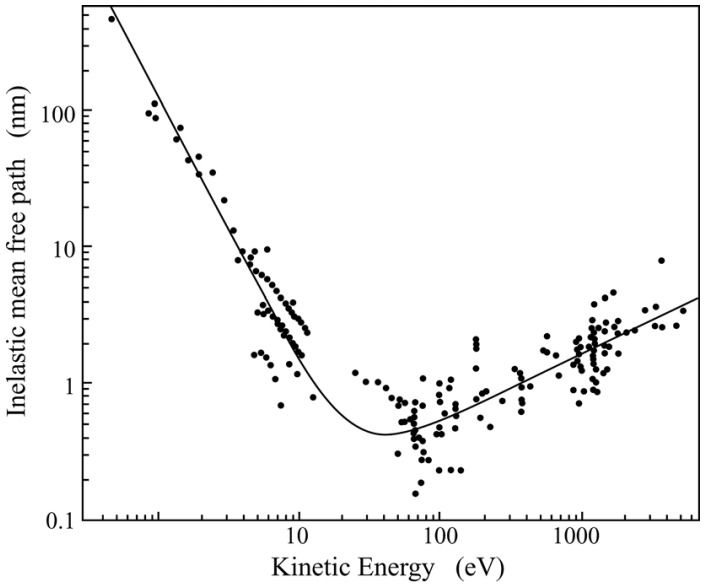

Figure 2.5. Kinetic energy dependence of the universal mean free path of excited electrons in a solid. Taken from [36]

The use of UV radiation (10-100 eV) gives ARPES measurements the surface sensitivity required to probe the electronic structure of surfaces.

Electron lens

After the photoemission process, the electrons are ejected from the surface of the sample in straight lines in all directions until they reach the entrance slit of the electron lens. These electrons will then be focused into the entrance slit of the hemispherical analyzer using electrostatic lenses.

Hemispherical analyzers

The hemispherical analyzer consists of two concentric hemispheres (of radius R1 and R2) that are kept at a potential difference ΔV so that only electrons with a narrow range of kinetic energies (centered at the pass energy, $E_{pass} = \frac{e\Delta V}{R_1/R_2 - R_2/R_1}$) will pass through the hemispherical analyzer and reach the exit slit. It will then be possible to measure the kinetic energy of the photoelectron with an energy resolution

$$\Delta E_a = E_{pass}\left(\frac{w}{R_0} + \frac{\alpha^2}{4}\right) \qquad (16)$$

where $R_0 = (R_1/R_2)/2$, w is the width of the entrance slit and α is the acceptance angle.

Upon reaching the exit slit, the electrons will be counted by a 2D multichannel plate (MCP) coupled to a phosphorous screen in front of a CCD camera. Electrons passing through the MCP is multiplied and becomes a "packet" of electrons with a given energy and momentum. These packets then hit the phosphorous screen creating a pixel of light. These flashes of light are then detected by the CCD camera, where the pixels correspond to energy and emission angle/momentum values.

2.2. Reflection High Energy Electron Diffraction (RHEED)

In this section, the fundamental principles behind reflection high energy electron diffraction will be discussed. The discussions in this section are based mostly on the books *Solid Surfaces, Interfaces and Thin films* by Lüth [8] and *Reflection high energy electron diffraction* by Ichimiya and Cohen [39], unless otherwise specified.

Elastic scattering experiments have been among the most important sources of information for surfaces and thin films. Like in the physics of bulk materials, these scattering experiments can reveal information about the symmetry and geometric arrangement of atoms on surfaces. X-rays, electrons, atoms, etc., can all be used in scattering experiments, depending on the surface sensitivity required in the experiment. X-rays can penetrate through the crystal samples, while low energy atoms and molecules only interact with the outermost atoms. Low energy electrons interacts only a few Angstroms into the surface.

For surface science, low energy electron diffraction (LEED) and reflection high energy electron diffraction (RHEED) are the two most widely used experiments in

structural determination of the surface [8]. In LEED, electrons with energies of 20-500 eV are used, and these low energies make them well suited for surface science since their mean-free path in the solid is short. In RHEED, electrons with energies of 10-100 keV are used. The grazing incidence and detection angles used in the experiment means that the long mean-free path is associated with a penetration depth of only a few atomic layers normal to the surface. The high energies used in RHEED makes visualization of the diffraction patterns easier, where a simple fluorescent screen can be used. Furthermore, the experimental geometry in RHEED experiments, as shown in Fig. 2.6 (a), allows *in-situ* observation of the surface, which makes it a valuable experiment in thin film growth.

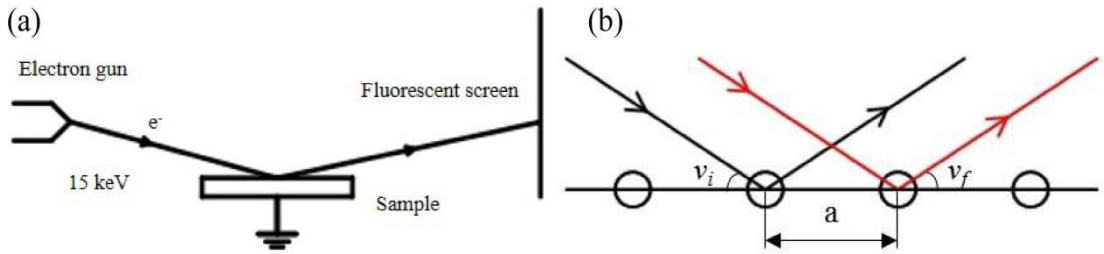

Figure 2.6 Schematic drawing of RHEED experiments and (b) a schematic drawing of scattering from a row of atoms.

For an incident plane wave with wavelength, λ, interference will occur due to the path difference of waves scattered from different atoms. Constructive interference occurs when the path difference is an integer value of the wavelength. For a simple one-dimensional row of scatterers (Fig. 2.6 (b)) with spacing a, the diffraction condition can be given as,

$$a\cos\upsilon_i - a\cos\upsilon_f = n\lambda \qquad (17),$$

or by using the expression, $\frac{2\pi}{\lambda} = K$ and defining $B_n = \frac{2\pi n}{a}$, we have,

$$k\cos\upsilon_i - k\cos\upsilon_f = B_n \qquad (18).$$

To satisfy the diffraction conditions, the parallel components of the initial and final wave vectors must differ by an integer value of $2\pi/a$.

For 2D surfaces, there will be other rows of atoms parallel to the one-dimensional row discussed previously. Interference perpendicular to the line will also occur, and the interference maxima will lie at points along a circle. The path difference between an atom at the set origin and an atom at $\mathbf{r_i}$ can be given by,

$$\mathbf{k_f} \cdot \mathbf{r_i} - \mathbf{k_i} \cdot \mathbf{r_i} \qquad (19).$$

Summing over all scatters, the diffracted amplitude [39] can be given as,

$$A(\mathbf{S}) \sim \sum_i e^{i\mathbf{S}\cdot\mathbf{r_i}} \qquad (20),$$

where $\mathbf{S} = \mathbf{k_f} - \mathbf{k_i}$.

The intensity can then be expressed as,

$$I = \mathbf{A}\mathbf{A}^* = \sum_{i,j} e^{i\mathbf{S}\cdot(\mathbf{r_j}-\mathbf{r_i})} \qquad (21).$$

Another approach in interpreting RHEED is through the Ewald construction. In this approach, energy and momentum conservation are combined to describe the diffraction. The energy and momentum conservation require that

$$|\mathbf{k_f}| = |\mathbf{k_i}| \qquad (22)$$

$$\mathbf{k_f} - \mathbf{k_i} = \mathbf{G_m} \qquad (23).$$

The energy conservation in eq. (22) requires that the magnitude of the final wave vector $\mathbf{k_f}$ is constant equal to the incident wave vector $\mathbf{k_i}$. This will result in final wave vectors that can be described by a sphere, the Ewald sphere. In the required momentum conservation in eq. (23), the difference in the final and initial wave vectors should be equal to the 3D reciprocal lattice vector G_m. The intersection of the Ewald sphere with reciprocal lattice points determine allowed diffraction conditions.

Graphically, one constructs a set of parallel rods normal to the surface, on points that correspond to the 2D reciprocal lattice points. The intersection of these rods with the Ewald sphere will correspond to allowed diffraction conditions, as shown in Fig. 2.4 (a).

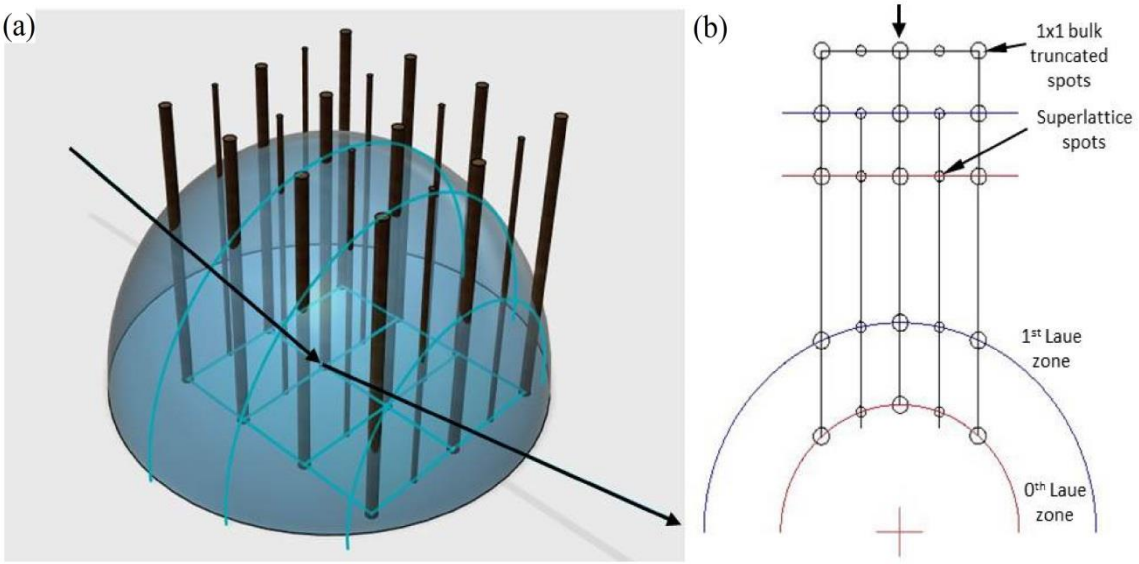

Figure 2.7 (a) Schematic drawing of the Ewald sphere with reciprocal lattice rods (not drawn to scale) and (b) a schematic drawing of the reciprocal lattice of a 2×1 super lattice and its RHEED pattern.

For a two-dimensional square lattice of scatterers with atoms at $\rho = na\hat{x} + ma\hat{y}$, eq. (4) can be expressed as,

$$A(\mathbf{S}) = \sum_{n,m}^{N-1,M-1} \exp\left(i\mathrm{S_x}\mathrm{na} + i\mathrm{S_y}\mathrm{ma}\right) \qquad (24).$$

The geometric series in eq (24) can be summed up, and from eq. (21), the intensity can be written as,

$$I(\mathbf{S}) = \frac{\sin^2(NS_X a/2)}{\sin^2(S_X a/2)} \frac{\sin^2(NS_y a/2)}{\sin^2(S_Y a/2)} \qquad (25).$$

2.3. Ultrahigh vacuum (UHV) chambers

2.3.1. Ultra-high vacuum

One of the most important requirements of surface and interface science is an ultra-high vacuum (UHV) chamber. The preparation of well-defined surfaces and interfaces with minimal contamination from residual gasses requires pressures lower than 10^{-10} Torr. The major parts of a typical UHV chamber are the stainless steel chamber, pumps and pressure gauges. The discussions in this section are based on the author's knowledge and experience with UHV chambers and is supplemented by the books *"Solid Surfaces, Interfaces and Thin Films"* by Lüth [8] and *"The Vacuum Technology Book vol II"* [40]. Detailed discussions about vacuum science and technology can be found in numerous books available on the subject.

A typical UHV chamber will consist of all stainless steel parts that can be connected together by soft copper gaskets cut with knife edges on both sides of the *conflat flange*. For chambers used in photoemission experiments, an additional requirement is that there should be no external magnetic field inside the chamber that could distort the path of the photoelectrons in the electron lens and hemispherical analyzer. The chamber walls are covered with *mu*-metal shielding to block out external magnetic fields, and all the metallic parts installed inside the chamber are carefully checked for any magnetization.

Vacuum pumps

In pumping the chamber, there are several kinds of vacuum pumps available with varying operational pressure range. To achieve UHV conditions, the most common pump used is the turbomolecular pump (TMP). The operational range of a TMP is from 10^{-2}–10^{-10} Torr. or lower. In a turbomolecular pump, turbine-like rotor blades rotate

inside the TMP housing with velocities of up to 40,000 rpm. Between these rotors, bladed stator disks having similar geometries are present. The pumping action occurs through the transfer of momentum from the rotating blades to the gas molecules. In modern TMPs, maintenance-free and wear-free magnetic bearings are used instead of ball-bearings that require oil. The rotors are magnetically levitated and thus mechanical contact between the rotor and the TMP housing is removed. By TMPs alone, UHV conditions can be achieved, however TMPs require a backing pump to lower the pressure in the outlet side of the TMP [40]. Furthermore, the rotor blades of the TMP are not designed to rotate at operating velocities at ambient pressures. A roughing pump is first required to reduce the pressure to around 10^{-2} Torr. before TMP operation. In most systems, a single pump can be used as the roughing and backing pump. The most common roughing/backing pump used is the rotary vane pump (RP). It consists of an eccentrically installed rotor and vanes that rotate radially inside the pump housing. During the rotation of the motor, gas flows in through the inlet valve. At this stage, the outlet valve is close. As the rotor rotates, it pushes the gas around the pump housing. At the exit phase, the inlet valve is sealed and the outlet valve opened. The gas is then expelled to the exhaust and the rotor completes one rotation, and then the cycle is repeated. Modern RPs use magnetic bearings or oiled ball bearings for the rotors and can be built in single- or two-stage versions.

Supplementary pumps such as ion getter pumps and Ti sublimation pumps (TSP) are often installed in UHV chambers. With no mechanical parts, these pumps are ideal for maintaining UHV conditions over long periods of time, and when the experiment to be done is sensitive to vibrations. In these pumps, gas molecules are adsorbed on a Ti cathode (IG pump) or on the Ti coated pump housing (TSP).

Pressure gauges

For accurate pressure measurements, several pressure gauges are available. The varying operational range of these gauges require at least two different types of gauge in a UHV chamber to cover atmospheric pressures to UHV. *Pirani* gauges, which measure the resistance variations in a filament with respect to pressure, are most commonly used for measuring atmospheric pressures to medium vacuum (10^{-4} Torr.) conditions. From there, ionization gauges are used. A fine wire is used as an ion collector as a cathode filament and anode grid is used to ionize residual gasses. The pressure inside the chamber can then be measured in terms of the ionization rate and the ion current measured.

A simple schematic diagram of a typical UHV chamber is shown in Fig. 2.8.

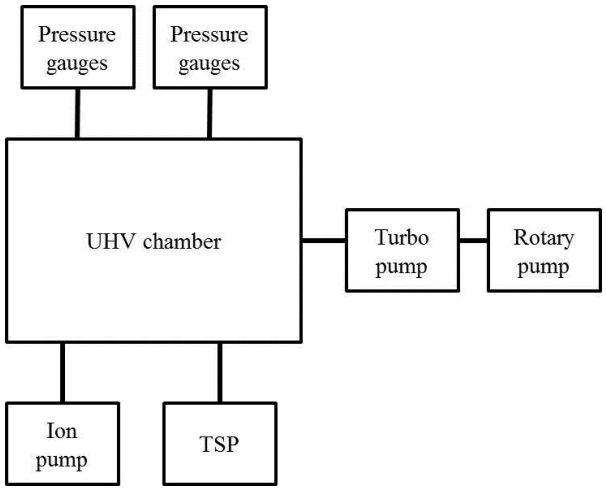

Figure 2.8. Simple schematic of a typical UHV chamber.

Bake out

Finally, to achieve good UHV conditions, a bake-out process is usually employed. Pumping with TMPs can easily achieve 10^{-9} Torr, but can take time to reach 10^{-10} Torr. Gas molecules, especially water, can be adsorbed on the chamber surface and

can be difficult to remove by pumping alone. In the bake-out process, the chamber is heated to temperatures above 100°C to facilitate desorption of these gasses from the chamber walls, and from there, they can be easily removed through the TMP. Higher bake-out temperatures will result in faster reduction in the pressure. The UHV chamber itself can be baked at much higher temperatures, but because of other parts inside the UHV chamber such as glass viewing ports, flanges connected with rubber O-rings, magnetically coupled transfer rods, etc, typical bake-out temperatures used are between 120-180°C. During the bake-out process, non-bakable cables and parts are first disconnected and removed. The chamber is then wrapped in aluminum foil to help in heat conduction. Electrical heaters and thermocouples are attached to the chamber. The chamber is then completely covered in insulating blankets to trap hot air around the chamber to further facilitate the baking. The residual gasses inside the chamber can then be monitored by a quadrupole mass spectrometer (QMS) attached to the chamber. The bake-out process can then be stopped when the water, H_2 and N_2 levels are sufficiently low. The bake-out process can last from 24 hours to 2 weeks, depending on the size of the chamber and the bake out temperature used. For the ARPES chamber used in this study, the typical baking time is around 2 weeks This includes the pre- and post-bake preparations.

2.3.2. UHV chambers in this study

All the experiments in this study were done in the ultra-high vacuum (UHV) complex [41] in the Surface and Materials Science Laboratory of the Nara Institute of Science and Technology (NAIST). The UHV chambers in this system mostly use RPs, TMPs and TSPs and are equipped with their own *Pirani* and ionization gauges. A more detailed description of this UHV complex can be found in ref. [41]. The UHV chambers

are all connected to a central trunk that houses the transfer carts, but are separated from each other with gate valves. Each UHV chamber can be operated and vented independently, but the introduction of a sample to the UHV chamber can only be done in airlock chambers scattered throughout the UHV complex. Almost all UHV chambers in this complex are equipped with evaporation sources and RHEED. Different experiments can be carried out on a sample without exposing it to ambient pressures by the UHV transfer system. Fig. 2.9 shows a schematic of the UHV complex.

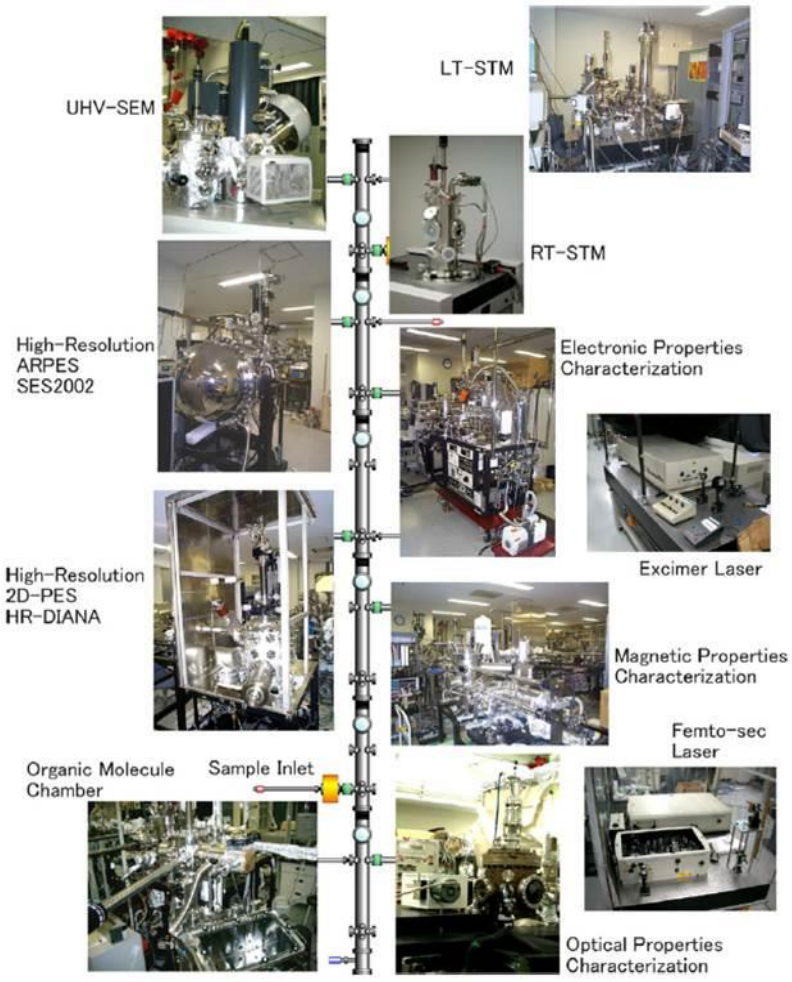

Figure 2.9. UHV complex for total analysis of surface structure and properties [41].

Samples are prepared in a fume hood and attached to a specially designed sample holder. Fig. 2.10 (b) shows the sample holder used in this study, with a melted

Si sample still mounted. The Si wafers are attached to the sample holder by placing it between a Ta mounting brace and a small Ta sheet underneath. The mounting brace is then screwed onto the Cu mount of the sample holder.

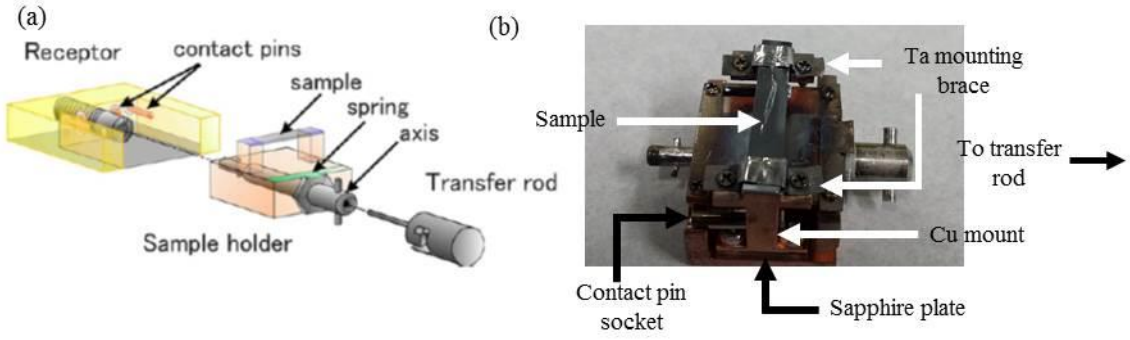

Figure 2.10. (a) Schematic drawing of the sample holder and transfer system [41] and (b) a (melted) silicon wafer sample mounted on a sample holder.

The sample holder is then introduced to the UHV complex through an airlock chamber. The pressure in the different chambers in the UHV complex is held at ~10^{-10} Torr to minimize contaminations on the surface of the sample. The Scienta chamber (ARPES) and Taiyo-1 chamber (electrical properties characterization) are the main chambers used in these experiments. Both chambers are equipped with various metal deposition sources and reflection high energy electron diffraction (RHEED) systems.

The ARPES system used in this study is equipped with an ECR based He discharge lamp and a Scienta high resolution electron analyzer (SES-2002). The UV source is incident on the sample surface at an angle of 45°. The chamber is equipped with a 5-axis manipulator, to allow control of the sample position in terms of the x-, y-, z- axis, as well as in-plane and out-of-plane rotations.

Chapter 3. Surface resonance states of the Si(110)16×2 surface

There already has been some reports about the electronic structure of the clean Si(110)16×2 surface. 16×2 derived surface states have been observed and identified, but many unknown bands still remain and the complete band structure has not been investigated. These papers studied the electronic structures in the bulk band gap, hence they were able to identify them as surface states easily. For electronic states intermixed with the Si bulk bands, the identification of them as bulk- or surface- derived states is much more difficult. A systematic study of these states is necessary to have a complete set of experimental data that theoretical studies can compare their results with. In particular, a good agreement of DFT calculations of the band structure of the Si(110)16×2 based on proposed structural models with actual experimental band dispersions will prove useful in validating these structural models.

In section 3.1, a short summary of the published literature on the clean Si(110) surface is presented. Section 3.2 describes a short discussion about the experiments done in this chapter.

The results and discussions are in Section 3.3. Section 3.3.1 details the surface and electronic structures of the Si(110)16×2 surface obtained in this study. ARPES spectra taken from well-ordered 16×2 surfaces are presented and discussed. Several electronic states are observed in the ARPES spectra and these are discussed in this section.

Section 3.3.2 details the effects of structural changes on the electronic states observed on the clean Si(110)16×2 surface. In particular, states located within the bulk band gap are analyzed, and their possible origins on the Si(110) surface are proposed.

3.1. Introduction

Compared to the (001) and (111) planes, the (110) plane of silicon has not been as extensively studied. In fact, up until now, there is still no widely accepted structural model for the clean Si(110) surface. There have been several structural models proposed, but these models have not been able to sufficiently explain the available experimental results.

The ideal Si(110) surface, shown in Fig. 3.1, consists of Si atoms arranged in parallel zigzag chains running along the $[\bar{1}10]$ direction, with each chain separated by $0.542\ nm$.

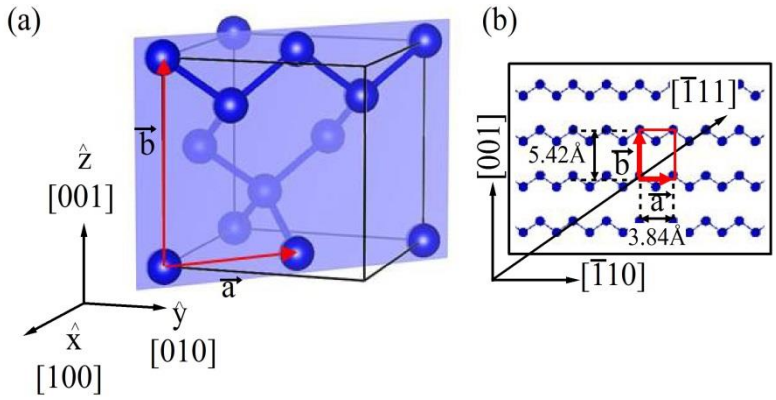

Figure 3.1 (a) The (110) plane of the Si crystal and (b) the unit cell of the ideal Si(110)1×1 surface.

The unit cell can be described by,

$$\mathbf{a} = \frac{a}{\sqrt{2}}(\hat{\mathrm{x}} + \hat{\mathrm{y}}) \qquad (26)$$

$$\mathbf{b} = a\hat{\mathrm{z}} \qquad (27)$$

where $a = 0.543\ nm$ and $\frac{a}{\sqrt{2}} = 0.384\ nm$.

Each Si atom on the (110) surface has one unsaturated dangling bond, and several reconstructions have been observed on the surface. In 1965, Jona [42] reported observing 4×5, 2×1, 5×1, 7×1, 9×1 [43], “initial” and “unknown” [44]reconstructions.

These reconstructions were also observed by other groups [43, 44]. Electron diffraction experiments by Olshanetsky [44] and Yamamoto [21] on clean Si(110) surfaces showed rows of superlattice spots parallel to the $\langle \bar{1}11 \rangle$. Olshanetsky referred to this reconstruction as the Si(17 15 1) 2×1 [44], while Yamamoto called this the Si(110)"16×2". Yamamoto reported that in RHEED patterns from atomically clean Si(110) surface, only the 16×2 structure remains, while the rest of the reconstructions previously observed were due to small amounts of Ni contamination (1-7%) on the surface [21, 22, 45]

The first clear RHEED pattern of the Si(110)16×2 was presented by Yamamoto [21]. For the diffraction pattern taken at the [001] incidence, the (00) and (11) fundamental spots are divided into 16 equal parts by superlattice spots, as shown in Fig. 3.2 (a).

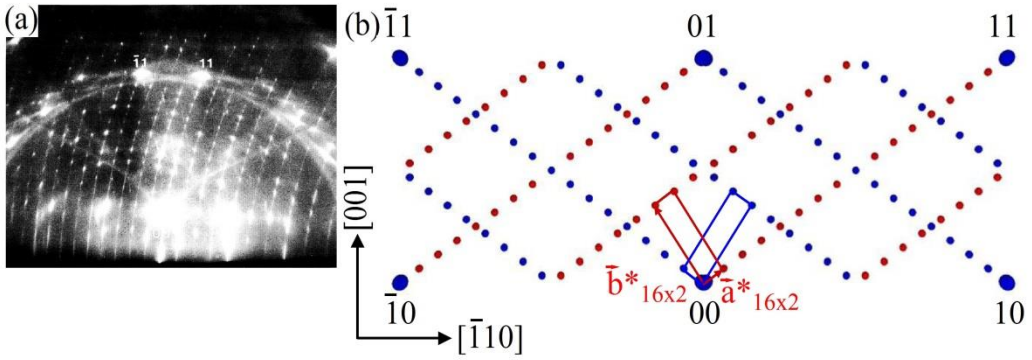

Figure 3.2 (a) RHEED pattern of the Si(110)16×2 taken at the [001] incidence taken from [21] and (b) the reciprocal lattice of a double domain Si(110)16×2 surface.

The reciprocal lattice vectors of the Si(110)16×2 surface can be given by,

$$\mathbf{a}^*_{16\times2} = \frac{1}{16}\mathbf{a}^* + \frac{1}{16}\mathbf{b}^* \qquad (28)$$

$$\mathbf{b}^*_{16\times2} = \frac{-5}{32}\mathbf{a}^* + \frac{11}{32}\mathbf{b}^* \qquad (29),$$

and the real space unit cell can be given by,

$$\mathbf{a}_{16\times2} = 11\mathbf{a} + 5\mathbf{b} \qquad (30),$$

$$\mathbf{b}_{16\times2} = -2\mathbf{a} + 2\mathbf{b} \qquad (31).$$

The real space unit cells of the reconstructed 16×2 and the clean 1×1 surfaces are shown in Fig. 3.3.

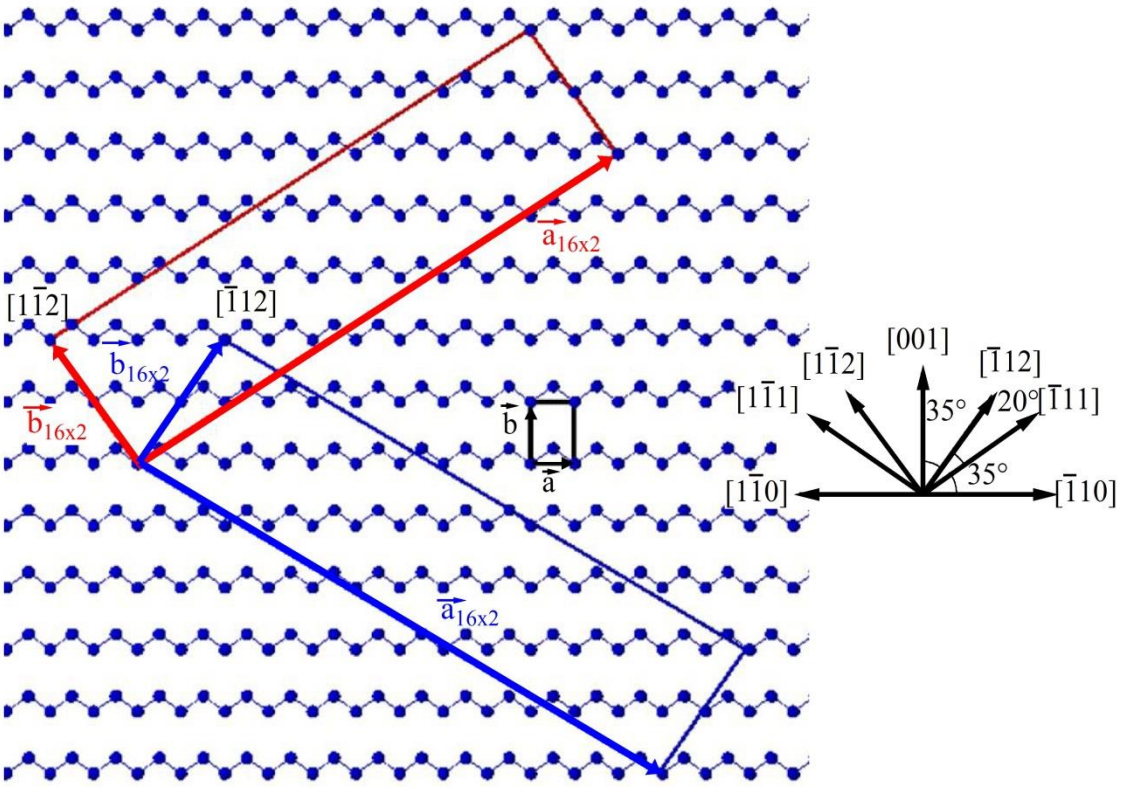

Figure 3.3. Unit cell of the ideal Si(110)1×1 and reconstructed Si(110)16×2 surfaces. Inset: High symmetry directions on the surface.

Soon after the determination of the surface reconstruction of the clean Si(110) surface through electron diffraction experiments [21], research efforts were redirected to understanding the real space structure of this surface. In 2007, Yamada *et al.* [31, 46], reported a detailed preparation method to produce high quality single domain Si(110)16×2 surfaces. They reported that by adding a post annealing step after flash annealing, electromigration due to the DC heating process used will align the

orientation of the steps with the direction of the current used in annealing [31]. They recommended annealing at 650°C for 30 min after several cycles of flash annealing at 1250°C in UHV, with the current direction along the $[\bar{1}12]$ or $[1\bar{1}2]$. This report was followed by several papers investigating the surface and electronic structure of a high quality single domain Si(110)16×2 surface.

In real space, scanning tunneling microscopy (STM) studies of the Si(110)16×2 surface have shown a series of chains running along either the $[\bar{1}12]$ or $[1\bar{1}2]$ direction, terraces one atomic step high and bright pentagon-shaped protrusions on both the upper and lower terraces (Fig. 3.4) [47, 48, 49, 31, 50]. The size of the 16×2 unit cell is 50.2 ×13.2Å and the terrace height is 1.92Å [47]. High resolution STM images showed large clusters of protrusions on both the upper and lower terraces (Fig. 3.4 (c)) [49, 50].

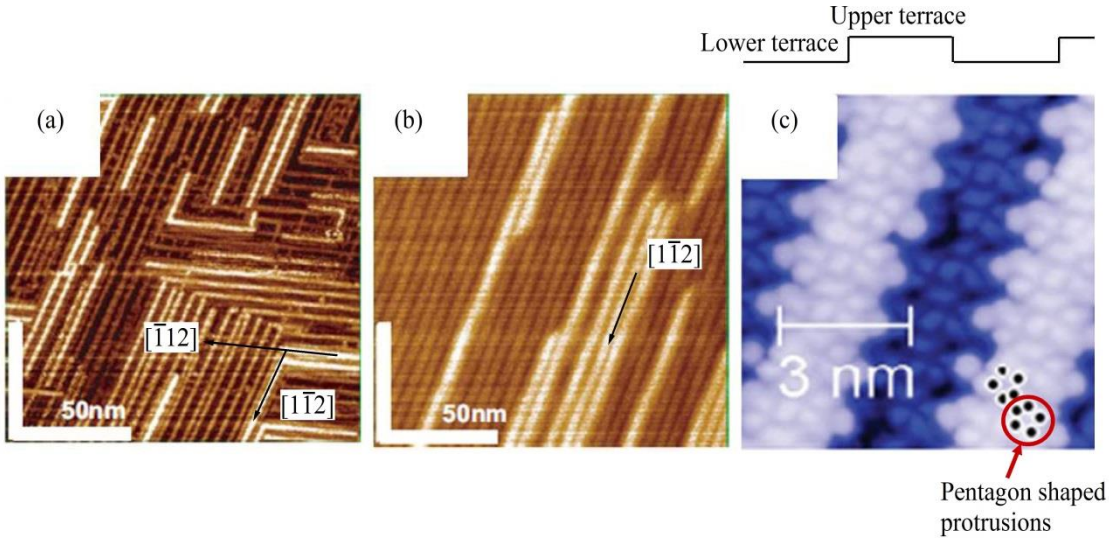

Figure 3.4 STM images of a (a) double and (b) single domain Si(110)16×2 surfaces [31], and a (c) zoomed in image of the pentagon shaped protrusions [50].

From the high resolution STM images, several models were proposed for the 16×2 reconstruction with different interpretations of the shape of the protrusions. An, *et al.*, [49] proposed several possible models for the bright protrusions based on their STM

images: the “adatom-tetramer” model, the “pentamer” model, the “adatom-pentamer” model, and the “tetramer-interstitial” (TI) model. They suggested that the tetramer-interstitial model was the most appropriate and proposed a complete model for the 16×2 using the “tetramer-interstitial” as reconstruction elements for the entire unit cell [49].

Detailed investigation of these reconstruction elements using first principles calculations showed that by using optimized adatom based structural models using 3×1 or 3×2 unit cells (Fig. 3.5 (a) and (b)), the dangling bonds of the ideal Si(110) surface are completely saturated and the only remaining DBs are on the adatoms themselves [51]. Total energy minimizations showed that the 3×1 adatom model was the most favorable. However, the arrangement of the adatoms does not match the available STM images [49, 50]. Furthermore, the 3×1 adatom model is accompanied by a metallic band structure, which does not agree with the semiconducting band structure observed by ARPES on Si(110)16×2 surfaces [52, 53, 54].

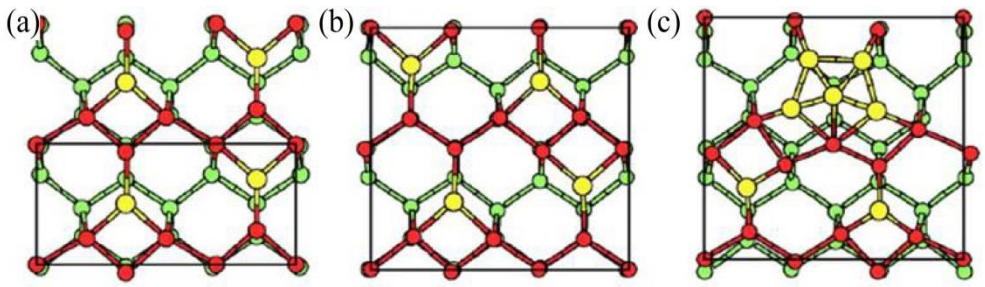

Figure 3.5 Relaxed atomic positions for the (a) 3×1 adatom, (b) 3×2 adatom and (c) 3×2 adatom-tetramer-interstitial (ATI) model for the Si(110)16×2 [51].

A 3×2 unit cell with the tetramer-interstitial (TI) elements suggested by An, *et al.* [49] was found to be less energetically favorable, but the addition of two adatoms (Fig. 3.5 (c)) makes it as favorable as the 3×1 adatom model [51]. A gap was also observed to open between the surface state bands [51], agreeing with the semiconducting band structures observed experimentally [52, 53, 54]. In addition to the

structural elements based on the adatom-tetramer-interstitial (ATI) model, the long range order of the 16×2 surface depends on the steps running along either the $[\bar{1}12]$ or $[1\bar{1}2]$ [55]. The formation of trenches and the rebonding of Si atoms across step edges further reduce the number of DBs on the surface [55]. A complete ATI model [51, 55] for the Si(110) 16×2 surface is shown in Fig. 3.6.

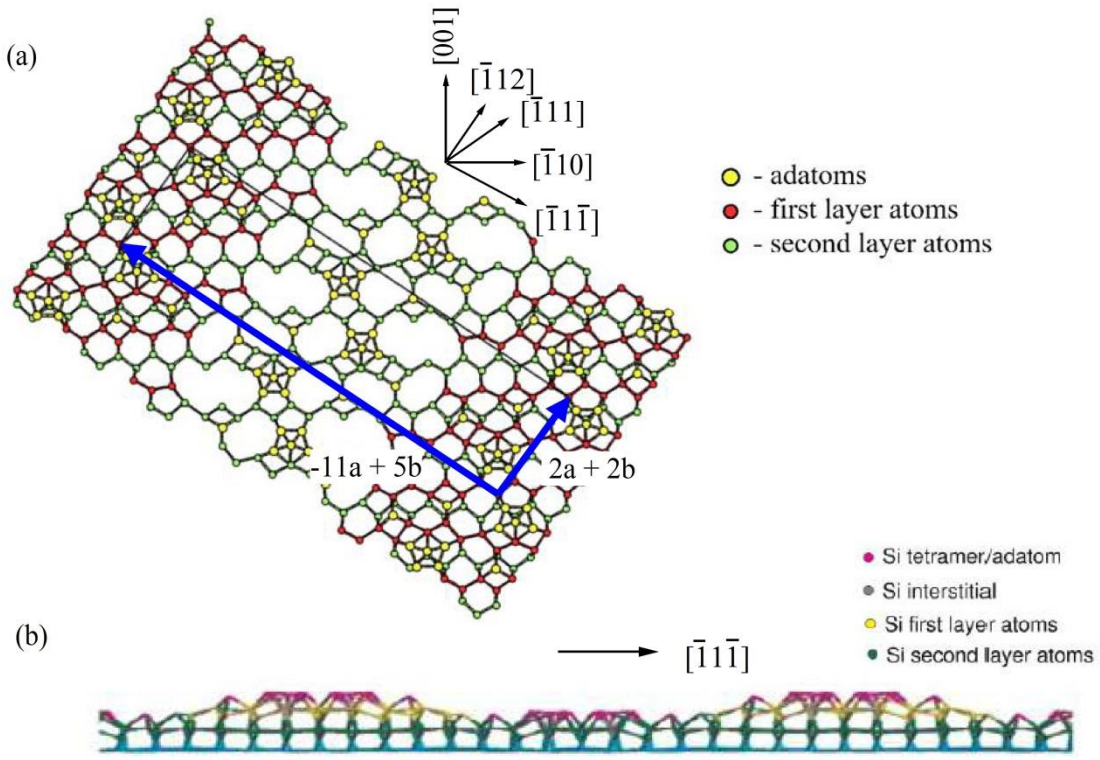

Figure 3.6 The adatom-tetramer-interstitial (ATI) model for the Si(110)16×2 [51] (a) top view and (b) side view [56].

Even though the ATI model was the most energetically favorable structure, it was found that it cannot completely explain the available experimental results. Data from a high resolution photoemission study by Kim, *et al.* [53] was analyzed using the ATI model and the surface states observed by ARPES (Fig. 3.8 (b)) and the Si 2p surface core level shifts (SCLS) (Table 3-1) were assigned spatial origins based on the ATI model.

However, a more recent combined ARPES (Fig. 3.8 (a), (c-d)) and STM study (Fig. 3.7) by Sakamoto *et al* [54]., showed additional surfaces states not observed in the study by Kim *et al.* [53]. They concluded that the ATI model could not fully explain the additional surface states observed and the LDOS mapping of these states. Furthermore, the protrusions in their STM images did not match the positions of the ATI reconstruction elements in the model. They suggested a structural model based on the ATI model with additional buckling in the underlying Si zigzag chains. This adatom buckling (AB) model is shown in Fig. 3.7 [54].

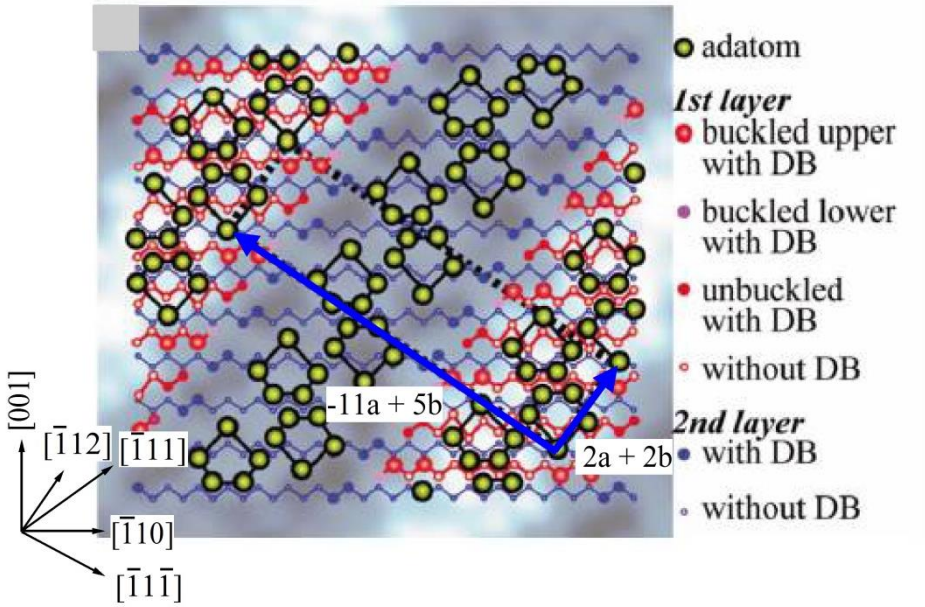

Figure 3.7. Adatom buckling (AB) model [54].

Using this new model, they proposed a reinterpretation of the SCLSs (Table 3-1) and provided new spatial assignments of the surface states observed in the spectra (Table 3-3).

Table 3-1. Summary of Si 2p surface core level shifts (SCLS) relative to Si 2p bulk component.

	Kim, et al. [53]		**Sakamoto, et al.** [54]	
	Relative binding energy (eV)	**Assignment**	**Relative binding energy (eV)**	**Assignment**
SC1	-0.83	Adatoms	-0.80	Buckled upper Si atoms
SC2	-0.33	Unsaturated π-bonded chains at step edges	-0.29	Unbuckled and 2^{nd} layer Si atoms
SC3	0.26	2^{nd} layer Si atoms	0.25	1^{st} and 2^{nd} layer Si atoms without DBs
SC4	0.50	Underlying π-bonded chains	0.47	Adatoms
SC5	0.70	Tetramer	0.71	Buckled lower Si atoms

Density functional theory (DFT) calculations of the band structure of the Si(110)16×2 surface based on the ATI model revealed differences between the calculated and experimentally observed surface states [56]. Four non-dispersing surface states within 0.5 eV of the Fermi level (E_F) were observed in the calculations [56] while only two were resolved in the same energy region in the ARPES spectra [54]. Several surface resonance states were also observed in the DFT calculations, but the thin slab used made it difficult for the authors to definitely distinguish between surface derived resonance states and bulk states [56]. Furthermore, in the experimental dispersions, the nature of the states in the projected bulk bands (bulk or surface resonance state) was not clarified. Simulated LDOS mapping also revealed differences [56] with the experimental LDOS mapping [54].

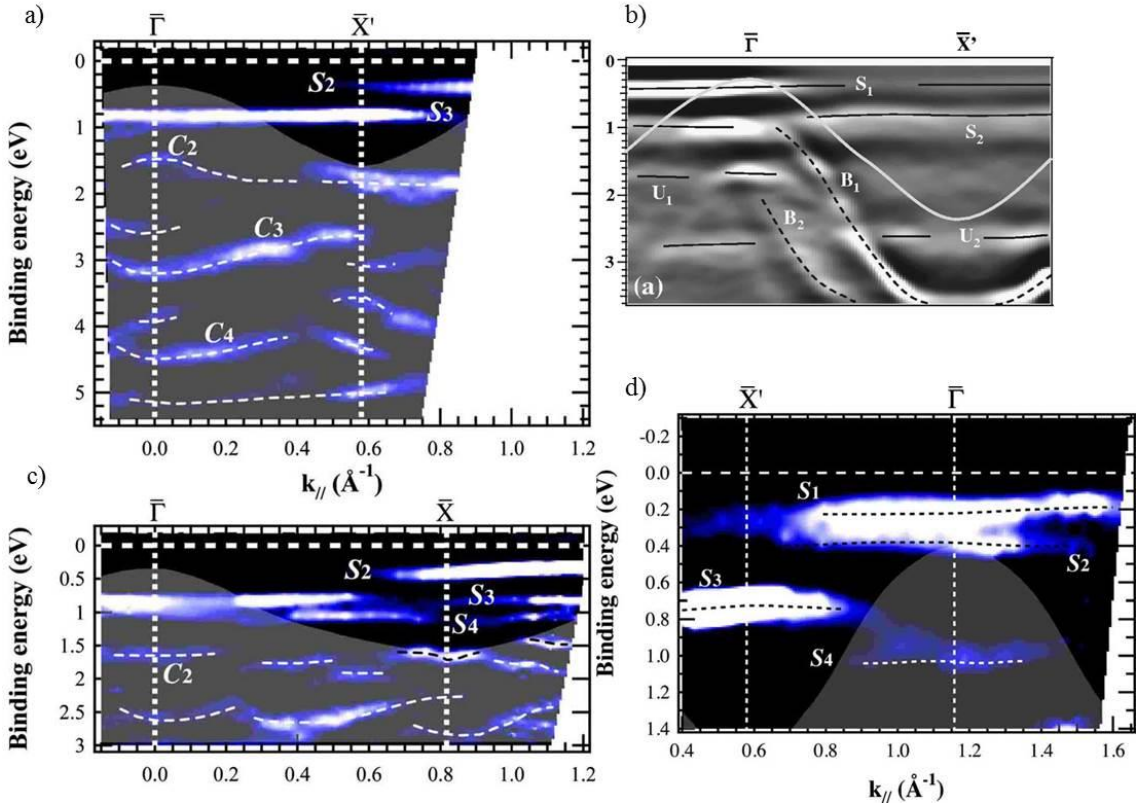

Figure 3.8 ARPES spectra of a single domain Si(110) 16×2 surface, (a) and (b) taken along the [001], and (c) [$\bar{1}$10] directions and (d) at the SBZ boundary along the [001] direction. (a), (c) and (d) are taken from ref. [54] and (b) is from ref. [53].

While the ATI model cannot completely explain all the experimental data, the AB model has not been fully investigated using first principles energy minimization. Further numerical and experimental investigations are still needed to be able to construct the correct structural model for the Si(110)16×2.

In this chapter, we look at the electronic states within the projected bulk bands and assign origins of these states. We first look at the band structure of the clean Si(110)16×2 surface and observe how these states change when the surface structure is modified by metal adsorption.

3.2. Experimental procedures

The samples used in these experiments were cut from n-type, P-doped Si(110) wafers. Two kinds of wafers were used throughout the experiments, low resistance (LR) and high resistance (HR) wafers. Both wafers were grown through the Czochralski process (CZ). The wafers used in this thesis are both n-type because of the desired goal of observing hole subbands in p-type inversion layers on the Si(110) surface.

Some relevant information are summarized in Table 3-2.

Table 3-2 Summary of the different Si wafers used in this study.

Wafer	Crystal axis	Dopant	Resistivity	Thickness	Surface	O.F.
n-Si(110) R9815(LR)	<110>±2°	P	0.0063-0.0075 Ω·cm	525±25 μm	Mirror polished	<111>±2°
n-Si(110) (HR)	<110>±1°	P	2-6 Ω·cm	525±25 μm	Mirror polished	$[\bar{1}10]$

The experiments done in this thesis were mostly done using the LR wafer. As discussed in section 2.2 and 2.3.1, the experiments used in this study are extremely sensitive to distortions in the path of the electrons excited from the surface. This means that excess excited electrons on the surface should be quickly removed through a connection to the ground. A sample with high resistance leads to excess charges on the surface which could distort the path of the excited electrons through an electric field, and result in distortions in the observed RHEED patterns and the ARPES spectra. The high dopant concentration of the wafers is also a significant factor in hole subband formation, which will be discussed later in section 5.3.4. The HR wafers were used to confirm reports about dopant concentration dependence of the ease of preparing clean surfaces, as will be discussed later in section 3.3.1.

The Si wafers were cut using a diamond tip pen into 25×4 mm^2 samples. They were then mounted on the sample holder (Fig. 2.10(b)) and introduced into the UHV

chamber through an airlock chamber [41]. Great care was taken so that the Si samples did not touch any metal tools or parts to avoid any possible Ni contamination. It was reported that even the smallest amount of Ni contamination could produce various surface reconstructions that would make getting a clean Si(110)16×2 surface impossible [21, 22].

Once the pressure in the chamber is in the UHV region (~5×10^{-10} Torr.), the sample was degassed by annealing it at low temperatures (<500°C) for 1-2 days. The Si samples are annealed by direct heating, where a current is passed through the sample. The annealing current is along the $[\bar{1}12]$ direction in the LR samples and along the $[001]$ in the HR samples. After completely degassing the sample, it is then flash annealed at 1250°C several times to get the clean Si(110) surface. On the last flash annealing step, the temperature is first reduced to ~600°C. The sample is then annealed at this temperature for 10 min. before the temperature is reduced back to the ambient room temperature. The sample temperature was measured using an optical pyrometer (Konica Minolta Spot Thermometer TR-630) and an IR thermographic camera (Thermovision FLIR A320). The pyrometer was used for temperatures above 700°C, while the IR thermographic camera can measure from 0-1300°C. The emissivity value used for Si was 0.67,

The quality of the surface reconstruction was monitored using RHEED. The accelerating voltage used in the experiments was 15 kV. The sample's orientation was determined from the RHEED patterns and was oriented accordingly.

ARPES measurements were done in ambient room temperature.

3.3. Results and discussion

3.3.1. Surface and electronic structures of the Si(110)16×2 surface

The quality of the clean Si(110) surfaces, as prepared by the method discussed in section 3.2, is confirmed by the quality of the diffraction patterns taken from the sample. Fig. 3.9 shows some representative RHEED patterns taken from an atomically clean, good quality Si(110)16×2 surface. RHEED patterns taken at the $[001]$ (Fig. 3.9(a)) and $[\bar{1}10]$ (Fig. 3.9(b)) incidence direction show two sets of streaks, indicating the presence of two domains on the surface. Along the streak from the 00 and $\bar{1}1$ fundamental spots in Fig. 3.9(a), several sharp fractional order spots are observed. These are the "16-structure" fractional order spots first observed by Yamamoto *et al* [21] (Fig. 3.2(a)). The intensity of one set of streaks is noticeably stronger than the other, a result of the post-annealing process introduced after flash annealing. It has been reported that prolonged post-annealing results in the formation of a single domain Si(110)16×2 surface [31].

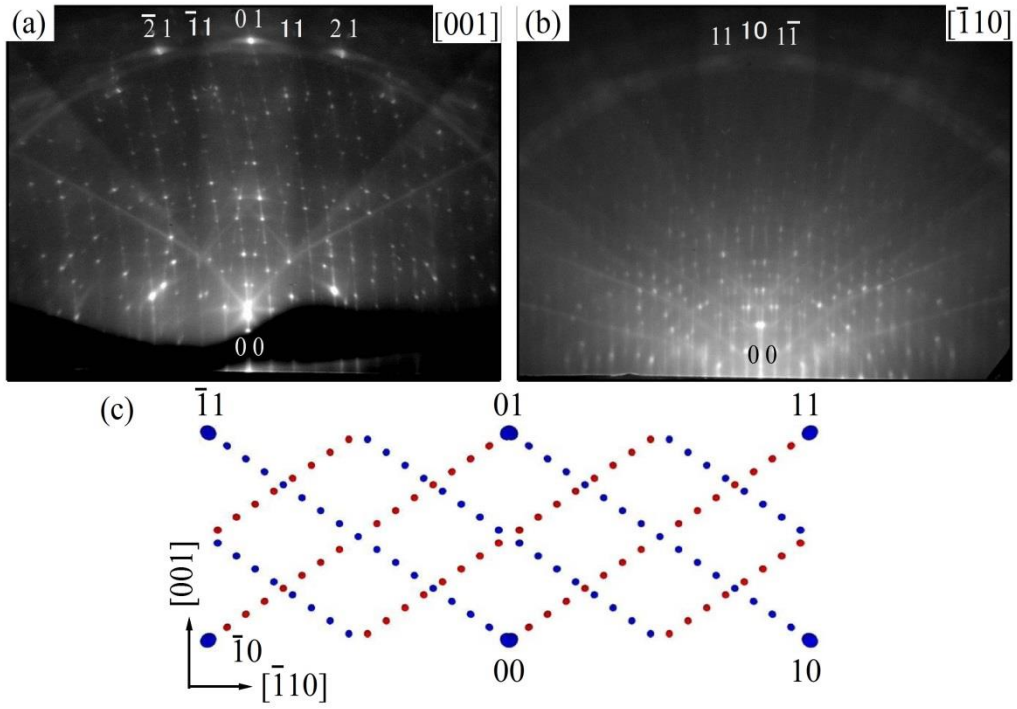

Figure 3.9 RHEED pattern of the double domain Si(110)16×2 surface taken at the (a) [001] incidence and (b) [$\bar{1}$10] incidence directions, and (c) its corresponding reciprocal lattice. In the reciprocal lattice, the larger blue circles are the fundamental Si 1×1 spots. The smaller circles indicate the fractional order 16×2 spots from the two domains (red and blue).

Without the post-annealing process (~600°C for 10 min), the 16×2 streaks can still be observed in the RHEED patterns, but the fractional order spots are no longer sharp and a strong diffuse background appears. Fig. 3.10 compares the RHEED patterns along the [001] direction for a sample prepared by flash annealing and post-annealing (Fig. 3.10 (a)) and a sample prepared by flash annealing only (Fig. 3.10 (b)).

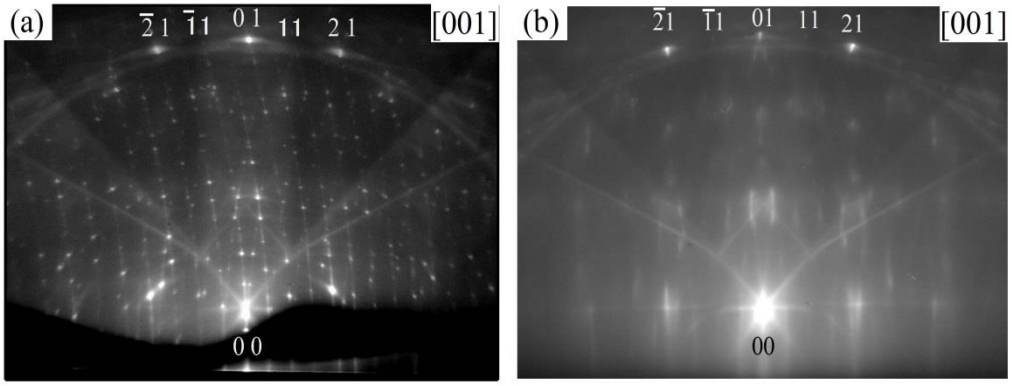

Figure 3.10 RHEED patterns of the Si(110)16×2 surface taken at the [001] incidence for a sample prepared by (a) flash annealing and post-annealing, and (b) flash annealing only.

In the STM and LEED investigation of Yokoyama, *et al.* [57] about the electromigration that causes the 16×2 reconstruction, they reported that for low resistance samples (0.01-0.02 Ω·cm), it takes longer post annealing times at 600°C to produce the same well-ordered single domain 16×2 reported in ref. [31]. For their high resistance samples (0.5-1.5 Ω·cm), post-annealing at 20 min produces the well-ordered single domain structures while it takes 14 hrs for their low resistance samples. A similar trend was observed in this study, where samples taken from the HR wafers produced sharper 16×2 diffraction spots after post-annealing for 10 min. However, it should be noted that the sharp double domain 16×2 spots were observed on both samples.

After confirming the quality of the prepared Si(110)16×2 surface, the electronic structure was investigated by ARPES.

Figure 3.11(a) shows the angle-resolved photoelectron spectra of the Si(110)16×2 surface, where the thick black lines indicate the surface Brillouin zone boundary of the ideal Si(110) surface. Fig. 3.11 (b) shows the 2nd derivative intensity map of the ARPES spectra taken from the Si(110)16×2 surface taken along the [001]

direction. The edge of the bulk band projections taken from tight-binding calculations of ref. [58] are included as the black dashed line in Fig. 3.11 (b).

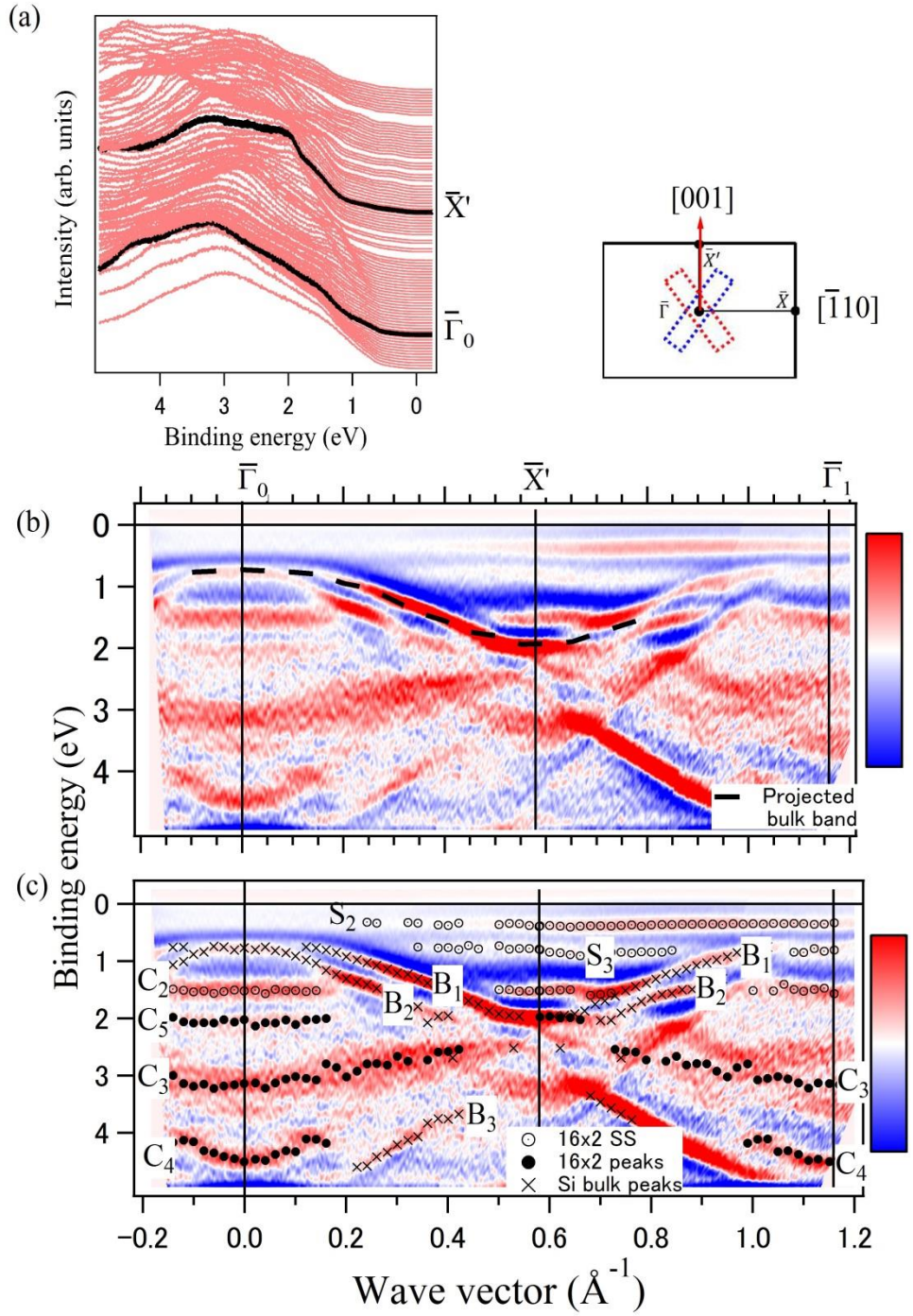

Figure 3.11. (a) Raw ARPES spectra of the of the Si(110)16×2 surface along the [001] direction and 2nd derivative intensity map of the ARPES spectra with (b) the projected bulk band edge taken from [54] and (c) peak positions obtained from energy distribution curves (EDC). Inset: SBZ of the 1×1 and 16×2 cells.

Peak positions taken from peak fitting of the energy distribution curves (EDC) of the raw ARPES data are overlaid as black dots in Fig. 3.11 (c), and are labelled following the convention used in ref. [54].

Bands labeled B_1-B_3 are electronic states derived from the bulk Si substrates. B_1 and B_2 are the heavy- and light- hole bands of Si, and are centered at $k_{\|} = 0$ Å^{-1} and similar parabolic bands can be seen at $k_{\|} = 1.15$ Å^{-1}. This $k_{\|}$ value corresponds to a reciprocal lattice vector of the Si(110) 1×1 SBZ as indicated in the inset of Fig. 3.11, which indicates the bulk Si origins of bands B_1 and B_2. The state B_3 also reflects the periodicity of the Si(110)1×1 SBZ, and can thus be assigned as a bulk Si state.

Above the projected bulk band edge, two non-dispersing electronic states are observed close to E_F: S_2 at ~0.4 eV, and S_3 at ~0.8 eV. At the $\bar{\mathbf{X}}'$ point, a third state can be seen above the projected bulk bands, C_2 at ~1.5 eV. Within ±0.2Å of the $\bar{\mathbf{\Gamma}}$ point, C_2 is located within the projected bulk bands.

S_2, S_3 and C_2 are clearly surface derived states. These have already been observed and identified as surfaces states in previous photoelectron spectroscopy studies [52, 53, 54]. In the most recent ARPES study by Sakamoto, *et al*. [54], two more surface states clearly situated in the bulk band gap were observed: S_1 at 0.2 eV and S_4 at 1.0 eV. In Fig. 3.11, the band widths of S_2 (~0.30 eV) and S_3 (~0.35 eV) and their locations so close to S_1 and S_4, makes it impossible to individually resolve these four states in the room temperature ARPES experiments in this study. These five non-dispersing states have been unanimously identified as surface states, however the exact origins of these states have not been clarified due to a lack of an accurate structural model for the Si(110)16×2 surface [53, 54, 56]. Kim, *et al.* [53] discussed their photoelectron results using the ATI model [51, 55], while Sakamoto, *et al* [54], proposed the new AB model

to discuss their results (S_1-S_4, C_2), which they found could not be explained using the ATI model.

Within the projected bulk bands, several more states are observed. At the $\bar{\Gamma}$ point, the following states are observed: C_5 at 2.0 eV, C_3 at 3.1 eV and C_4 at 4.5 eV as shown in Fig. 3.11 (c). The dispersion of C_5 is similar to C_2, non-dispersing with a band width of ~0.3 eV. C_3 is parabolic, opening upward with a bandwidth of 1.0 eV. C_4 is also parabolic and opening upward, but it is much narrower compared to C_3. Both C_3 and C_4 are observed at the $\bar{\Gamma}_0$ and $\bar{\Gamma}_1$ points and appear folded with respect to the SBZ at the $\bar{X}'$ point, suggesting that these bands follow the bulk 1×1 periodicity.

Furthermore, the states were also observed in the other high symmetry directions. ARPES scans along the $[\bar{1}10]$ and the $[\bar{1}12]$ incidence are shown in Fig. 3.12 (a) and (b).

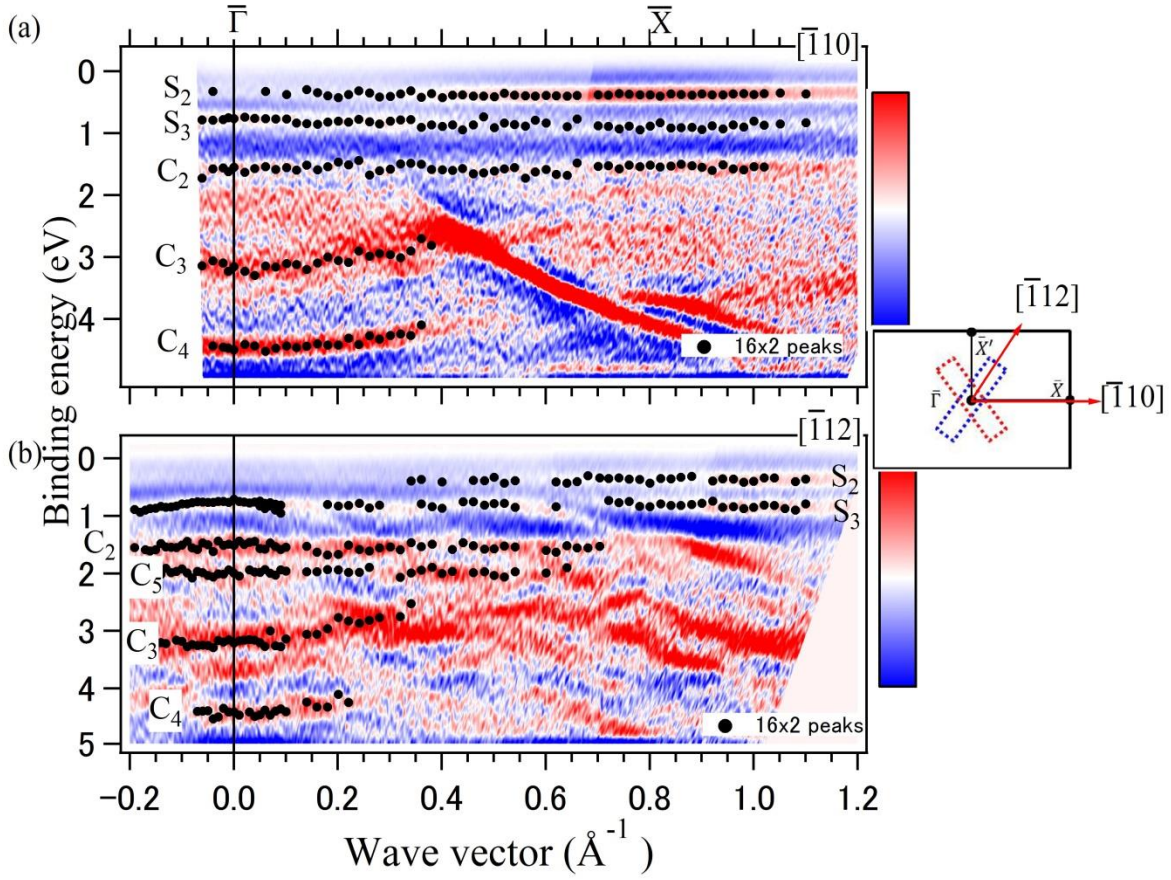

Figure 3.12 2nd derivative intensity map of the ARPES spectra of the Si(110)16×2 surface taken at the (a) [$\bar{1}$10] and (b) [$\bar{1}$12] directions. Peak positions derived from EDCs are overlain as the black circles.

The states observed in Fig. 3.11 appear with the same energy position and dispersion characteristics except for C_4. While C_4 was a parabola dispersing upward and centered at $\bar{\Gamma}_0$, in both Fig. 3.12 (a) and (b), it is clearly less dispersive than that in Fig. 3.11.

The states observed in the ARPES spectra are summarized and compared to the available experimental and DFT calculation results in Table 3-3.

Table 3-3. Comparison of the electronic states observed in this study by ARPES with those reported in the literature from ARPES, STS and DFT data. Also included are the details about the light source used in the ARPES experiments.

	This work (ARPES)	**Cricenti, et al. (ARPES)** [52]	**Kim, et al. (ARPES)** [53]	**Sakamoto, et al. (ARPES, STM)** [54]	**Setvin, et al. (STS,DFT)** [50]	**Ferraro, et al. (DFT)** [56]
Excitation light	Unpolarized 21.2 eV	Unpolarized 21.2 eV	Synchrotron 90 eV	Synchrotron 21.2 eV		
Binding energy of the peak				S_1 ~0.2 eV DBs adatoms	P_1-P_5 ~0.2 eV Pentamers	S_0,S_1 ~0.1-0.15 eV Step edges
					L_0 ~0.33 eV	
	S_2 ~0.4 eV		S_1 ~0.4 eV DBs tetramers	S_2 ~0.4 eV DBs buckled Si	U_1-U_2 ~0.4 eV Upper terrace	S_2,S_3 ~0.35-0.45 eV Upper terrace
	S_3 ~0.8 eV			S_3 ~0.7 eV DBs unbuckled Si	U_2,L_2 ~0.7 eV Upper and lower terrace	S_4 ~0.6 eV Lower terrace
		S_1 ~0.95 eV DBs	S_2 ~0.9 eV DBs adatoms	S_4 ~1.0 eV DBs 2nd layer Si	U_1 ~0.95 eV Upper terrace	S_5 ~0.9 eV SRs
	C_2 ~1.5 eV	S_2 ~1.7-1.9 eV Rest atoms	U_1 ~1.7 eV	C_2 ~1.4 eV Si-Si BBs	P_m ~1.5 eV BBs	S_7 ~1.5 eV SRs
	C_5 ~2.0 eV					S_8 ~2.2 eV SRs
		S_3 ~2.8 eV σ-type BBs	U_2 ~2.7 eV	~2.5 eV		S_9 ~2.6 eV SRs
	C_3 ~3.1 eV			C_3 ~3.2 eV		
	C_4 ~4.5 eV	S_4 ~3.8 eV π-type BBs		~4.2 eV		

Cricenti, *et al*. reported a non-dispersing state similar to C_2 or C_5 at 1.7-1.9 eV [52]. It was only observed in the spectra taken at the $[\bar{1}10]$ and $[\bar{1}11]$ directions, but was not visible in the $[001]$ direction. Kim, *et al.,* also reported a state in the similar energy region (Fig. 3.8(b)), U_1 at 1.7 eV [53].

Sakamoto, *et al.*, also reported observing the C_2, C_3 and C_4 bands with the same energy positions (Fig. 3.8 (a), (c) and (d)) and dispersion characteristics [54]. In their LDOS mapping of C_2 (1.4 eV), they observed that this state is from the orbitals of Si atoms located slightly off the pentamers on the surface. From their proposed AB model, they assigned this C_2 state as a 16×2 surface state from the backbonds of the adatoms [54].

3.3.2. Surface resonances of the Si(110)16×2 surface

For the bands located within the projected bulk bands, the assignments done by the three studies mentioned above are still just highly speculative. To clarify the identity of these bands experimentally, the following can be done [8]:

1) Observing the photon energy-dependence of the band dispersion.
2) Observing the polarization vector-dependence of the photoelectron peak intensity.
3) Observing the dependence of these states on surface treatments.

Cricenti, *et al*., showed that by allowing the Si(110)16×2 surface to be contaminated by residual gasses in the UHV chamber the states they observed disappeared [52]. This is highly indicative of the surface sensitivity of these states.

Fig. 3.13(b and c) shows selected ARPES spectra taken along the [001] direction from different surface reconstructions on the Si(110) surface induced by Bi and In adsorbates in this study.

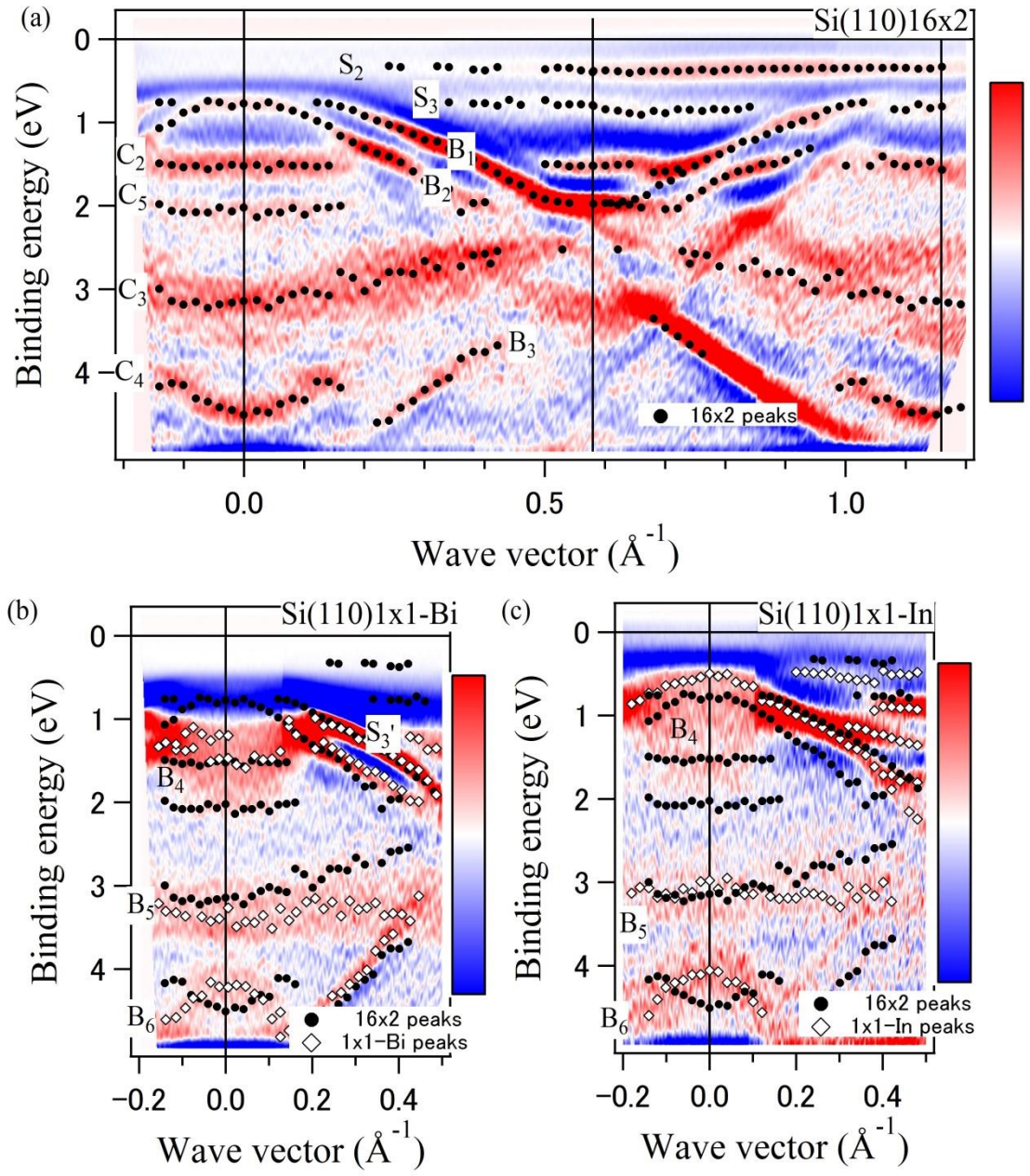

Figure 3.13. ARPES 2nd derivative intensity map taken at the [001] direction of the (a) Si(110)16×2, (b) Si(110)1×1-Bi, and (c) Si(110)1×1-In surfaces. The peak positions of the 16×2 are overlaid as black solid circles while the 1×1 peaks are white solid diamonds.

A complete summary of the 2nd derivative intensity maps of the ARPES spectra of the different Bi-adsorbed Si(110) surfaces are shown later in Fig. 4.14 and 4.15. The peak positions obtained from the EDCs of the clean 16×2 (●) and metal-adsorbed surfaces (◊) are both overlaid on the intensity maps in Fig. 3.13 (b) and (c). More detailed reports of the band structures of the different surface reconstructions are presented in Chapter 4 for Bi- and Chapter 5 for In- induced reconstructions.

The reported 16×2 surface states (S_1-S_4 and C_2) [54] are no longer observed in the metal-adsorbed surfaces (Fig. 3.13 (b) and (c)). This is further evidence of the identification of these as 16×2 surface states. The bulk Si states B_1-B_3 did not change by metal-adsorption on the surface, except for the energy shifts due to band bending on the Si(110)1×1-In surface (Fig. 3.13 (c)).

For the other 16×2 states in the projected bulk bands (C_3-C_5), they are also not observed in the metal-adsorbed surfaces. Other states (B_4-B_6) are observed in the same energy regions instead, but the dispersions are significantly different.

At ~2.0 eV, C_5 is non-dispersing in the 16×2 surface (Fig. 3.13 (a)). In the metal-adsorbed surfaces, a state B_4 is observed with the same binding energy at the $\bar{\Gamma}_0$ point but is dispersing upward. At ~3.2 eV, C_3 is dispersing upward in the 16×2 surface but is non-dispersing over a wide $k_{\parallel}$-range in the metal-adsorbed surfaces (B_5). At ~4.2 eV, C_4 is parabola-like, opening upwards in the 16×2 surface. In the metal adsorbed surfaces, B_6 appears to be parabola-like and opening downwards at the $\bar{\Gamma}_0$ point.

In the 16×2 surface, C_3 and C_4 are located at the $\bar{\Gamma}_0$ point and are reproduced at the $\bar{\Gamma}_1$ point due to the 1×1 periodic potential as shown in Fig. 3.13 (a). In the metal adsorbed surfaces, C_3 has completely disappeared. C_4 on the other hand, can still be observed in the $\bar{\Gamma}_1$ points of the 1×1 SBZs. This suggests that the bonding orbitals

responsible for C_4 are still present in the metal-adsorbed surfaces, with some minor perturbations.

Similar trends are also seen in Pb-adsorbed Si(110) surfaces, as reported in ref. [59], where the 16×2 surface states (S_1-S_4) and surface resonance states (C_2-C_5) are no longer observed or their dispersion is changed drastically.

C_3-C_5 can thus be assigned as 16×2 derived surface resonance states. The wave functions of such states are still highly localized within the surface, but penetrate more into the bulk when compared to pure surface states [8]. Possible origins of these surface resonance states are the Si atoms in the layers underneath the 16×2 reconstruction. Their position in the projected bulk bands suggests that they originate from backbond states. Backbond states are generally less disturbed than the dangling bond states, thus their energy levels are less shifted from the bulk states [8]. These backbond states are between the topmost Si atoms comprising the 16×2 reconstructions and the Si atoms in the ideal Si(110) positions below them.

The states B_4-B_6, which were observed in the metal-adsorbed Si(110) surfaces (Fig. 3.13 (b) and (c)), regardless of the metal species or the periodicity of the new superstructure, can also be attributed to similar backbonds. Metal adsorption on the Si(110) surface can result in a wide variety of surface reconstructions, but the underlying surface is still the ideal Si(110)1×1. Similar to the 16×2 surface resonances C_3-C_5, the states B_4-B_6 can be attributed to backbonds between the subsurface Si atoms and either the metal adsorbates or the topmost Si atoms.

3.3.3. Further Discussions

Anisotropic dispersion of C_4

Another interesting feature observed in these surface resonance states was the dispersion characteristics of the state C_4. The state C_4 is more dispersive along the [001] direction (Fig. 3.11), as compared to the spectra taken along the $[\bar{1}10]$ (Fig. 3.12 (a)) and $[\bar{1}12]$ (Fig. 3.12 (b)) directions. This is contrary to the expected anisotropy in these surface states. On the 16×2 surface, possible anisotropic states should be more dispersive along the terrace directions, either $[\bar{1}12]$ or $[1\bar{1}2]$ (Fig. 3.3, 3.6-7), where there should bigger overlaps of the Si orbitals as compared to directions across these terraces. On the ideal Si(110)1×1 surface, larger wave function overlap is expected along the zigzag Si chains, the $[\bar{1}10]$ direction (Fig. 3.1). This suggests that there is an additional bonding configuration of the Si atoms in the subsurface region that is different from both the bulk Si and the ideal Si(110)1×1 surface. One possible configuration is the buckling of subsurface Si atoms suggested in the AB model [54], as shown in Fig. 3.7. This buckling can cause the larger overlap of the Si orbitals along the [001] direction. However, theoretical calculations will be necessary for confirm the exact origins of these states.

3.4. Conclusions

In summary, the electronic structure of the clean Si(110)16×2 surface was studied in detail by ARPES and the ambiguous electronic states located in the bulk bands were systematically studied. The previously reported 16×2 surface states in the bulk band gap were confirmed in these experiments. Furthermore, by changing the surface structure by metal-adsorption, it was shown that three of the electronic states deep in the bulk valence bands were 16×2-derived surface resonances. This study

provided the first experimental identification of the states located within the projected bulk bands, and these were distinguished as either bulk-derived (B_1-B_3) or 16×2-derived surface resonances (C_3-C_5). The identification of these states as 16×2-derived surface states provides additional experimental results about that can be used to validate structural models proposed for this surface. The results of this study also showed interesting features in the ARPES spectra, such as the unique anisotropic dispersion of the 16×2 surface resonance state, C_4, and the subsurface states (B_4-B_6) that appear on all metal-adsorbed Si(110) surfaces.

Chapter 4. Atomic and electronic structures of Bi-adsorbed Si(110) surfaces

The semimetal Bismuth has been among the most studied elements in solid state physics. It is the most diamagnetic, has the highest Hall coefficient, has a very high resistivity and low heat conductivity [19]. Its unique properties are derived from its unique electronic structure, making it widely studied as a bulk material, as surfaces and as a thin film. The review article by Ph. Hofmann [60] about the structural and electronic properties of Bismuth surfaces contains a more thorough summary about Bismuth and its various low index surfaces. Furthermore, the experimental observation of relativistic quasiparticles being observed on solids [4] has significantly increased the interest on Bi. In fact, in the past 10 years, Bi has played a significant role in the discovery of a new class of materials, the topological insulators [5, 61].

Despite being widely studied as a bulk material, as surfaces or as thin films on various substrates, very little is known about Bi adsorbed on the Si(110) surface. The highly anisotropic nature of the ideal Si(110)1×1 makes it an interesting substrate for the growth of self-assembled 1D metallic chains. However, no such investigations have been done on the Si(110) surface. In fact, there are only a handful of published reports on the Si(110) surface and these were just studies investigating the surface reconstructions.

In this chapter, the atomic and electronic structures of Bi-adsorbed Si(110) surfaces are investigated by RHEED and ARPES. In section 4.1.1, a brief introduction about Bismuth is provided. Some of the interesting properties of Bi as a bulk, as low index surfaces, and as adsorbates or thin films on semiconductors are introduced. Next,

in section 4.1.2, a brief overview of the available literature on the Bi/Si(110) system is presented. Next, section 4.2 briefly describes some important details about the experiments performed in this section.

Section 4.3.1 details the growth of Bi on the Si(110) surface, the different surface reconstructions formed. New reconstructions were found in these experiments and analysis of their RHEED patterns revealed a possible highly disordered quasi one-dimensional surface. The results of these experiments were collated into a more complete and updated phase diagram of the Bi/Si(110) system.

Section 4.3.2 details the electronic structure of the different Bi-adsorbed Si(110) surfaces. Results of the ARPES spectra are discussed here. This section revealed the semiconducting surfaces of the these Bi-adsorbed Si(110) surfaces. The ARPES spectra also revealed the presence of three states in the bulk band gap of the Si substrate. Two of these states are identified as surface states, while the third one was assigned as a defect state.

In section 4.3.3, the results of the previous two sections are integrated, and structural models are proposed for the Bi-adsorbed Si(110) surfaces. These Bi-adatom models were found to satisfactorily explain the RHEED and ARPES results. These structural models can also be adapted to elucidate surface structures of similar reconstructions on Si(110) surfaces adsorbed by different metals.

4.1. Introduction

4.1.1. Bismuth

The Bismuth crystal can be described by a rhombohedral structure (space group $R\bar{3}m$), which is typical for group V elements. The rhombohedral lattice can be generated by using three vectors (green lines in Fig. 4.1 (a)) with equal length $(a_{rh} =$

4.7236Å) with an angle α ($\alpha = 57.35°$) between any two primitive vectors. The three primitive vectors are shown as the green solid lines in Fig. 4.1 (a). Each atom is covalently bonded to its three nearest neighbor atoms. This crystal forms puckered bilayers oriented perpendicularly to the rhombohedral [111] direction. Bismuth can also be described using a hexagonal unit cell, with the trigonal axis (C_3 in Fig. 4.1(a)) as the c-axis ($a = 4.5332\text{Å}$ and $c = 11.7967\text{Å}$). The pink solid lines in Fig. 4.1 (a) are the vectors spanning the hexagonal unit cell.

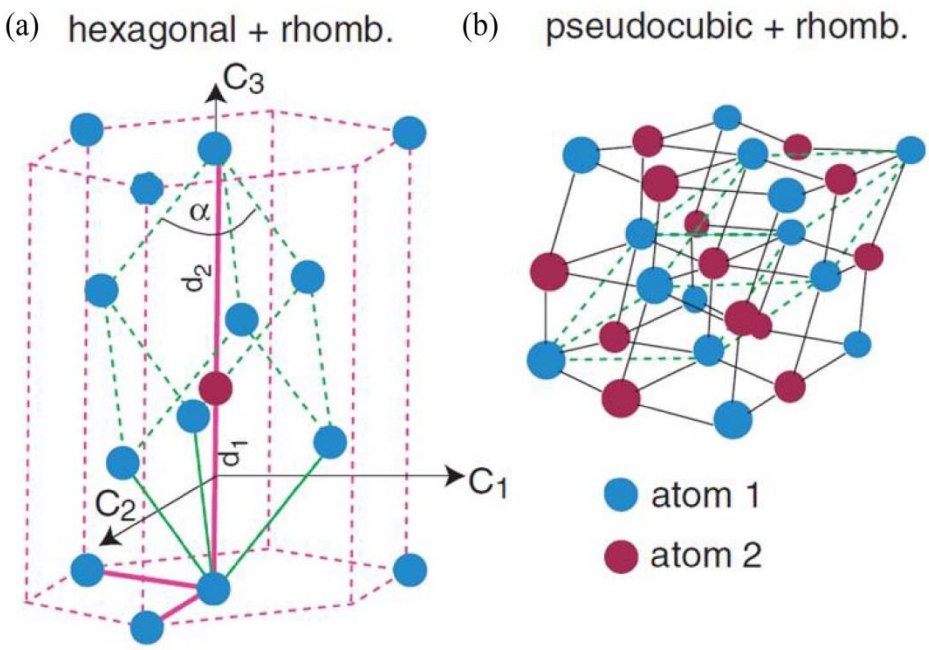

Figure 4.1 The different unit cells used to describe bulk Bismuth: (a) the rhombohedral unit cell (green lines) and the hexagonal unit cell (pink dashed lines), and (b) the pseudocubic nature of this structure with the rhombohedral unit cell [60].

A pseudocubic structure can also describe the Bi crystal (Fig. 4.1 (b)), but this indexing system is ambiguous and not widely used. A summary of the different indexing of low index surfaces of Bi are shown in table 4-1.

Table 4-1 Indexing of the low index Bi surfaces

Rhombohedral	Hexagonal	Pseudocubic
(100)	$(1\bar{1}01)$	(111)
(110)	$(10\bar{1}2)$	(100)
(111)	(0001)	(111)
$(10\bar{1})$	$(2\bar{1}\bar{1}0)$	(110)

The electronic structure of bulk Bi has several interesting features that are responsible for some of its unique properties. Band structure calculations immediately show the unique aspects of the band structure of bulk Bi. Fig. 4.2 (a) shows results from band structure calculations from the tight-binding calculations done by Liu and Allen [62], and first-principles calculations by Gonze, *et al* [63].

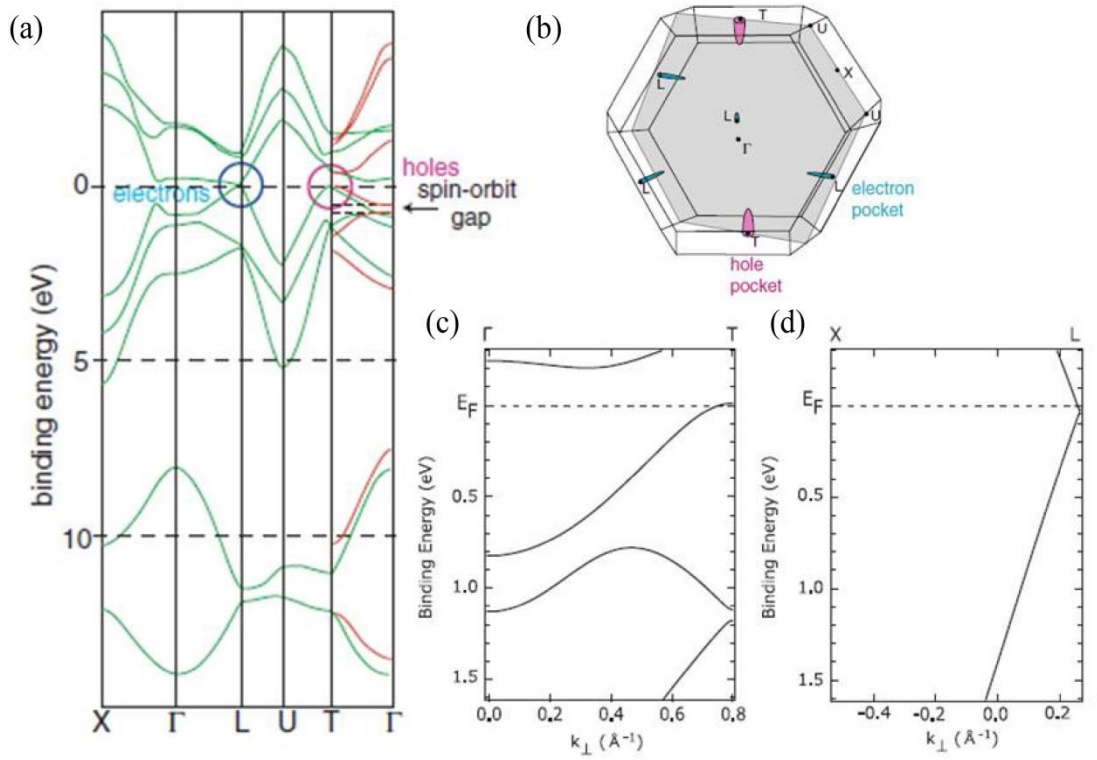

Figure 4.2 (a) Calculations of the band structure of bulk Bi from tight-binding calculations [60, 62] (green lines) and first-principles calculations [60, 63] (red lines), (b) Brillouin zone of bulk Bi [60], and close up of the (c) electron pocket along **Γ-T** and (d) hole pocket along **X-L** [19]**.**

The inclusion of spin-orbit interaction in the first-principles calculations results in a spin-orbit gap in the **T**-point in Fig. 4.2 (a). Bismuth is a heavy element with a strong spin-orbit splitting (1.5 eV between $p_{3/2}$ and $p_{1/2}$). However, because of the bulk inversion symmetry $\left(E(\vec{k},\uparrow) = E(-\vec{k},\uparrow)\right)$ the degeneracy of the bands in the bulk dispersion is not lifted.

On the surfaces however, the bulk inversion symmetry is lifted and has resulted in the observation of strong spin-orbit splitting in both calculations and ARPES experiments (Fig. 4.3 (a-c)).

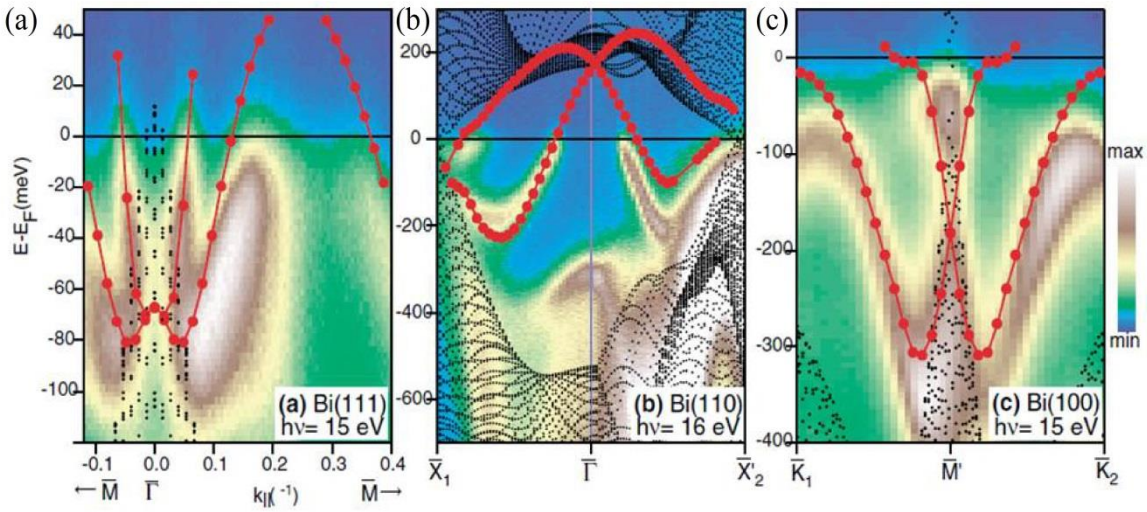

Figure 4.3. Spin-orbit splitting observed by ARPES and calculations on (a) Bi(111), (b) Bi(110) and (c) Bi(100) surfaces. Small black dots are the projected bulk bands and the red circles are the calculated surfaces states [64].

4.1.2. Bismuth on semiconductor surfaces

The novel electronic phenomena observed on Bi have also led to the investigation of Bi thin films and overlayers, where the bulk inversion symmetry is also expected to be broken. Furthermore, the low Fermi energy and the small effective mass of the carriers in Bi lead to a long de Broglie wavelength$\left(\lambda_B \sim 200 - 300\text{Å}\right)$. From quantum mechanics, when the size of the material is reduced, such that it becomes

comparable to, or smaller than the de Broglie wavelength, quantum size effects (QSE) are observed. This results in interference and quantization of the electronic states (i.e. formation of quantum well states (QWS) or subbands) [19]. These QSEs have led to the increased motivation in the study of Bi thin films [19] and other nanostructures.

The emergence of semiconductor-based spintronics has also contributed to the increased motivation in the study of semiconductor surfaces adsorbed with metals with strong spin-orbit coupling (SOC). For the application of these material systems in spintronic devices, the following requirements are necessary [65]:

1) generation of spin-polarized electrons through the Rashba effect with large enough spin-splitting,
2) the spin-split states should be metallic to allow significant spin transport,
3) the substrate should be semiconducting to reduce signal from spin degenerate electron transport.

The Rashba effect is the momentum-dependent lifting of the spin degeneracy of bands due to strong SOC and the breaking of the bulk inversion symmetry along the surface normal direction, which can be observed on metal surfaces, metal-oxide surfaces, interfaces in heterostructures and between heavy element monolayer or thin films and a bulk substrate. There has been step-by-step progress made, beginning with the observation of Rashba type spin-split surface states on metal surfaces [64, 66], and was eventually followed by the experimental observation of spin-split surface states on various metal films or overlayers on different semiconducting surfaces. The strong SOC of Bi makes it one of the most investigated film/overlayer material on various semiconductor surfaces [19, 20, 67, 68]. This search for these metallic Rashba-type

spin-split states on semiconductor surfaces for applications in Si-based spintronic devices continues [34].

4.1.3. Bismuth on Si(110)

Despite the considerable interest in Bi thin films or nanostructures on semiconductor surfaces, it has not been fully investigated on the Si(110) surface. The strong SOC of Bi and the anisotropic structure of the Si(110) substrate makes it possible to create 1D wires that can host a 1D Rashba system on the surface, similar to that observed on the Pt-adsorbed Si(110) surface [33]. Aside from possible applications in spintronic devices, 1D structures with strong SOC are an essential component in the proposed experiments to observed the elusive Majorana fermions in solids [69, 70].

An early study by Oyama, *et al.* [71] investigated the low coverage adsorption of Bi on Si(110). Using QMS, LEED and Auger electron spectroscopy (AES), they observed two 2D phases and one 3D phase of Bi on Si(110). They reported that the 2D phases were only observed when Bi was deposited on Si(110) substrates held at temperatures above 300°C, and that Bi grows in the Stranski-Krastanov (SK) mode (layer plus island growth mode) [8, 71]. From their analysis of the LEED patterns, they identified the 2D phases as 3×2 and 1×1 reconstructions which have Bi coverages of $1/6$ ML and $1/3$ ML respectively.

An STM study later showed that these 3×2 surfaces are well ordered and that phase boundaries were hardly seen (Fig. 4.4 (a) and (b)) [72]. They suggested that these domains align at supposed anti-phase boundaries when the different domains contact each other. They also found that room temperature (RT) deposition of Bi on Si(110) formed Bi clusters all over the surface.

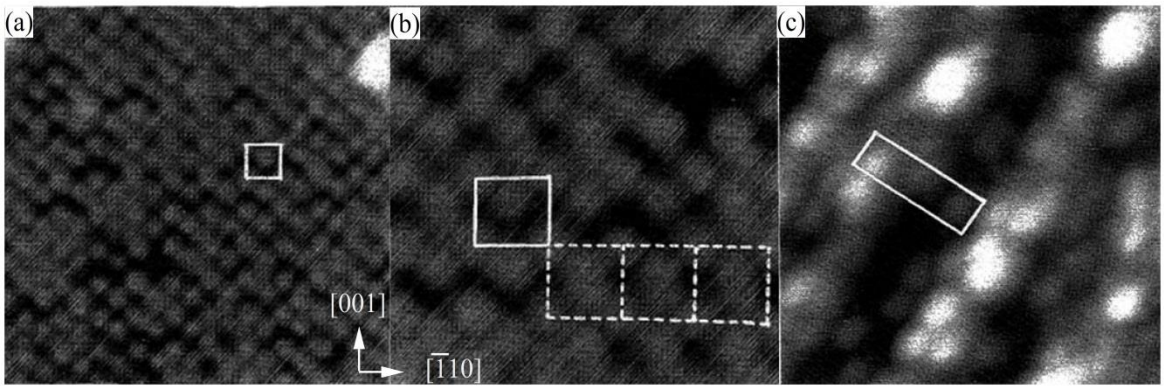

Figure 4.4 (a) 12×12nm^2 and (b) 6×6nm^2 STM filled state images of the Si(110)3×2 surface and (c) 15×15nm^2 empty state image after Bi deposition at RT [72].

Their STM images also showed that the 3×2 unit cell consists of Bi adatoms on top of the ideal Si(110)1×1 surface (Fig. 4.4(a)). They suggested that the Si atoms on the 16×2 protrusions are mobile enough and fill in the lower terraces, leaving a flat ideal Si(110) surface.

For the 1×1-Bi surface, I-V curves from tensor LEED experiments suggested only a short range order in the Bi structure [73]. The strong diffuse background in the LEED patterns from the Si(110)1×1-Bi surface prepared at substrate temperatures below 300° suggested that the Bi domains formed are randomly oriented and have no long range order [71].

The goal of this chapter is to investigate Bi growth on Si(110) substrates held at high substrate temperatures and to investigate the electronic structure of these Bi-adsorbed Si(110) surfaces. To do this, the surface of the Si(110) was observed *in-situ* by RHEED during Bi deposition at various metal coverage and substrate temperatures. The results of these experiments were collated into a complete phase diagram for the Bi/Si(110) system. Furthermore, the electronic band structure of the different surfaces of the Bi/Si(110) system was investigated by ARPES. Results of the RHEED and ARPES

experiments were integrated and discussed in terms of proposed structural models of these surfaces.

4.2. Experimental procedures

The growth of Bi on Si(110) surfaces were studied by *in-situ* RHEED experiments. The clean Si(110)16×2 surfaces were prepared following the procedure laid out in section 3.2. The samples were first flash annealed several times at 1250°C, followed by an annealing step at ~600°C [31, 57]. The clean Si(110)16×2 surface was confirmed by observing the RHEED patterns.

Bismuth was evaporated from a Knudsen cell and deposited on the Si(110)16×2 surface at various Bi coverages and substrate temperatures. The Bi deposition rate was calibrated using the wetting layer of a Bi thin film grown on the Si(111) surface [74]. The substrate temperature was controlled using the annealing current. The current was calibrated with temperature as observed by an infrared pyrometer and a IR thermography camera.

In the ARPES measurements, monochromatized light from a He discharge lamp (He I α, $h\nu$ = 21.21 eV) were used to access the bands close to E_F. For Bi core-level photoelectron spectroscopy, He II α ($h\nu$ = 40.81 eV) was used. All photoelectron spectroscopy experiments were done in ambient room temperature. The energy resolution for the measurements close to E_F was 5 meV, while for the Bi core-level scans, it was 10 meV.

4.3. Results and discussion

4.3.1. Bi growth and surface reconstructions on Si(110)

Oyama, *et al*., first reported the formation of 2D Bi phases on the Si(110) surface [71]. These 2D phases occur only when Bi is deposited on Si(110) substrates held at temperatures above 300°C. A summary of Bi deposition on Si(110) surfaces derived from the report by Oyama [71] is shown Fig. 4.5.

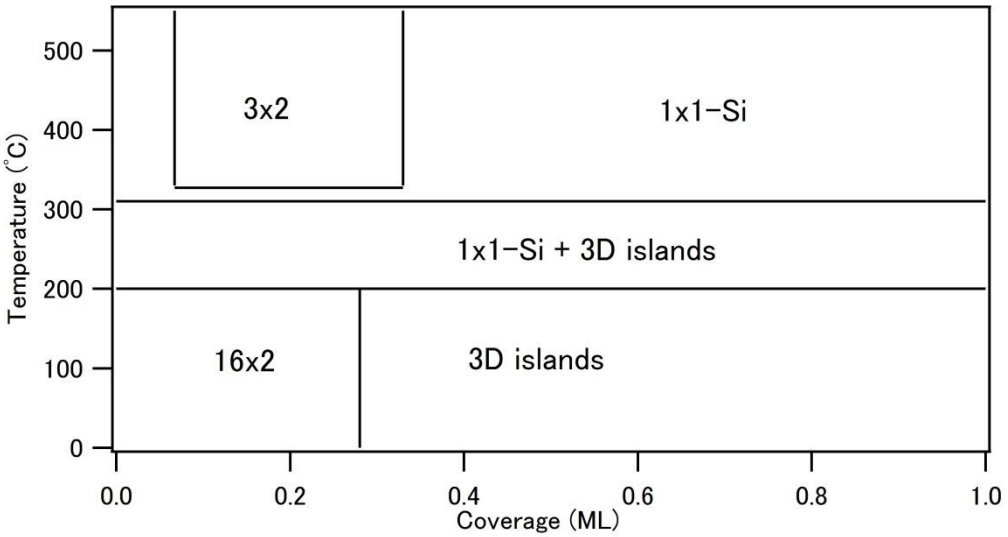

Figure 4.5 Phase diagram of Bi deposition on Si(110) at various substrate temperatures summarized from ref. [71].

Above 300°C, a 3×2 reconstruction is formed at 1/6 ML Bi [71], where 1 monolayer (ML) is the areal density of the ideal Si(110) surface (9.6×10^{14} cm^{-2}). Fig. 4.6(a) and (b) show representative RHEED patterns taken from the Si(110) 3×2-Bi surface. Sharp fractional $n/3$ spots can be seen in the half-ordered Laue zone circle ($L_{1/2}$) in the RHEED pattern taken at the [001] incidence (red arrows in Fig. 4.6(a)), indicating a ×3 periodicity along the $[\bar{1}10]$ direction and a ×2 periodicity along the perpendicular [001] direction. The same periodicities can be observed in the RHEED

pattern taken at the $[\bar{1}10]$ incidence directions in Fig. 4.6(b). Sharp $n/2$ fractional order spots are seen in the $n/3$ Laue zones (green arrows in Fig. 4.6(b)).

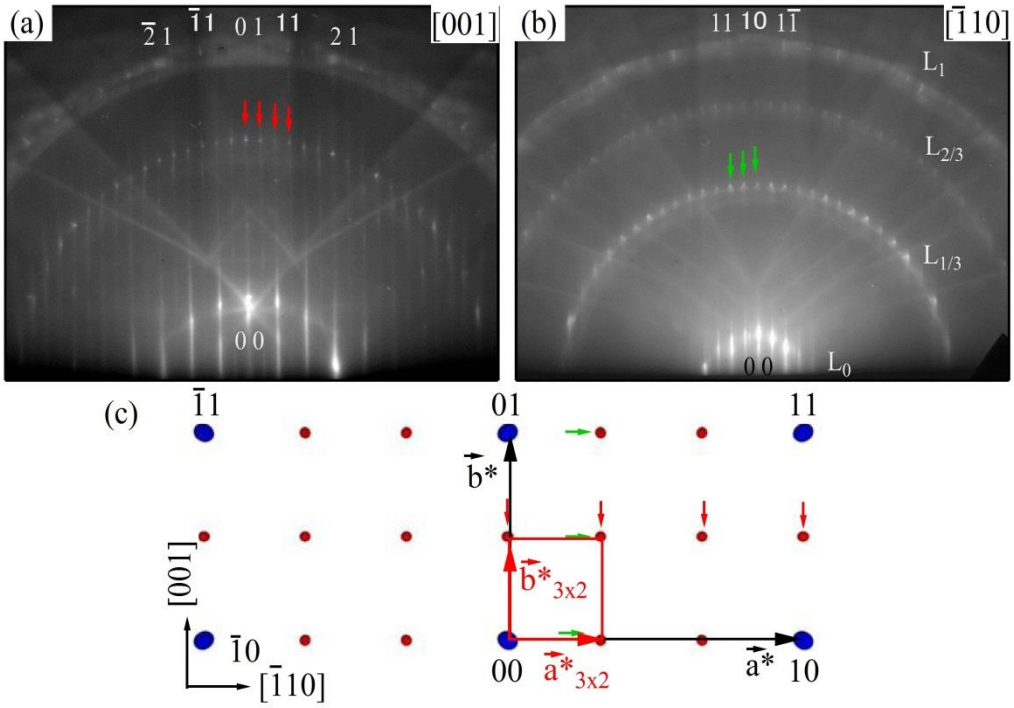

Figure 4.6 RHEED patterns of the Si(110)3×2-Bi surface taken at the (a) $[001]$ and (b) $[\bar{1}10]$ incidence directions, and (c) its corresponding reciprocal lattice.

The reciprocal lattice vectors of the Si(110)3×2-Bi are,

$$\mathbf{a}^*_{\mathbf{3\times2}} = \frac{1}{3}\mathbf{a}^* \text{ and } \mathbf{b}^*_{\mathbf{3\times2}} = \frac{1}{2}\mathbf{b}^* \qquad (32),$$

and the real space vectors are,

$$\mathbf{a}_{\mathbf{3\times2}} = 3\mathbf{a} \text{ and } \mathbf{b}_{\mathbf{3\times2}} = 2\mathbf{b} \qquad (33).$$

Further Bi deposition at these substrate temperatures results in a 1×1-Si surface as shown in the RHEED patterns in Fig. 4.7(a) and (b).

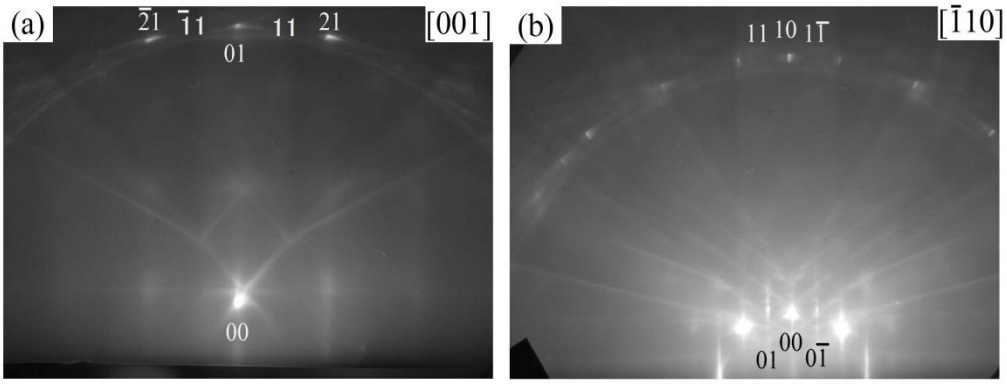

Figure 4.7 RHEED patterns of the Si(110)1×1-Bi surface taken at the (a) [001] and (b) [$\bar{1}$10] incidence directions.

When the substrate is annealed at temperatures above 600°C, new surface reconstructions were found. *In-situ* RHEED experiments during Bi deposition on Si(110) held at 600° showed a new diffraction pattern appearing before the 3×2 pattern emerges.

Figure 4.8 shows the growth of Bi during deposition at 600°C. Images of the RHEED patterns were taken with a CCD camera every 4 sec. during the deposition. An intensity line profile was taken along the 0^{th} Laue zone of the diffraction patterns taken at the [$\bar{1}$10] incidence direction. The region used for the intensity line profile is shown by the rectangles in Fig. 4.8 (a) and (b). The line profile for each RHEED image is then collected and shown as an intensity map in Fig. 4.8 (c). Representative RHEED line profiles are shown Fig. 4.8 (d).

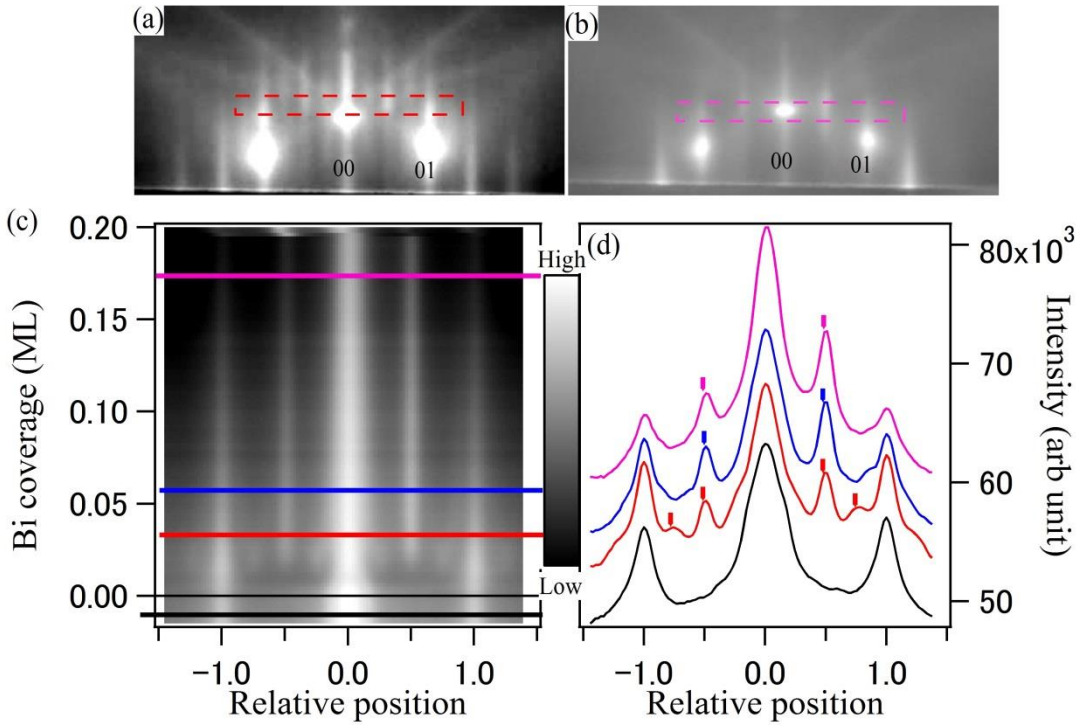

Figure 4.8. RHEED patterns at Bi coverage of (a) 0.026 ML and (b) 0.18 ML, taken along the [$\bar{1}$10] incident direction during Bi deposition at 600°C. (c) Intensity map of the line profiles taken across the rectangles marked in (a) and (b) during Bi deposition plotted vs Bi coverage and (d) line profiles taken at various Bi coverages.

Fig. 4.8 (c) shows that before a well ordered diffraction pattern of the 3×2 surface appears at ~0.10 ML (Fig. 4.8 (b) and the pink line profile in Fig. 4.8 (d)), additional spots appear. Fig. 4.8 (a) shows the RHEED pattern at 0.026 ML, where the fundamental spots 00 and 01 are divided into four by fractional order spots. These n/4 spots can be seen slowly disappearing upon further Bi deposition. Figure 4.9(a) and (b) shows the RHEED patterns of the Si(110) surface after deposition of 0.1 ML Bi at a substrate temperature of 600°C.

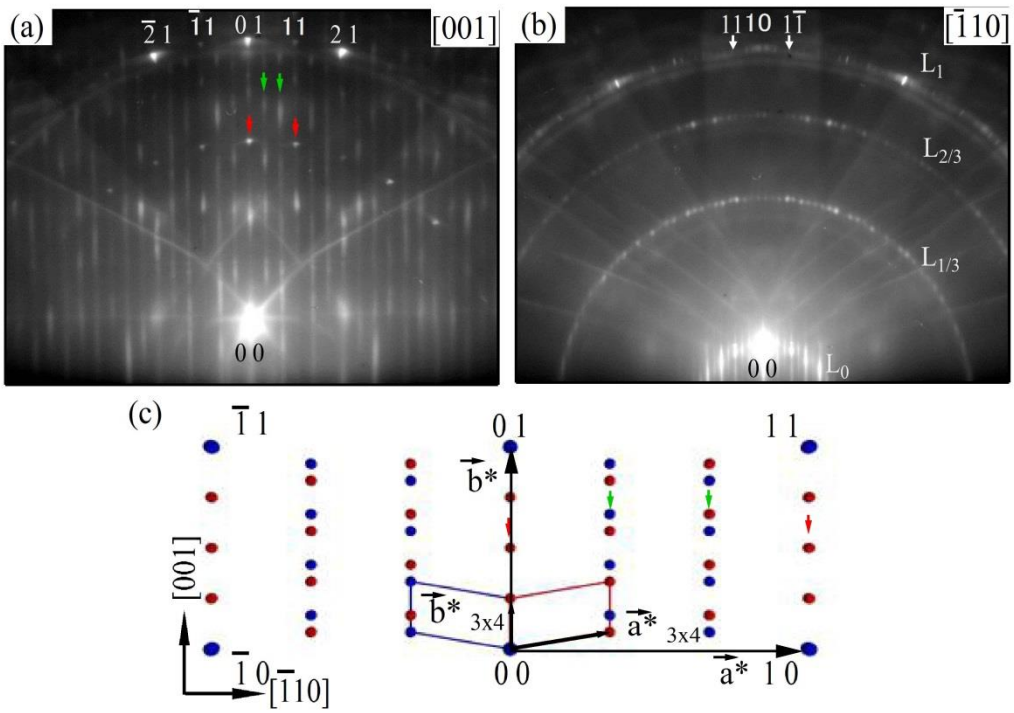

Figure 4.9 RHEED patterns of the Si(110)3×"4"-Bi surface taken at the (a) [001] and (b) [$\bar{1}$10] incidence directions, and (c) its corresponding reciprocal lattice, with the unit cells of the double domain structure.

In the RHEED pattern taken at the [001] incidence direction (Fig. 4.9(a)), fractional order $n/3$ streaks are observed between the 00 and 10 fundamental spots. This is similar to the $n/3$ spots observed in the 3×2-Bi phase, as was shown in Fig. 4.6(a). This indicates that this new reconstruction has the same ×3 periodicity along the [$\bar{1}$10] direction.

At the [$\bar{1}$10] incidence direction, the RHEED pattern shown in Fig. 4.9(b) shows fractional order $n/4$ spots along the 0^{th} Laue zone, this suggests a ×4 periodicity along the [001] direction. However, these $n/4$ spots are not arranged along $n/4$ Laue circles in the diffraction pattern taken at the [001] incidence as shown Fig. 4.9(a). This means that the surface reconstructs into a 3×"4" unit cell, where the 2 unit cell vectors are not orthogonal to each other.

Furthermore, the diffraction patterns taken at the [001] incidence direction shows the coexistence of sharp diffraction spots and elongated streaks (red and green arrows in Fig. 4.9(a)) from the same surface. This will be further discussed later on.

Assuming a double domain structure due a mirror symmetry plane along the [001] direction of the ideal Si(110) surface, the reciprocal lattice vectors was extracted from the diffraction patterns. The reciprocal lattice vectors of the single domain 3×"4" are given by,

$$\mathbf{a}^*_{\mathbf{3\times4}} = \frac{1}{3}\mathbf{a}^* + \frac{1}{12}\mathbf{b}^* \text{ and } \mathbf{b}^*_{\mathbf{3\times4}} = \frac{1}{4}\mathbf{b}^* \qquad (34).$$

In real space, the superlattice can be expressed by the vectors,

$$\mathbf{a}_{\mathbf{3\times4}} = 3\mathbf{a} \text{ and } \mathbf{b}_{\mathbf{3\times4}} = -\mathbf{a} + 4\mathbf{b} \qquad (35).$$

This Si(110) 3×"4"-Bi surface can be more accurately expressed as the $\begin{pmatrix} 3 & 0 \\ \overline{1} & 4 \end{pmatrix}$ structure.

Similar structures have been observed on Si(110) covered with different metals: the Si(110)3×8-Al (0.54 ML) [75], Si(110)"4×6"-Al (0.2 ML) [76] and Si(110)α'-In (0.2 ML) [77] surfaces. The reported coverage and reciprocal lattice vectors interpreted from the diffraction patterns of the 3×8-Al and "4×6"-Al are different, but it is believed that these two surfaces are the same [15]. The metal coverage, substrate temperature and the diffraction patterns for these surfaces are exactly the same as the Si(110)3×"4"-Bi reported here, indicating that these surfaces reconstructs into the same structure.

At substrate temperatures above 630°C, the structural transitions observed during Bi deposition are different from Bi deposition at 600°C. The diffraction pattern of the 3×"4" reconstruction appears at the same Bi coverage region, but it does not

transition to the 3×2 pattern. Instead, a new diffraction pattern was observed to appear. Fig. 4.10 (a) shows the intensity map of Bi deposition at 630°C.

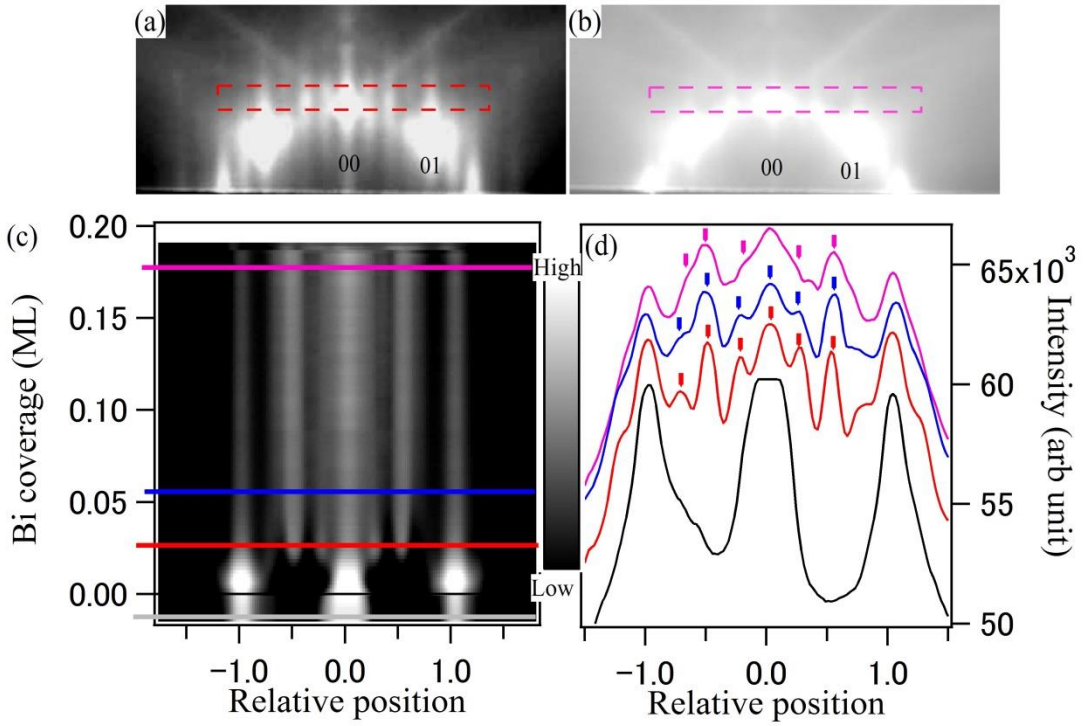

Figure 4.10. RHEED patterns at Bi coverages of (a) 0.022 ML and (b) 0.11 ML, taken along the $[\bar{1}10]$ incident direction during Bi deposition at 630°C. (c) Intensity map of the line profiles taken across the rectangles marked in (a) and (b) during Bi deposition plotted vs Bi coverage and (d) line profiles taken at various Bi coverages.

The $n/4$ spots of the 3×"4" structure can be seen in the line profile (red line in Fig. 4.10(d)) and RHEED pattern (Fig. 4.10(a)) at 0.22 ML. At a Bi coverage of 0.17 ML, $n/6$ are now seen in the line profile (pink line in Fig. 4.10(d)) and RHEED pattern (Fig. 4.10(b)), suggesting that these new reconstruction has a ×6 periodicity along the [001] direction.

The RHEED pattern taken at the [001] incidence (Fig. 4.11(a)) further shows this ×6 periodicity, while the $n/3$ streaks observed between the 00 and 10 fundamental spots suggest that it has the same ×3 periodicity along the $[\bar{1}10]$ direction, similar to the

3×2 and 3×“4” structures. Fig. 4.11(a) also shows the same sharp spots and elongated streaks observed from the 3×“4” suface.

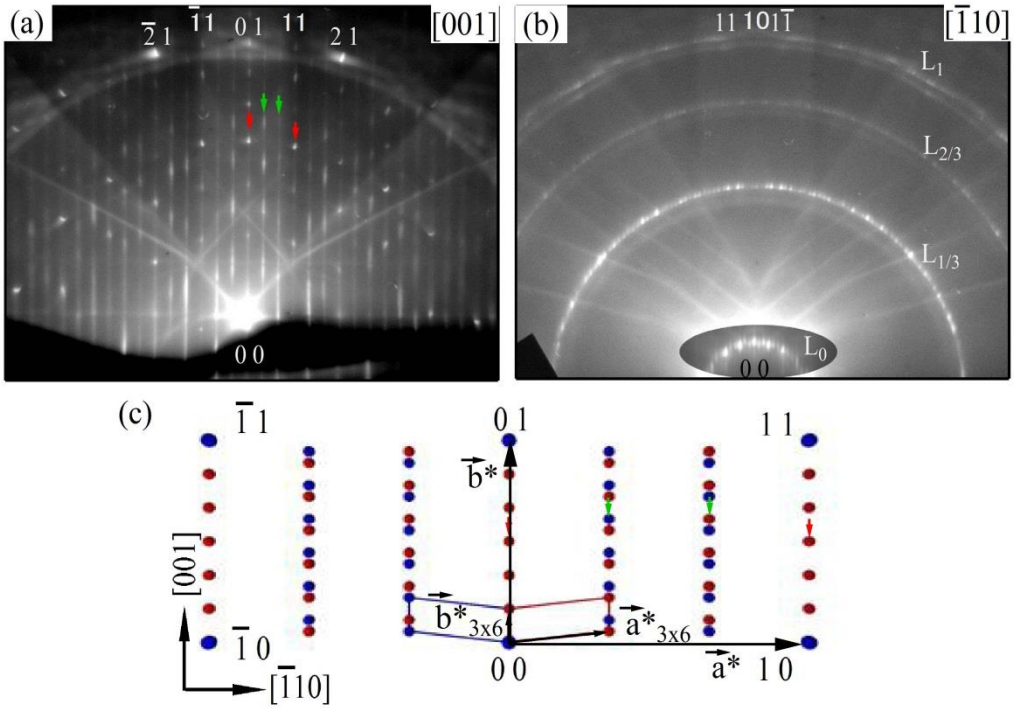

Figure 4.11 RHEED patterns of the Si(110)3×“6”-Bi surface taken at the (a) [001] and (b) [$\bar{1}$10] incidence directions, and (c) its corresponding reciprocal lattice, with the unit cells of the double domain structure.

Using the same arguments used for the 3×“4”, the reciprocal lattice vectors were extracted from the diffraction patterns and are given by,

$$\mathbf{a}^*_{\mathbf{3\times6}} = \frac{1}{3}\mathbf{a}^* + \frac{1}{18}\mathbf{b}^* \text{ and } \mathbf{b}^*_{\mathbf{3\times6}} = \frac{1}{6}\mathbf{b}^* \qquad (36),$$

and the real space unit cell vectors are,

$$\mathbf{a}_{\mathbf{3\times6}} = 3\mathbf{a} \text{ and } \mathbf{b}_{\mathbf{3\times6}} = -\mathbf{a} + 6\mathbf{b} \qquad (37).$$

This structure can be more accurately referred to as the $\begin{pmatrix} 3 & 0 \\ \bar{1} & 6 \end{pmatrix}$ structure. This has been the first observation of this surface reconstruction on the Si(110) surface. The results of these experiments are summarized in more complete Bi/Si(110) phase diagram in Fig. 4.12.

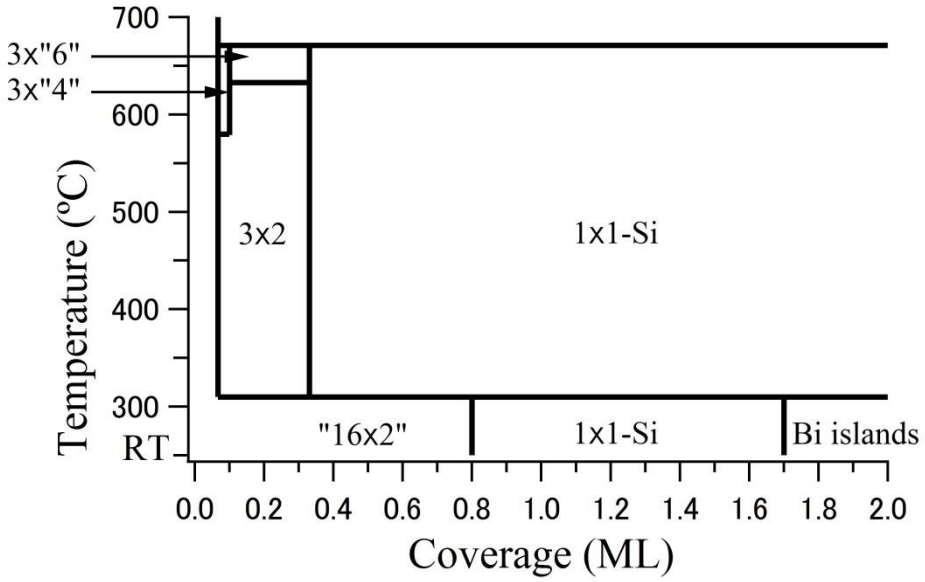

Figure 4.12. Complete phase diagram for the Bi/Si(110) system summarized from this study.

As shown in both Fig. 4.9(a) and 4.11(a), the diffraction patterns of the 3×"4" and 3×"6" surfaces exhibit the coexistence of sharp diffraction spots and streaks (red and green arrows in both figures). The sharp fractional order spots occur at reciprocal lattice points $\mathbf{G_1} = 3h\mathbf{a_s^*} + k\mathbf{b_s^*}$, h and k are integers, and the intensity modulated streaks along the [001] direction have higher intensities at the positions of the reciprocal lattice points $\mathbf{G_2} = (3h \pm 1)\mathbf{a_s^*} + k\mathbf{b_s^*}$, where $\mathbf{s}$ refers to either the 3×"4" or 3×"6" surface.

Several conclusions can be made from the direction and length of these streaks. First, the coexistence of the sharp spots and streaks suggest the presence of antiphase domain boundaries on the surfaces, similar to those observed by Daimon, *et al.* [78] and Yeom, *et al.* [16]. This kind of diffraction pattern is analogous to a quasi-one-dimensional system where the scatterers on the surface are arranged in lines with disorder perpendicular to the lines introduced by random shifts of scatterers along these lines of scatterers [39].

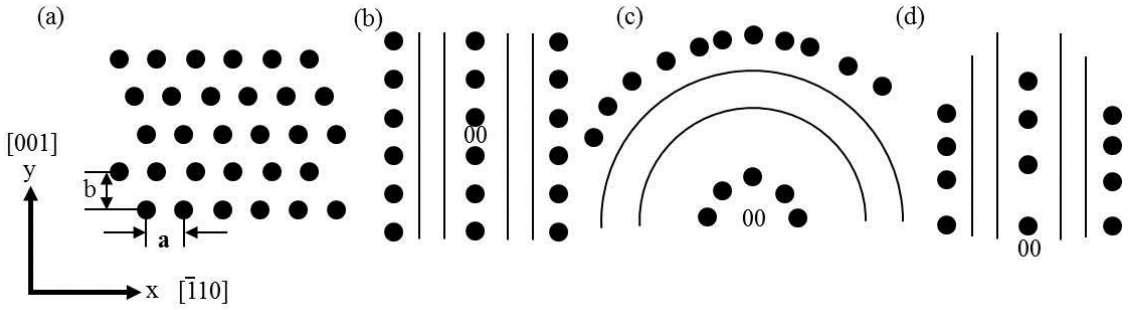

Figure 4.13. (a)Schematic diagrams of a pseudo-one dimensional arrangement of scatterers along x, (b) the reciprocal lattice of this structure and the RHEED patterns taken at the (c) x-incidence and (d) y-incidence.

The direction of the streaks in Fig. 4.9(a) and 4.11(a), running along the $[001]$ direction suggests that some disorder exists along the $[001]$ direction [39, 77]. This could mean that the scatterers are aligned along the $[\bar{1}10]$ direction, with random shifts along the $[\bar{1}10]$ direction causing the disorder along $[001]$.

The intensity modulations along these streaks also reveal valuable information. Completely random shifts of the scatterers, with no correlation in the disorder, will result in long continuous streaks with an almost constant intensity distribution (Fig. 4.13 (d)) [39, 78]. The streaks observed in this study exhibit some intensity modulations, where the intensity is maximum near the reciprocal lattice points of the superstructure. Between these points, the intensity drops along the streaks, but faint lines of intensity can still be observed. This indicates that some correlation exists in the disorder, i.e., the shifts of the scatterers are not completely random.

The sharp spots in the diffraction patterns also reveal further information. A modified version of the diffraction amplitude in eq. (24) in section 2.2 for a pseudo-1D crystal with random displacements, *d*, of the scatterers along the $\hat{x}$ ($[\bar{1}10]$) direction (Fig. 4.12 (a)) can be expressed as:

$$A(s) = \sum_{m,n} g(X_n)\exp(iS_x na + iS_y mb) \qquad (38),$$

where $g(X_n)$ is the disorder term and is expressed as,

$$g(X_n) = \begin{cases} 1 & \text{if d} = 0 \\ \exp(iS_x d) & \text{if d} \neq 0 \end{cases} \qquad (39).$$

For both the 3×"4" and 3×"6" surfaces, the sharp spots only appear for reciprocal lattice points $\mathbf{G_1} = 3h\mathbf{a_s^*} + k\mathbf{b_s^*}$. For the 3×"4" surface, using eq. (34) and (35), the reciprocal vector can be written as,

$$\mathbf{S_1} = 3h\left(\frac{1}{3}\mathbf{a}^* + \frac{1}{12}\mathbf{b}^*\right) + k\left(\frac{1}{4}\mathbf{a}^*\right)$$

$$= h\mathbf{a}^* + \left(\frac{h+k}{4}\right)\mathbf{b}^* . \quad (40)$$

S_x in eq. (38) can be written as $S_x = 2\pi h/a$, and thus the disorder term in eq. (38) reduces to 1 if $d = a$. The diffraction amplitude, using eq. (38) now becomes a δ function when m is an integer. The disorder along the $\mathbf{a_{3\times4}^*}$ direction ([001]) does not affect the diffraction at these reciprocal lattice points and the diffraction pattern will show only sharp n/4 fractional order spots.

For the intensity modulated streaks that peak on reciprocal lattice points $\mathbf{G_2} = (3h \pm 1)\mathbf{a_s^*} + k\mathbf{a_s^*}$, it can also be shown that the disorder term $g(X_n)$ will not reduce to 1 and the diffraction amplitude will depend on both $\mathbf{a}^*$ and $\mathbf{b}^*$.

All the surface reconstructions reported here had been observed on both the LR and HR Si(110) wafers.

4.3.2. Electronic structure of Bi-induced superstructures

The electronic structures of the different Bi-induced reconstructions observed in the previous section were investigated by ARPES. All the ARPES spectra of the different Bi-adsorbed Si(110) surfaces are shown together with the Si(110)16×2 spectra in Fig. 4.14 ([001] spectra) and Fig. 4.15 ($[\bar{1}10]$ spectra).

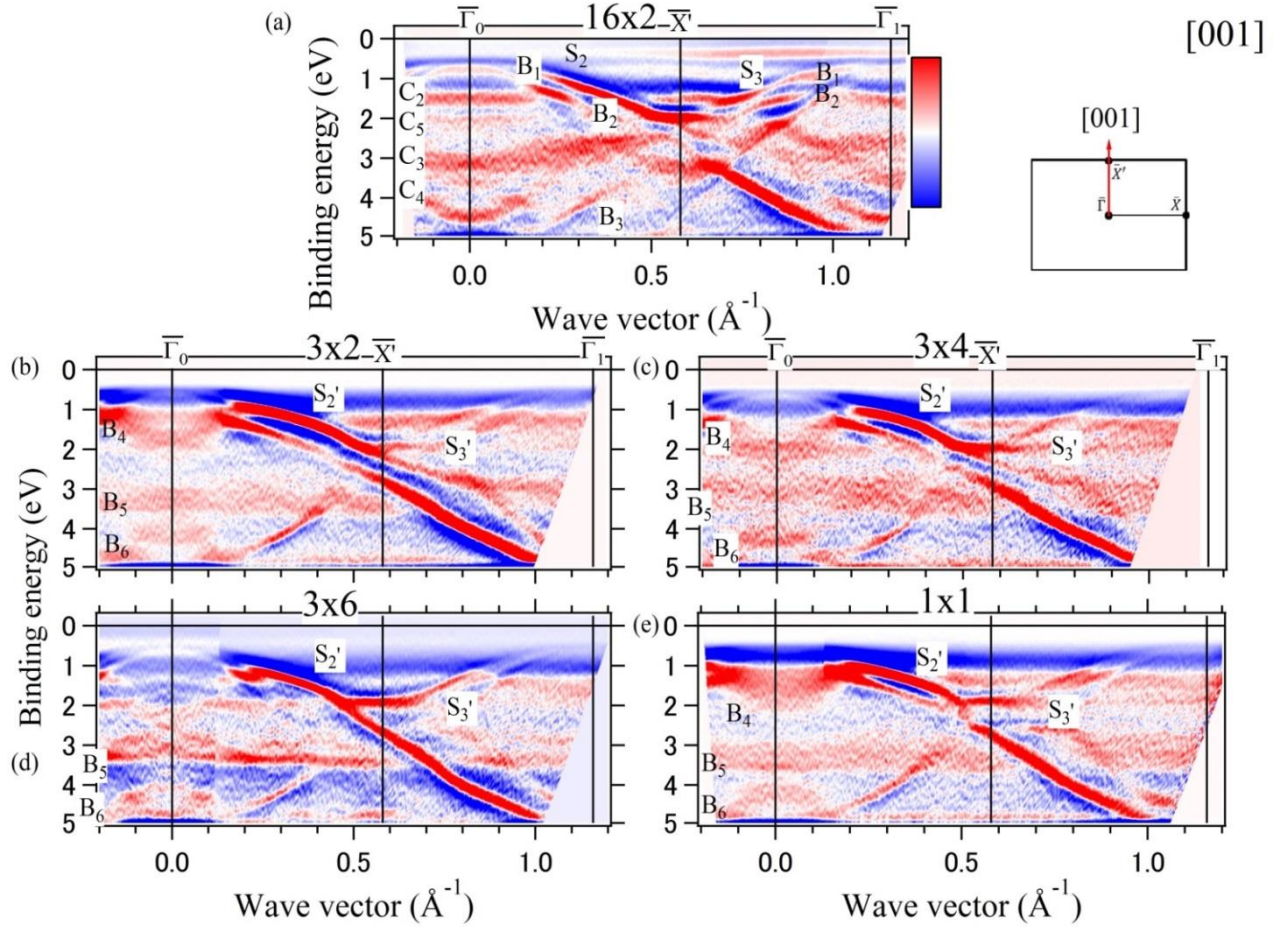

Figure 4.14. Comparison of the 2nd derivative intensity map of the ARPES spectra of (a) Si(110)16×2, (b) Si(110)3×2-Bi, (c) Si(110)3×“4”-Bi and (d) Si(110)3×“6”-Bi and (e) Si(110)1×1-Bi surfaces taken along the [001] direction. Inset: SBZ of the ideal Si(110)1×1.

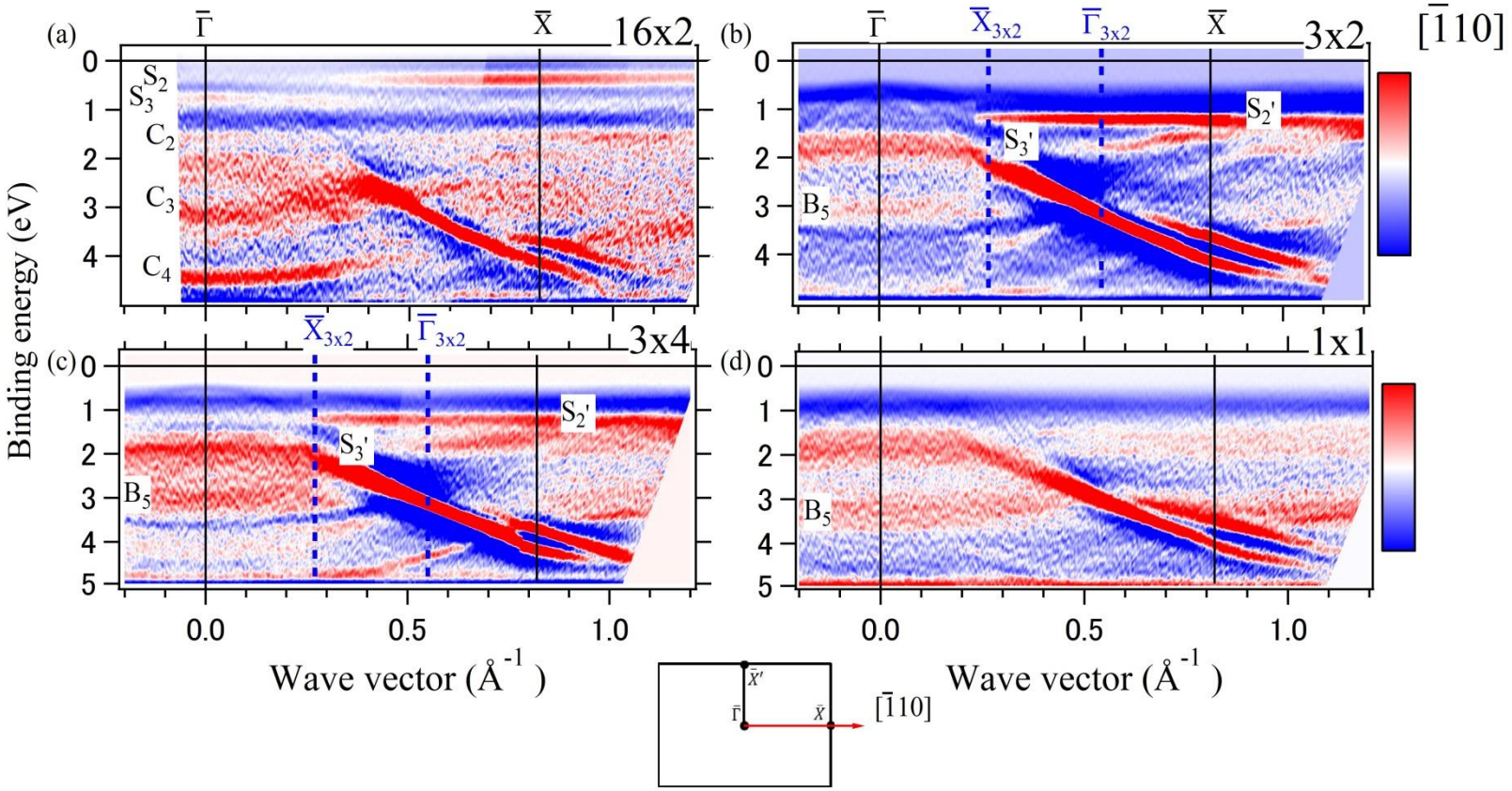

Figure 4.15. Comparison of the 2nd derivative intensity map of the ARPES spectra of the (a) Si(110)16×2, (b) Si(110)3×2-Bi, (c) Si(110)3×"4"-Bi and (d) Si(110)1×1-Bi surfaces taken along the [$\bar{1}$10] direction. Inset: SBZ of the ideal Si(110)1×1.

Fig. 4.16 shows the band structure of the Si(110)3×2-Bi taken along the $\bar{\Gamma}_0 - \bar{X}' - \bar{\Gamma}_1$, [001], direction of the Si(110)1× 1 SBZ. The peak positions are obtained by peak fittings of the EDCs of the raw spectra and are shown as filled circles overlaid over the intensity map in Fig. 4.16(b). In the 2nd derivative intensity map of the ARPES spectra, two electronic states can be seen above the projected bulk band edge (Fig. 4.16(a)): S_2' at 1.25 eV and S_3' at 1.98 eV. S_2' is clearly located within the bulk band gap, while S_3' is right on the edge. Three more states are observed within the projected bulk bands. Non-dispersing B_5 at 3.2 eV, which extends from the $\bar{\Gamma}$ point to boundary of the 1×1 surface Brillouin zone (SBZ), at the $\bar{X}'$ point. Two parabolic bands, B_4 at 1.95 eV at the $\bar{\Gamma}$ point and disperses upward, and B_6 at 4.0 eV the $\bar{\Gamma}$ point and disperses downwards. These three bands were discussed in the previous chapter and will no longer be discussed here.

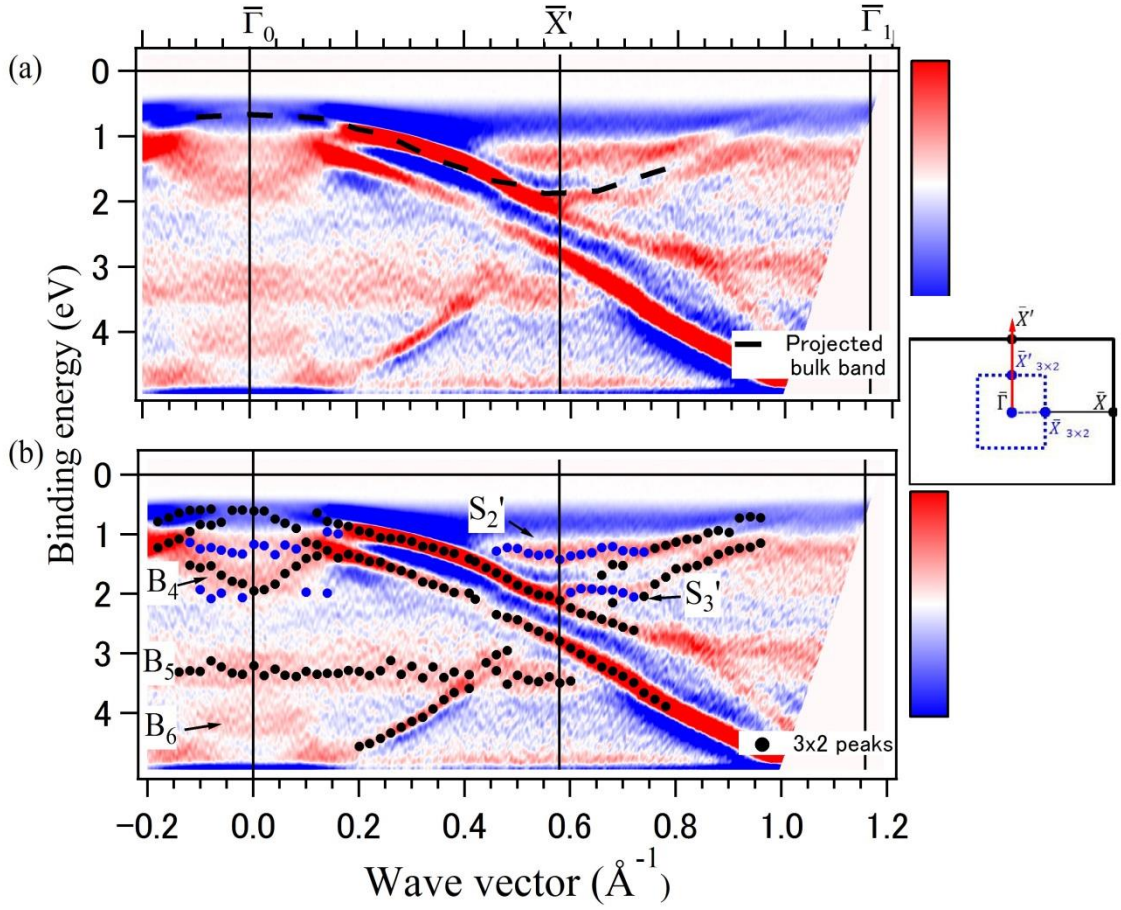

Figure 4.16. 2nd derivative intensity map of the ARPES spectra of the Si(110)3×2-Bi along the [001] direction overlaid with (a) the projected bulk band edge [54] and (b) peaks taken from EDCs. Inset: SBZ of 1×1 and 3×2 cells.

Along the $\bar{\Gamma}_0 - \bar{X}$, $[\bar{1}10]$, direction of the Si(110)1×1 SBZ, the S_2' and S_3' states are also observed in the same energy position (Fig. 4.17) as those observed in the [001] direction. The S_3' state is evidently more dispersive than in the spectra along the [001] incidence direction. S_2' is non-dispersing in both the [001] and $[\bar{1}10]$ direction, appearing almost flat, with a ~0.2 eV width. S_3' has the same width along the [001] direction, but in the $[\bar{1}10]$ direction, it has a bandwidth of around ~0.33 eV.

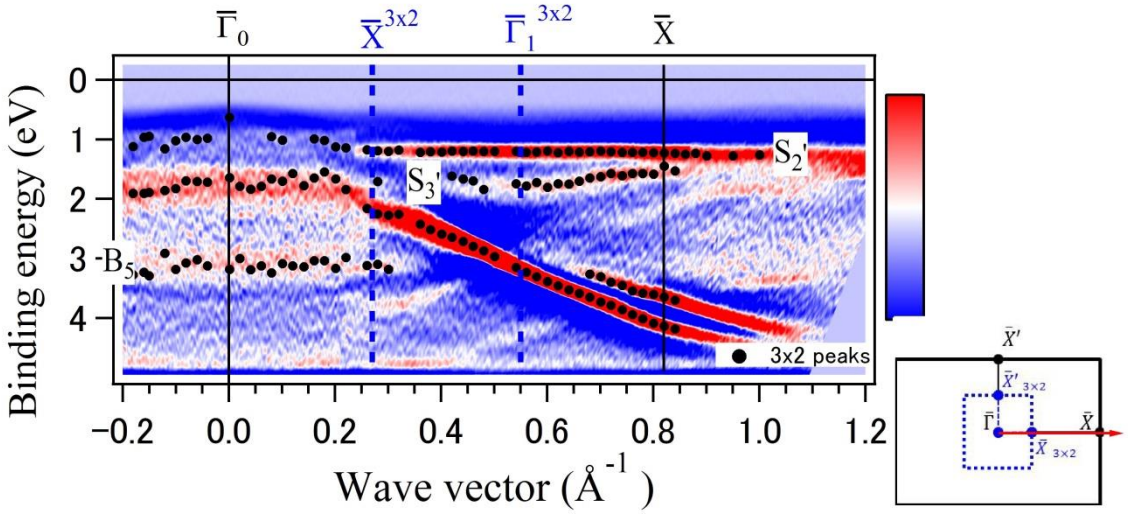

Figure 4.17. 2nd derivative intensity map of the ARPES spectra of the Si(110)3×2-Bi taken along the [$\bar{1}$10] direction. The SBZ boundaries of the 3×2 surface are indicated by the blue lines. Inset: SBZ of the 1×1 and 3×2 unit cell.

S_3' is also observed to be backfolded at the SBZ boundaries of the 3×2 unit cell. Fig. 4.18 highlights the dispersion of S_3', with guide lines to show the 3×2 SBZ boundaries.

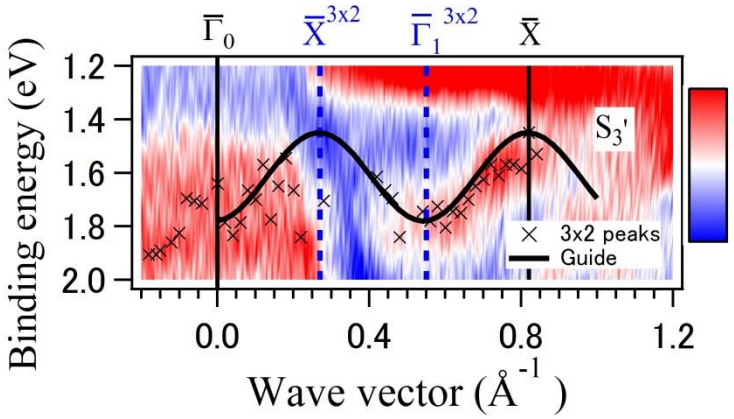

Figure 4.18. 2nd derivative intensity map of the ARPES spectra of the Si(110)3×2-Bi taken along the [$\bar{1}$10] direction zoomed in on S_3'.

This backfolding of S_3' at the boundary of the 3×2 SBZ suggests that S_3' is a 3×2 derived electronic state and it reflects the ×3 periodicity of the surface.

Fig. 4.19 shows the band structure of the Si(110)3×“4”-Bi surface along the [001] incidence direction.

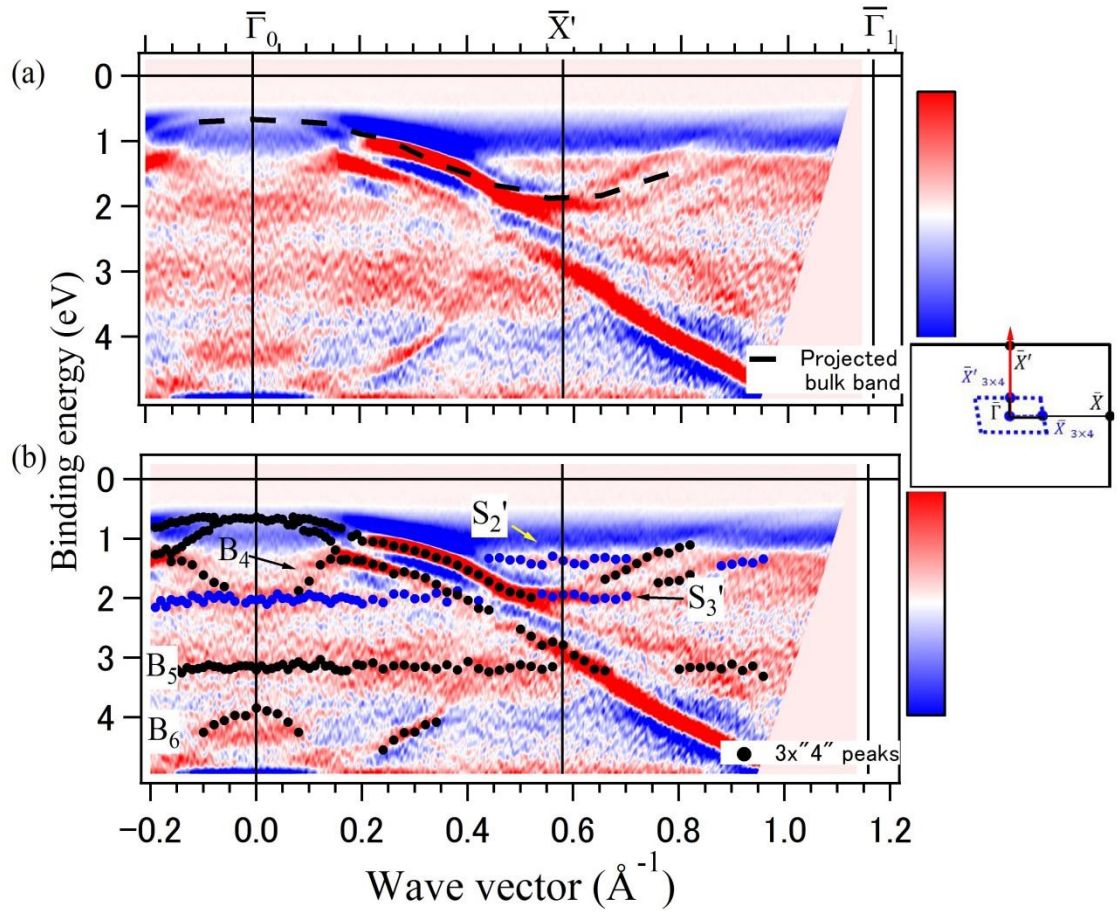

Figure 4.19. 2nd derivative intensity map of the ARPES spectra of the Si(110)3×“4”-Bi taken along the [001] direction overlaid with (a) the projected bulk band edge [54] and (b) peaks taken from the EDCs. Inset: SBZ of 1×1 and 3×“4” cells.

The S_2’ and S_3’ states of the 3×2 surface are still observed in the 3×“4” spectra, in the same energy position and has the same dispersion characteristics.

Along the $[\bar{1}10]$ direction, S_2’ and S_3’ are also observed, as shown in Fig. 4.20. Like in the 3×2-Bi surface, the S_3’ state is reflected at the 3×“4” SBZ boundary. Fig. 4.21 shows that the 3×“4”-Bi surface still has the same ×3 periodicity along the $[\bar{1}10]$ as the 3×2-Bi surface.

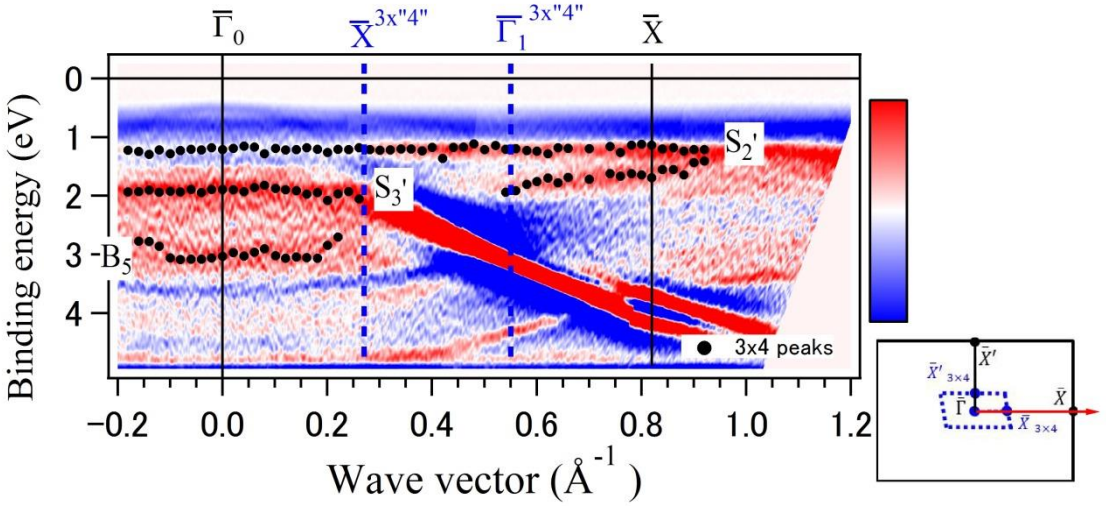

Figure 4.20. 2nd derivative intensity map of the ARPES spectra of the Si(110)3×“4”-Bi taken at the $[\bar{1}10]$ direction. The SBZ boundaries of the 3×“4” surface are indicated by the black lines. Inset SBZ of the 1×1 and 3×“4” unit cells.

The reciprocal lattice vectors $\mathbf{b}^*_{\mathbf{3\times2}}$ (eq. (32)) and $\mathbf{b}^*_{\mathbf{3\times"4"}}$ (eq. (33)) only differ by $1/4\,\mathbf{b}^*$vector in the 3×“4” surface. This, however, does not affect the ×3 periodicity along the $[\bar{1}10]$ direction, and the S_3’ state is backfolded at the boundaries of the 3×“4” SBZ.

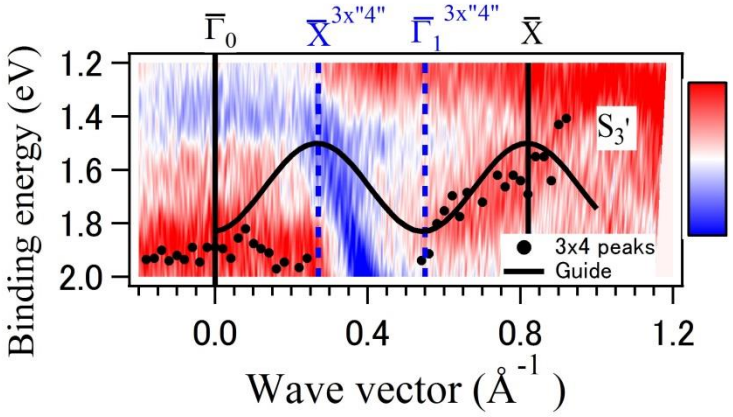

Figure 4.21. 2nd derivative intensity map of the ARPES spectra of the Si(110)3×“4” -Bi taken along the $[\bar{1}10]$ direction zoomed in on S_3’.

For the Si(110)3×“6”-Bi surface, the S_2’ and S_3’ states are once again observed in the same binding energy position and has the same dispersion characteristics. The 2nd derivative intensity map of the ARPES spectra of the 3×“6”-Bi surface taken at the

[001] incidence direction is shown Fig. 4.22. In this surface however, a third weaker electronic state is observed close to the E_F, S_1' located at ~0.2 eV.

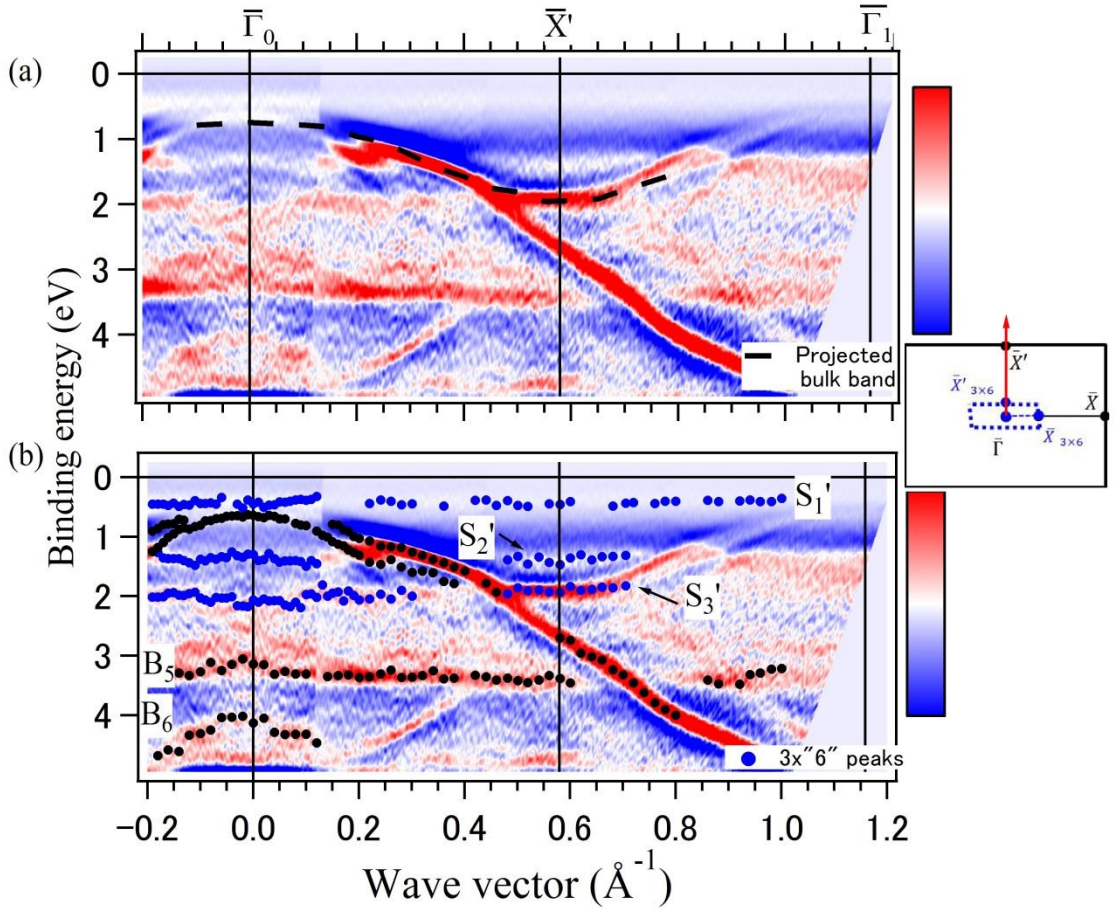

Figure 4.22. 2nd derivative intensity map of the ARPES spectra of the Si(110)3×"6"-Bi taken at the [001] direction overlaid with (a) the projected bulk band edge [54] and (b) peaks taken from the EDCs. Inset: SBZ of 1×1 and 3×"6" cells.

Fig. 4.23 compares the EDC's of the Bi/Si(110) surfaces taken from the SBZ boundaries along the (a) [001] and (b) [$\bar{1}$10] directions. The binding energy positions of these three states, S_1', S_2' and S_3', located in the bulk band gap, suggest their surface state characters. The appearance of the S_2' and S_3' on the different Bi-induced reconstructions suggests that these electronic states originate from bonding orbitals present on all these surfaces.

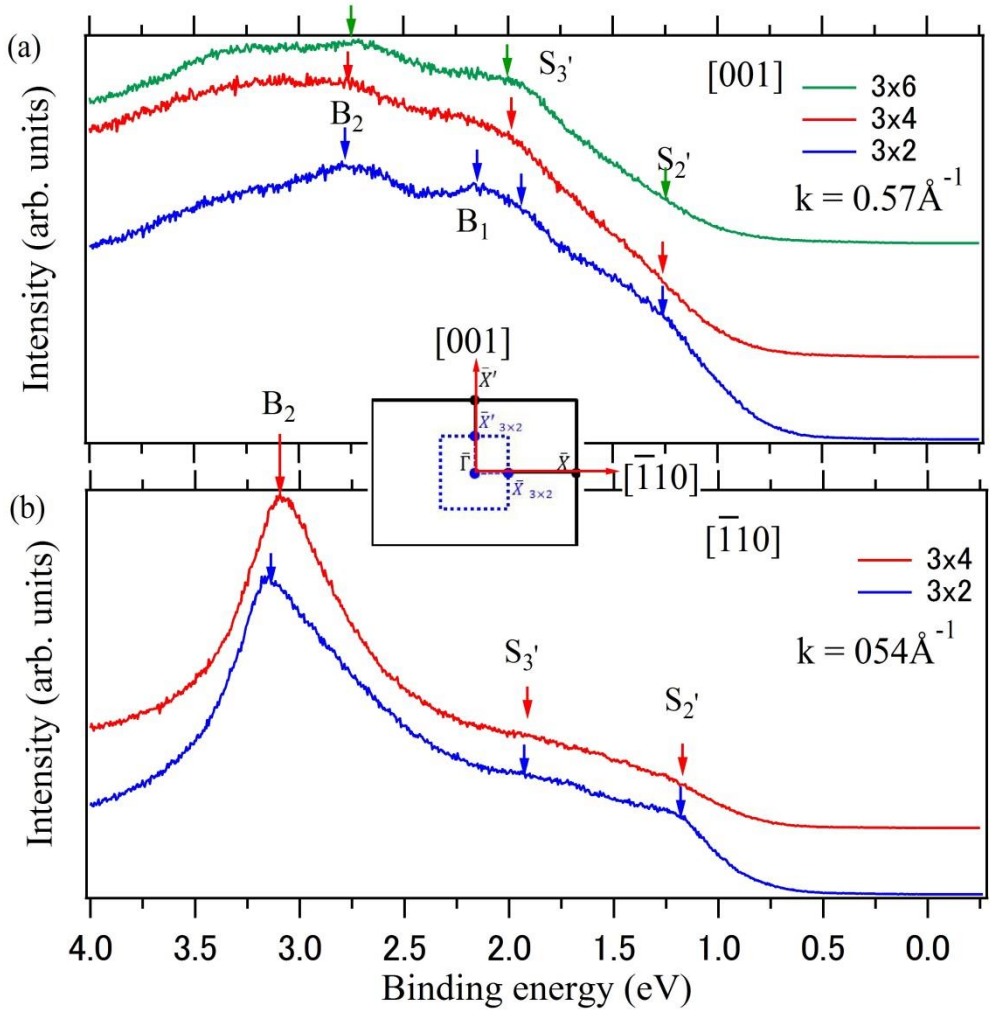

Figure 4.23. EDC of the Bi-induced reconstructions taken at the SBZ boundaries along the (a) [001] direction, $\mathbf{X'^{3\times2}}$ (k=0.57 Å^{-1}) and (b) [$\bar{1}$10] direction, $\mathbf{X^{3\times2}}$ (k=0.54 Å^{-1}). Inset: SBZ of the 1×1 and 3×2 surfaces.

States similar to the S_2' and S_3' states reported in this study were observed on the ARUPS spectra taken from the Si(110)-β 3×2-Sb, Sb_1 at 1.8 eV and Sb_2 at 2.2 eV [79]. Similar dispersion properties were observed, where along [001] the states were non-dispersing and were more dispersive along the [$\bar{1}$10] direction. Cricenti, *et al.* [79] concluded that these were surface states derived from Sb-Sb and Sb-Si bonding orbitals of the Sb trimers that were believed to be the building blocks of the 3×2 surface. It was later shown that there was no experimental evidence to support the trimer model and

that 3×2 adatom model was found to be more likely [80, 81, 82]. Similar electronic states were observed on Si(111)α√3×√3-Bi [83], one of the states, SL2 was located at ~2.0 eV. Its dispersion revealed the √3×√3 SBZ, and was assigned as a surface state derived from *p*-orbitals of the Bi adatoms and Si atoms on the surface [83]. They also observed a state similar to S_1' observed here, a very weak non-dispersing state close to E_F. It was reported that this is a defect state (DS) originating from minor structural elements remaining from the clean Si(111)7×7 surface [83, 84, 85].

To help further clarify the S_1'-S_3' bands, the electronic structure of the Si(110)1×1-Bi surface is shown in Fig. 4.24 and Fig. 4.25. At 1 ML Bi coverage, all the Si DBs on the surface is fully saturated, and DB states should no longer exist on the surface.

The 2nd derivative intensity map of the ARPES spectra of the Si(110)1×1-Bi surface taken along the [001] direction is shown in Fig. 4.24. The S_2' and S_3' states can still be observed in the same binding energy positions with the same non-dispersing character. This indicates that the S_2' and S_3' states are not surface states derived from unsaturated DBs on the Si substrate. Furthermore, the S_1' state cannot be observed in the scanned $E_B - k_{\|}$ region, this suggests that the S_1' is just a defect state like the DS state observed on metal-adsorbed Si(111) surfaces [83, 84, 85]. Furthermore, the binding energy position of this state is similar to the 16×2 surface state S_2. Thus, this S_1' state is concluded to be a defect state originating from structural elements from the 16×2 surface that still remained on the surface.

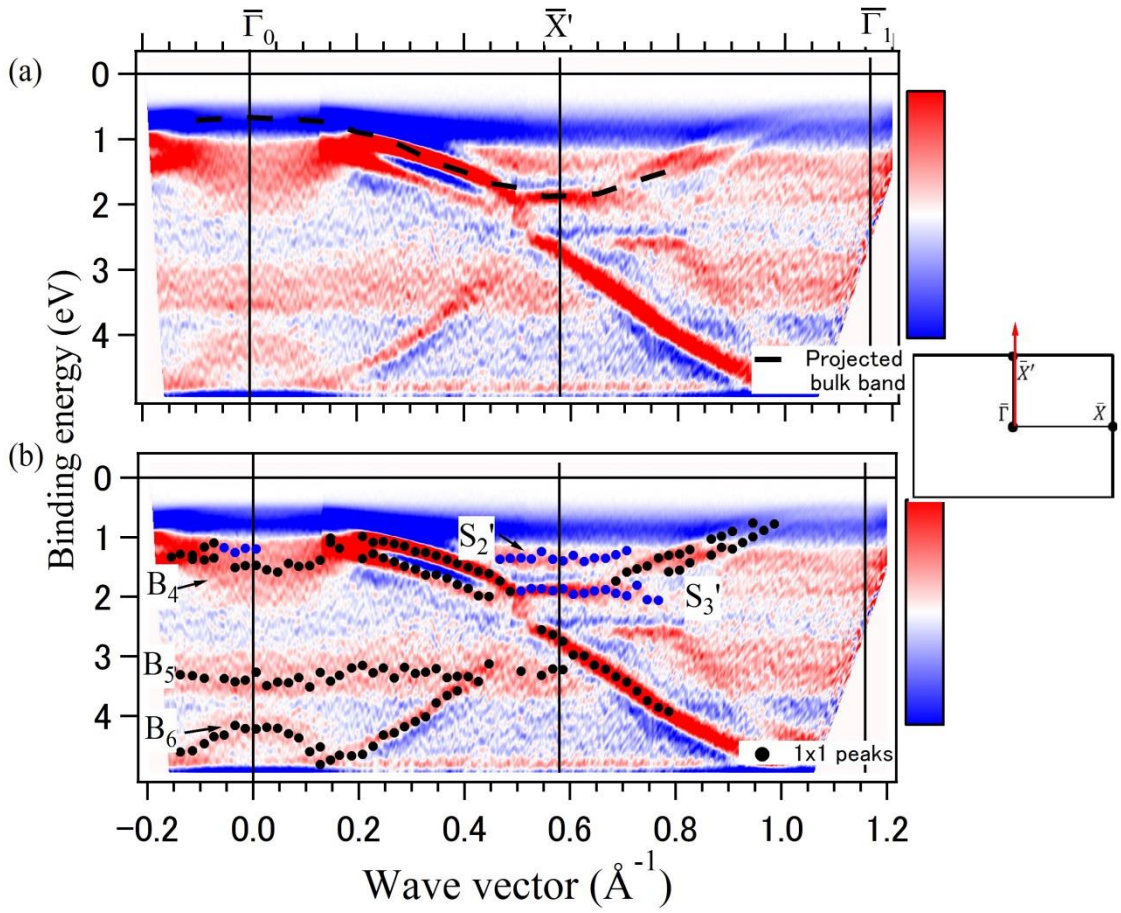

Figure 4.24. 2nd derivative intensity map of the ARPES spectra of the Si(110)1×1-Bi taken at the [001] direction overlaid with (a) the projected bulk band edge [54] and (b) peaks taken from the EDCs. Inset: SBZ of 1×1 unit cell.

In the ARPES spectra of the Si(110)1×1-Bi surface taken along the $[\bar{1}10]$ direction, as shown in Fig. 4.25, a broad non-dispersing state S_4' is observed in the binding energy region where S_2' and S_3' were observed. This S_4' is completely non-dispersing and does not show any symmetry along the SBZ boundary of the 3×2 unit cell like the S_3' state.

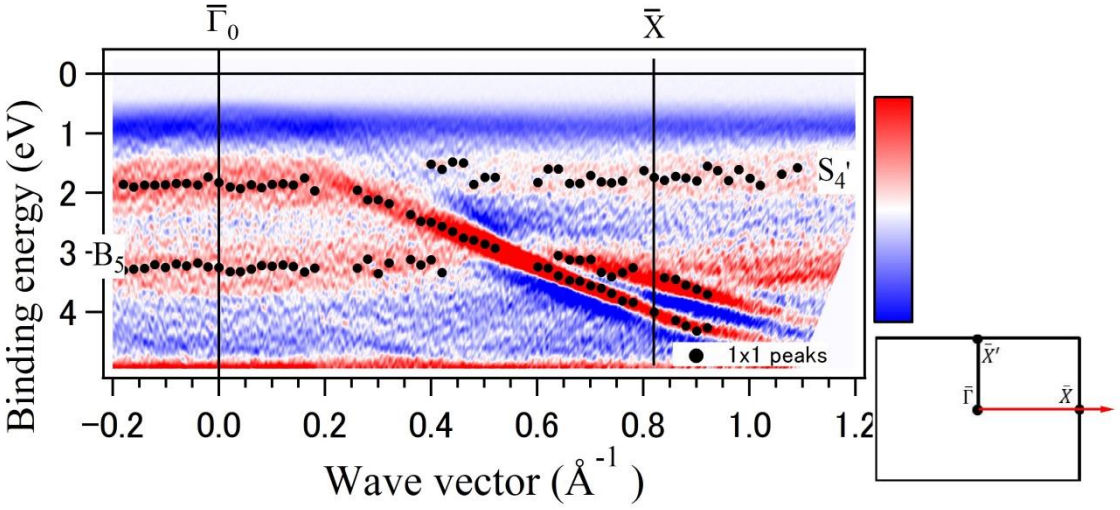

Figure 4.25. 2nd derivative intensity map of the ARPES spectra of the Si(110)1×1-Bi taken along the $[\bar{1}10]$ direction. The SBZ boundary of the 1×1 surface is indicated by the black line.

From the results of the ARPES experiments, comparisons with similar electronic states in the literature, and from DFT calculations of the band structure of the Si(110)3×2-Bi [86], it can be concluded that the S_2', S_3' and S_4' are surface states of the different Bi-induced reconstructions derived from Bi-Si backbonding. From the anisotropic dispersion of the S_3' state, it can be concluded that the overlap integral of the orbitals involved in this bonding is higher along the $[\bar{1}10]$ than in the [001] direction.

4.3.3. Structural models

From the experimental results in the previous sections, and the various experimental results available in the literature, structural models for the different Bi-induced reconstructions on the Si(110) surface are proposed here.

From their study of the Bi/Si(110) system, Oyama, *et al*. [71], proposed a Bi adatom model for the Si(110)3×2-Bi surface. In their model, shown in Fig 4.26 (a), Bi adatoms are adsorbed on the surface and saturates 3 Si dangling bonds each, forming zigzag chains aligned along the $[\bar{1}10]$ direction. Another model, based on metal trimers

on the surface, was proposed for the Si(110)3×2-Sb (1/3 ML) surface by Zotov *et al* [87] and is shown in Fig. 4.26 (b).

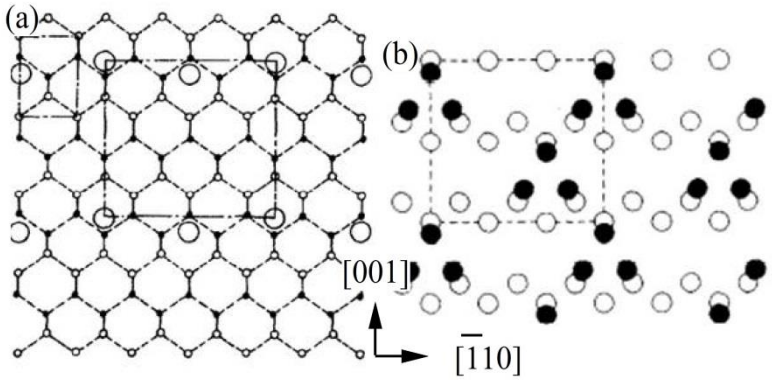

Figure 4.26 Structural models proposed for the 3x2 surface: (a) the adatom model [71], where the larger circles are Bi adatoms, and (b) the trimers model [87], where the filled circles are Sb atoms in a trimer.

However, Sb core-level photoemission [80], STM images [81], and first-principles calculations [82, 88] have shown no evidence of the metal trimers in the model proposed by Zotov *et al* [87]. Instead of trimers, the 3×2-Sb reconstruction is formed by tetrahedrons, where Sb atoms occupy the top most layer and saturates the dangling bonds of 3 Si atoms on the 2nd layer [88].

Bi 5d core-level photoemission spectra taken from the different Bi-induced surface reconstructions, as shown in Fig. 4.27, show a single component peak.

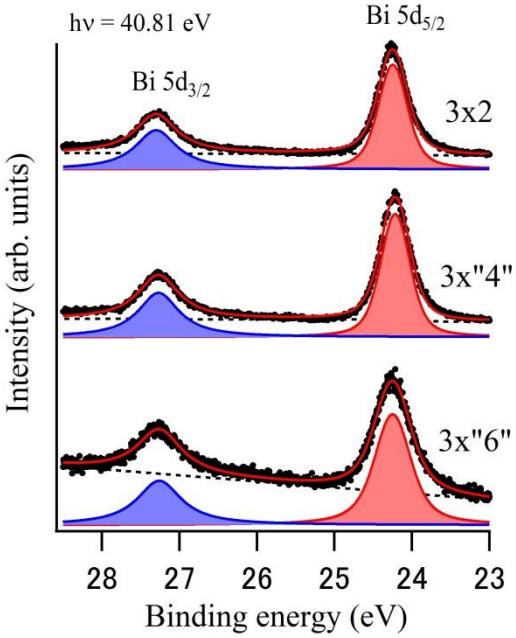

Figure 4.27. The Bi 5d photoelectron spectra of the 3×2, 3×“4” and 3×“6”-Bi surfaces (black circles), with the background (dashed line), peak fitting results (red line), and the individual peak components.

The core-level spectra were fitted using a Shirley or linear background. The Bi 5d peaks were fitted with Voigt functions using the least-square method. The parameters of the peak fittings are summarized in Table 4-2.

Table 4-2. Summary of the peak fitting parameters for the Bi 5d spectra.

	Bi $5d_{3/2}$			**Bi $5d_{5/2}$**			**Branching ratio**
	Pos.	**Lor. Width**	**Gaus. Width**	**Pos.**	**Lor. Width**	**Gaus. Width**	
3×2	27.30	0.65	0.001	24.25	0.22	0.32	1.53
3×“4”	27.27	0.64	0.001	24.22	0.19	0.34	1.58
3×“6”	27.26	0.70	0.001	24.25	0.33	0.35	1.73

The single component in the peak fitting indicates that the adsorbed Bi atoms are in a single bonding configuration and is most likely from Bi adatom-Si bonding. Below 1 ML, peak fitting of Bi 5d core levels on GaAs(110) showed three peak components, two from Bi- backbonds to surface atoms (Bi-Ga and Bi-As bonds) and a small

component (1.5%) from Bi-Bi bonds [89]. This indicates that Bi is most likely to adsorb as adatoms than as trimers on the surface.

Based on the results obtained in this study, structural models for the various Bi-adsorbed Si(110) surfaces are proposed and shown in Fig. 4.28. The model for the Si(110)3×2-Bi surface is based on the model proposed by Oyama [71].

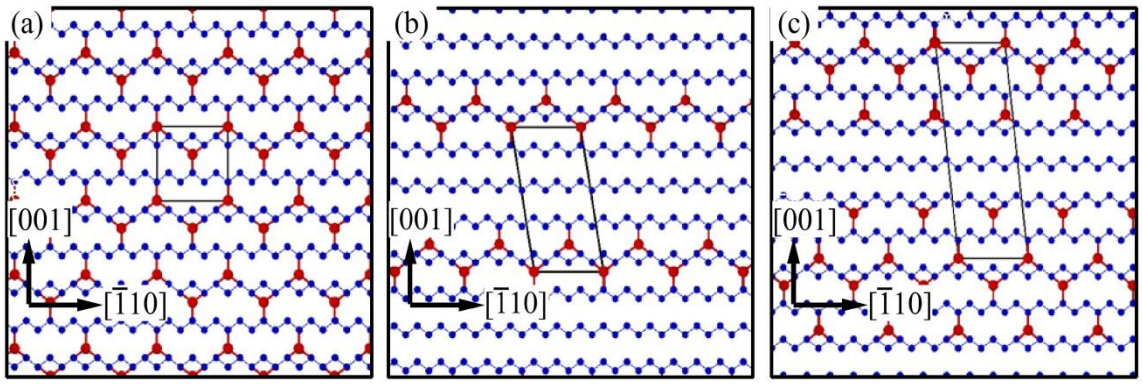

Figure 4.28. Structural models for the (a) Si(110)3×2-Bi, (b) Si(110)3×"4"-Bi and (c) Si(110)3×"6"-Bi surfaces, where the red circles are the Bi adatoms while the blue circles are the Si atoms of the substrate.

In the model for the 3×2 surface (Fig. 4.28(a)), the Bi atoms are adsorbed as adatoms and arranged to form the 3×2 unit cell. These Bi adatoms are illustrated in Fig. 4.29.

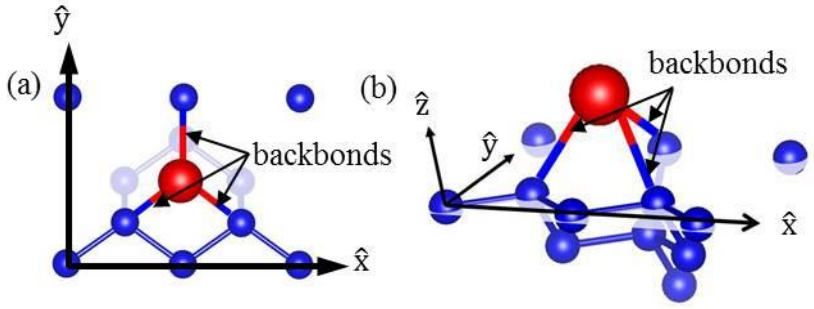

Figure 4.29. Schematic diagram of the backbonds between a Bi adatom and Si substrate atoms (a) top view and (b) 3D view, where the red spheres = Bi adatoms, and blue spheres = Si atoms.

STM images taken of the Si(110)3×2-Bi [72] and Si(110)3×2-Sb [81] surfaces showed 5 bright protrusions in the 3×2 unit cell: 4 in the corners and one in the center, as shown in Fig. 4.30 (a) and (d). These bright protrusions can be interpreted as the adatoms on the surface, and by overlaying the structural models on these STM images, (Fig. 4.30(b) and (e)), it can be seen that there is good agreement between the Bi adatom positions and the bright protrusions observed in the STM images.

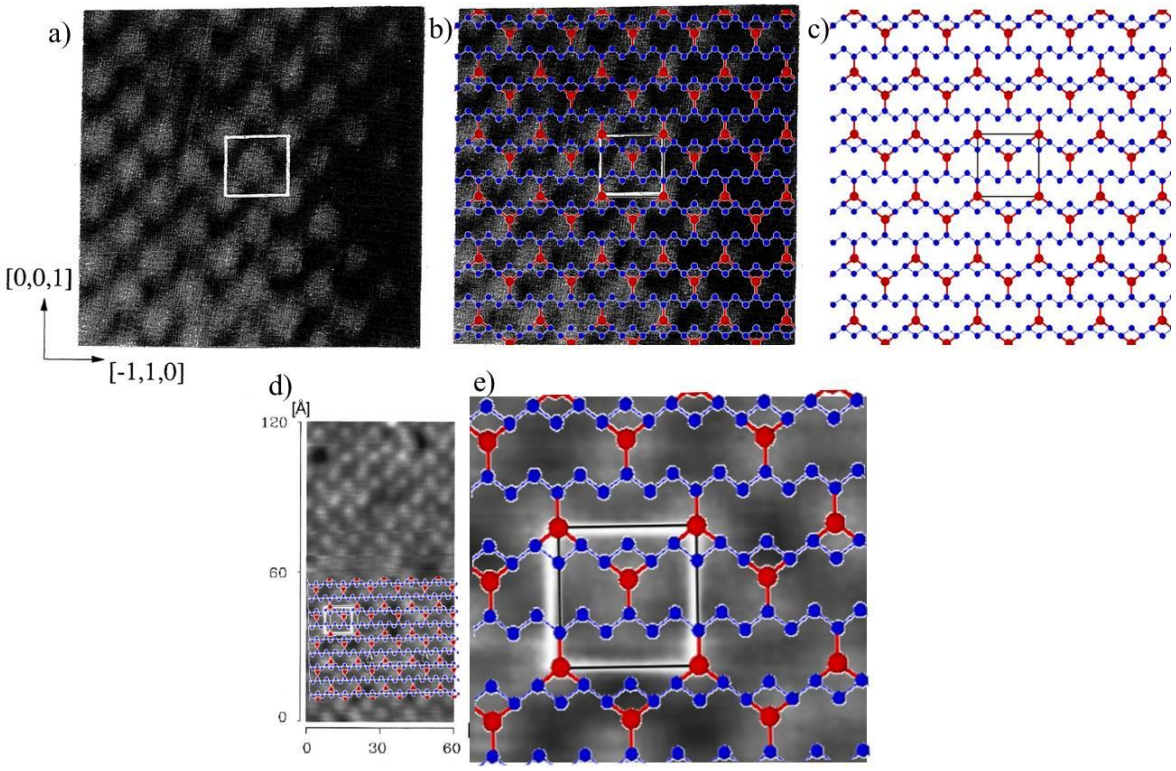

Figure 4.30 (a) STM image of the Si(110)3×2-Bi surface [72], (b) the STM image from (a) overlaid with the structural model shown in (c). (d) STM image of the Si(110)3×2-Sb [79] overlaid with the model and (e) an enlarged image.

Structural models based on the 3×2 model are also proposed for the 3×"4" and 3×"6" surfaces. For the 3×"4"-Bi surface, as shown in Fig. 4.28 (b), entire rows of zigzag Bi adatoms are removed and the remaining rows of Bi adatoms are shifted by one unit cell vector along the $[\bar{1}10]$ direction with respect to its adjacent row. In this model, adjacent Bi rows are separated by $4\mathbf{a_2}$ or 2.172 nm ($\mathbf{a_2} = 0.543\ nm$).

STM images of a similar structure (Fig. 4.31 (a)), the Si(110)α'-In shows rows of In chains separated by 2.2 nm [77], close to the distance between adatom rows in the model for the 3×"4"-Bi surface. Overlaying the model for the 3×"4" surface on this STM image, as shown in Fig. 4.31 (b), once again shows good agreement between the Bi adatom positions in the model and the bright protrusions in the STM image.

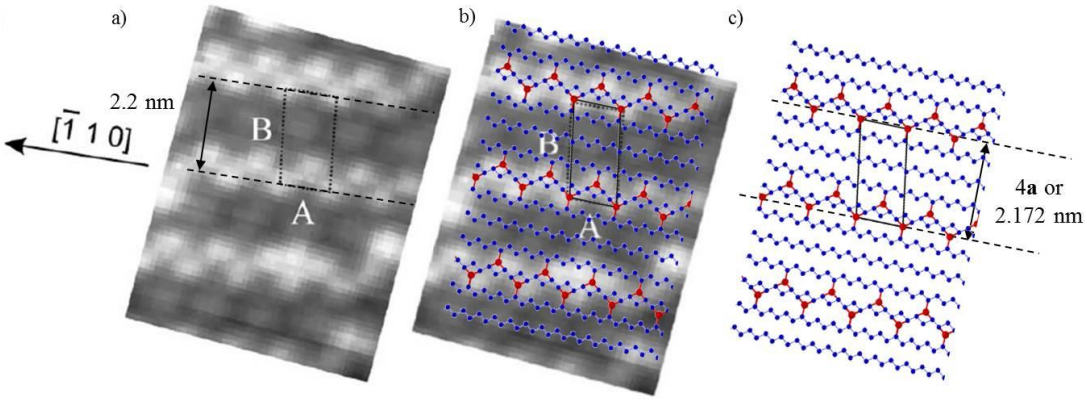

Figure 4.31. (a) STM image of Si(110) α'-In surface [77], (b) the STM image from (a) overlaid with the structural model in shown in (c).

A similar model with missing rows and shifts along the $[\bar{1}10]$ direction between adjacent Bi adatom rows is also proposed for the 3×"6" surface in Fig. 4.28(c). As this study is the first reported observation of this reconstruction, STM images is unavailable for this surface. However, the good agreement between the model and the STM images for the 3×2 and 3×"4"-Bi surfaces is a good indicator that this model for the 3×"6" can also explain the actual structure on the surface.

The models proposed in Fig. 4.28 for the different Bi-induced reconstructions also explain the anisotropic dispersion of the S_3' backbond state observed in the ARPES spectra in the previous section. As seen in Fig. 4.28, there is more overlap between the sp^3 orbitals of the Si atoms along the $[\bar{1}10]$ direction than in the [001] direction.

From these structural models, the coexistence of the sharp diffraction spots and streaks in the RHEED patterns discussed in Section 4.3.1 can be appropriately explained. These streaks in the RHEED pattern indicate strong structural correlation along the $[\bar{1}10]$ direction and poor structural correlation along the [001] direction. From the proposed structural models of the Si(110)3×"4" and Si(110)3×"6"-Bi, the Bi adatoms are arranged in lines along the $[\bar{1}10]$ direction. This can be analogous to a pseudo-one dimensional arrangement of scatterers on the surface. To get the streaks along the [001] direction observed in Fig. 4.9 (a) and 4.11 (a), a disorder has to be introduced along the [001] direction. This disorder can be achieved by introducing phase shifted unit cells on the surface. These phase shifted unit cells can be obtained by ±**a** shifts along the $[\bar{1}10]$ direction of rows of Bi adatoms. These shifts of the unit cell will result in antiphase domain boundaries on the surface. Fig. 4.32 shows a schematic diagram of a antiphase domain boundary on the Si(110)3×"4"-Bi surface.

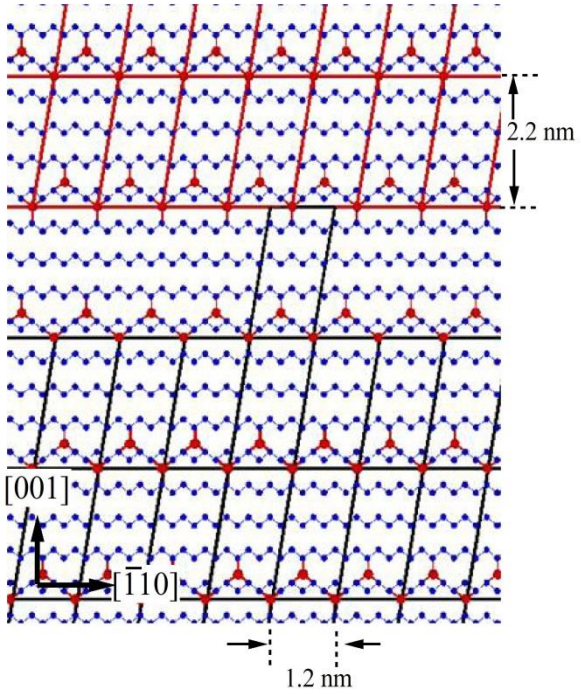

Figure 4.32. Schematic diagram of an antiphase domain boundary between two domains of the Si(110)3×"4"-Bi surface.

4.3.4. Further Discussions

Similar surface reconstructions

The structural models proposed in this study for the 3×"4" and 3×"6"-Bi surfaces can be adapted to explain other similar reconstructions on the Si(110) surface. There have already been several reports of similar diffraction patterns with a coexistence of sharp spots and elongated streaks along the [001] direction in various metal adsorbed Si(110) surfaces [32, 33, 76, 77, 90, 75]. STM images showed rows of adsorbates arranged along the $[\bar{1}10]$ direction, with varying periodicities along and between these rows [33, 77, 91, 92, 80]. For the "4×6" or $\begin{pmatrix} 3 & 0 \\ \bar{1} & 4 \end{pmatrix}$-Al [75], α' or $\begin{pmatrix} 3 & 0 \\ \bar{1} & 4 \end{pmatrix}$-In [77] and $\begin{pmatrix} 3 & 0 \\ \bar{1} & 3 \end{pmatrix}$-Sn [90] surfaces, the unit cells extracted from their respective diffraction patterns were parallelograms with one unit cell vector parallel to the ideal unit cell vector $\vec{\mathbf{a}}$ along the $[\bar{1}10]$ direction, similar to the unit cells derived for

the 3×“4” and 3×“6” surfaces in this study. Thus, the streaks in the diffraction patterns taken from these Al [75], In [77] and Sn [90] adsorbed surfaces can also be explained by the presence of antiphase domains on these surfaces. Similar LEED patterns, with similar n/3 streaks elongated along the [001] direction, were also observed for the Si(110)“6”×5-Pt [33]. However, additional weak n/2 streaks were also observed. STM images revealed a ×3 periodicity along the Pt wires ($[\bar{1}10]$ direction) and an additional ×2 periodicity along the valleys between these wires, with minimal correlation between the periodicities [33].

The Si(110)3×“4”-Bi and 3×“6”-Bi surfaces presented in this study did not show this n/2 periodicity in the RHEED patterns taken at the $[\bar{1}10]$ incidence, and thus this ×2 periodicity is not expected between the Bi adatom rows. STM images from the similar Si(110)α’-In structure showed some protrusions arranged along the $[\bar{1}10]$ direction between the rows of In adsorbates, but these exhibited a ×3 periodicity, and thus does not affect the diffraction patterns. However, from the experimental results in this thesis, no conclusions can be made about the structure between the rows of Bi adatoms in the models presented in this study. However, speculations about possible structural arrangements between these rows of Bi adatoms can be made by minimizing the unsaturated DBs left on the substrate.

In the model proposed for the Si(110)3×“4”-Bi surface in Fig. 4.28, there are still 18 Si atoms with unsaturated DBs per unit cell. To create a more energetically favorable surface, these unsaturated DBs have to be reduced or completely saturated. In Fig. 4.33 (a), the Si(110)3×“4”-Bi model proposed in the previous section is shown with the 2nd Si layer included. Models based on the reconstruction of a Si zigzag chain

between the Bi adatom rows (inside the black dashed lines in Fig. 4.33(a))) are proposed here.

Below this Si zigzag chain, there are two Si(111) planes. These two planes are shown in Fig. 4.33 (b) and (c) by temporarily removing the Si zigzag chain from the topmost layer.

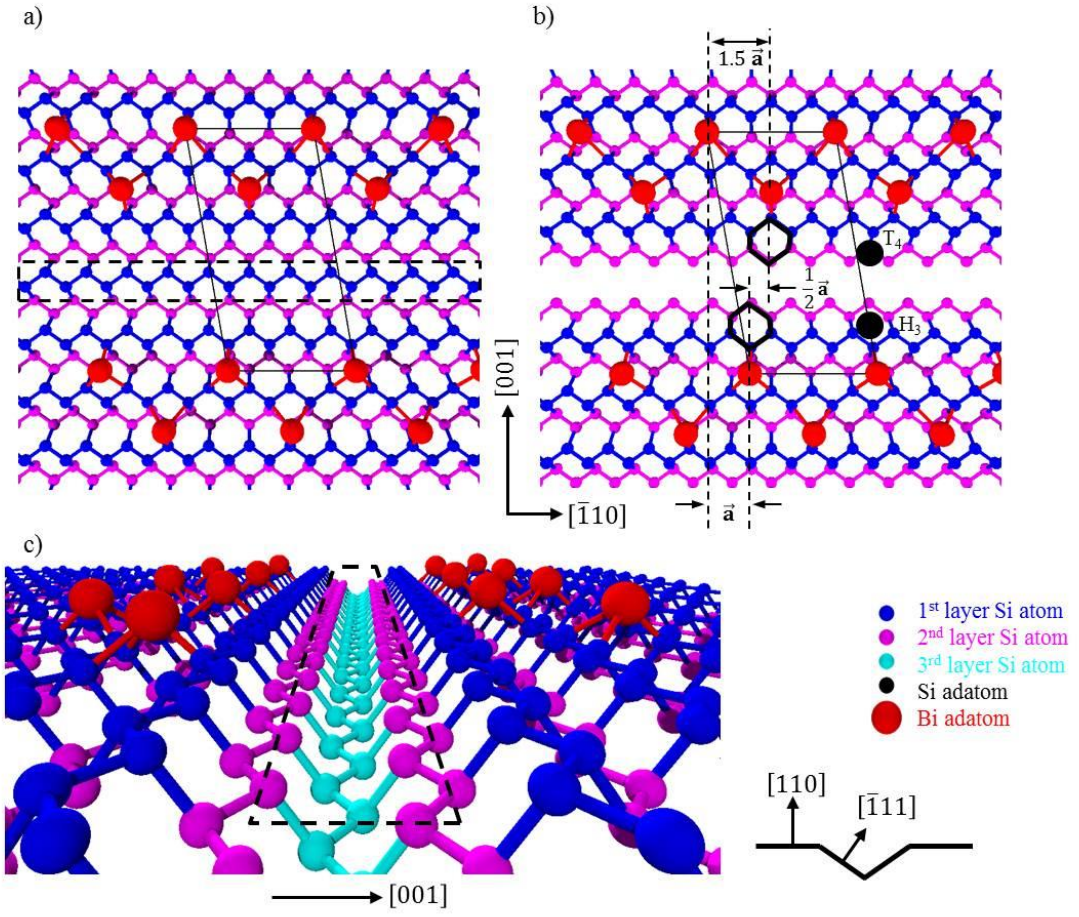

Figure 4.33 a) The Si(110)3×"4"-Bi model with the 2nd layer Si atoms shown. (b) top and (c) side view of the surface after temporarily removing the Si zigzag chain in the black dashed rectangle in (a). Inset: crystallographic directions of these sufaces.

These two Si(111) planes are out of phase with respect to each other, with a half unit cell vector $\left(\frac{1}{2}\vec{\mathbf{a}}\right)$ shift as shown in Fig. 4.33(b). The Si atoms on these two planes have one unsaturated DB each and two adsorption sites become available on these

Si(111) surfaces, the H_3 and T_4 sites, shown in Fig. 4.33(b). To saturate these DBs, the Si bonds in the zigzag chain indicated by the black dashed rectangle in Fig. 4.33 (a) are broken and these atoms rearrange to saturate as much DBs as possible. The different possible reconstructions involve the adsorption of these Si atoms on the H_3 and T_4 sites of the two Si(111) planes, as shown in the schematic in Fig. 4.34 (a). The difference in the atomic radius between Bi and Si atoms will result in small distortions in the positions of the Si atoms around these Bi adatoms, pushing Si atoms towards the zigzag chain indicated by the black dashed rectangle in Fig. 4.33 (a). The Si atoms are adsorbed on the H_3 and T_4 sites alternatingly along the $[\bar{1}10]$ direction. From this arrangement, there is a $3\vec{a}$ distance between identical H_3 or T_4 sites.

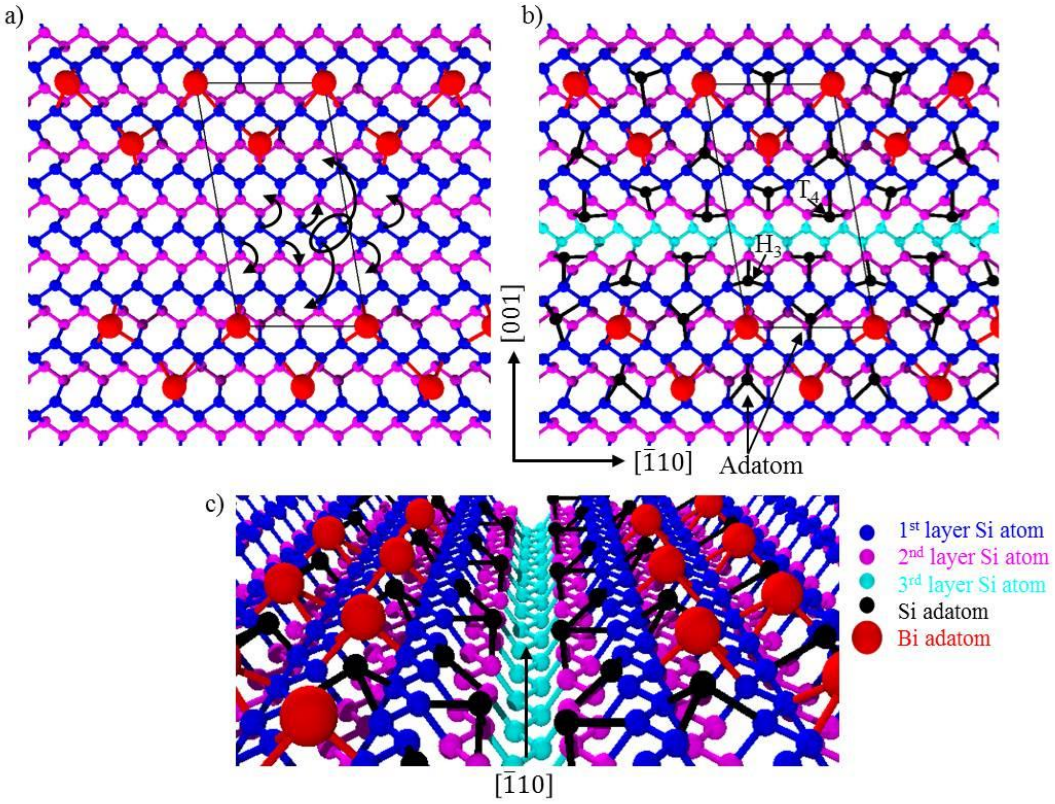

Figure 4.34 (a) The Si(110)3×"4"-Bi with a schematic of how the Si atoms reconstruct, and the H_3 model for the Si(110)3×"4"-Bi shown from (b) top and (c) side.

In this so-called H_3 model (Fig. 4.34 (b)), the Bi adatoms are adsorbed adjacent to the Si adatoms in the H_3 site. The $\frac{1}{2}\vec{\mathbf{a}}$ shift between the Si(111) planes means that the Bi adatoms closest to the reconstructed Si zigzag row are adsorbed with the same $\frac{1}{2}\vec{\mathbf{a}}$ shift. This results in the $\vec{\mathbf{a}}$ shift between adjacent Bi adatom rows.

Another possible reconstruction of this surface occurs when the Bi adatoms are adsorbed adjacent to the Si adatom in the T_4 site instead. In this T_4 model, the Bi adatoms can be adsorbed either to the right (Fig. 4.35 (a)) or left (Fig. 4.35(b)) of this T_4 Si adatom.

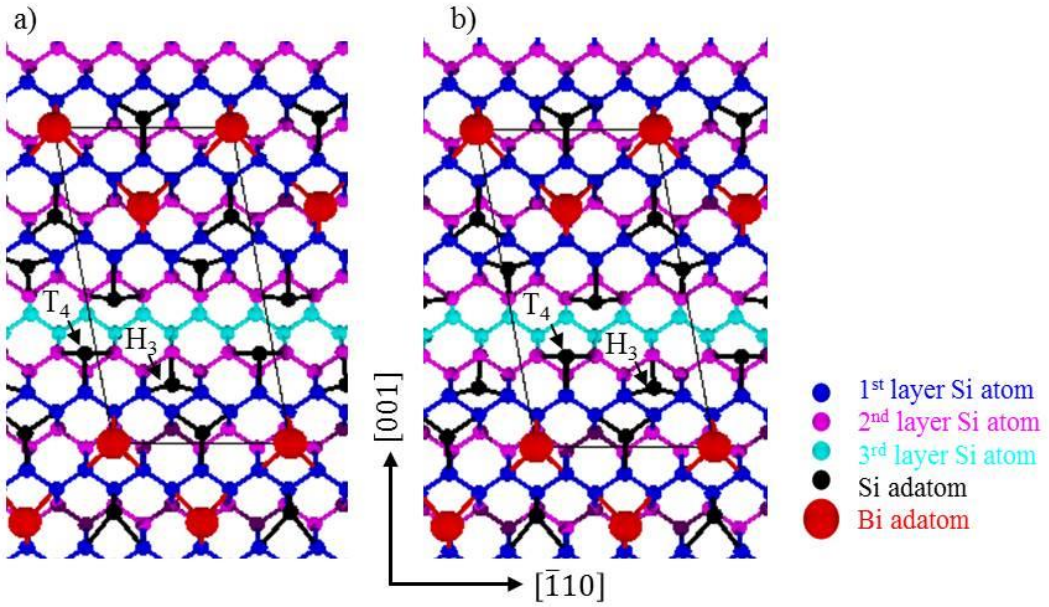

Figure 4.35. The two possible variations of the T_4 model for the Si(110) 3×"4"-Bi, where the Si adatom on the T_4 site is on the (a) left or (b) right of the Bi adatom.

Furthermore, to saturate the Si DBs between the Bi adatoms, Si adatoms are necessary between these Bi adatoms. As shown in Fig. 4.34 (a), to completely saturate the DBs along the $[\bar{1}10]$ direction between the Bi adatom rows with Si adatoms in H_3 and T_4 sites, two Si atoms from the zigzag chain must be removed (black circle in Fig.

4.34(a)). These Si atoms can then saturate the Si DBs between the Bi adatoms. These Si adatoms are the same for the H_3 and the two T_4 structural models.

In all these scenarios, the DBs per unit cell are reduced from 18 to 6, where the remaining DBs are only on the Si adatoms on the surface. In all three models, the $\frac{1}{2}\vec{\mathbf{a}}$ shift between the Si(111) planes cause the $\vec{\mathbf{a}}$ shift between the adjacent Bi adatom rows. In the original models proposed in Fig. 4.28 (b), there was no clear reason why the $\vec{\mathbf{a}}$ shift between Bi adatom rows occurs and why these surfaces were stable. By introducing this $\frac{1}{2}\vec{\mathbf{a}}$ shift through the Si(111) planes, this shift between the Bi adatom rows will occur naturally.

Furthermore, because this shift can either be $\frac{1}{2}\vec{\mathbf{a}}$ or $-\frac{1}{2}\vec{\mathbf{a}}$, these models also allow the existence of two mirror symmetric domains, as was observed in the RHEED patterns in Fig. 4.9 and Fig. 4.11.

Finally, a fourth scenario for this reconstruction can also occur when the Bi adatoms on one adatom row is adsorbed as suggested by the T_4 models, while the adjacent row is adsorbed in the H_3 configuration. This is shown in Fig. 4.36.

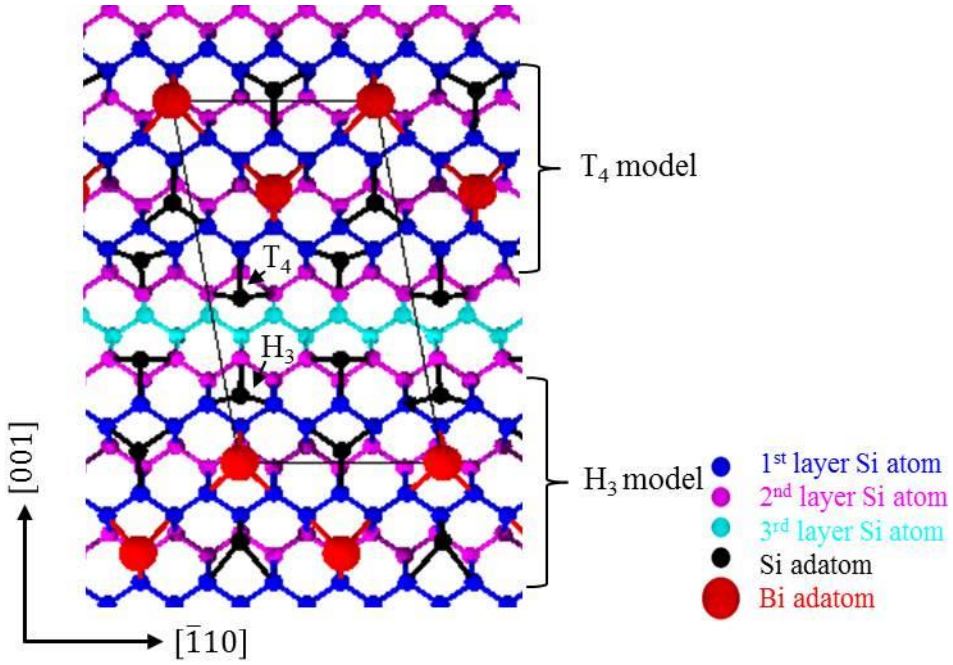

Figure 4.36. The T_4-H_3 model for the Si(110)3×"4"-Bi.

While this T_4-H_3 model can also adequately explain the periodicity of the surface and the existence of the two mirror symmetric domains, this model does not appear to be energetically possible. Between the H_3 and the T_4 structural models, there will be one that is more energetically favorable. For example, if the H_3 model is more energetically favorable, all the Bi adatoms will adsorb adjacent to the Si adatom in the H_3 site as shown in Fig. 4.33 (b).

In all these models presented, the periodicity of the structural elements between the Bi adatom rows is $3\vec{\mathbf{a}}$, and thus, does not affect the overall periodicity of the surface. This also is supported by the lack of additional periodicities observed in the RHEED patterns in Fig. 4.9 (a) and Fig. 4.11 (a). In terms of the available STM images, the bright protrusions observed between the Bi adatom rows can be derived from the unsaturated DBs of the Si adatoms on the H_3 and T_4 sites. These DB orbital lobes will be oriented perpendicular to these Si(111) planes. From these speculative models, it

cannot be conclusively determined whether these Si adatoms can form bonds along the [001] direction.

Similar structural elements can also be incorporated in the structural model for the Si(110)3×"6"-Bi surface (Fig. 4.30 (c)).

Again, it should be noted that the H_3 and T_4 models proposed here are highly speculative. However, these structural models can already be used as a basis in trying to explain the surface structures of similar metal adsorbed Si(110) surfaces, and as basis for further investigations on the exact atomic arrangements of these surfaces using techniques such as high resolution STM, LEED-IV and DFT calculations.

Bi diffusion

The structural models proposed in this thesis are based on the assumption that the deposited Bi atoms are adsorbed on the surface and bonds to the unsaturated DB's of the Si atoms and does not diffuse into the bulk Si substrate. The highly reactive surface of the ideal Si(110)1×1 surface, with one DB per Si atom, suggest that the Bi atoms are limited to the topmost surface.

First, the substrate temperatures used in these experiments are below 650°C. Above 650°C, the sticking coefficient of the deposited Bi atoms is almost zero. RHEED patterns taken after Bi deposition at these substrate temperatures show the Si(110)16×2 streaks, indicating that the surface is atomically clean, without any Bi adatoms.

Furthermore, the diffusion coefficients of Bi on Si are low in the temperature range used in this study. For temperatures below 1000°C, the diffusion coefficient is below 10^{-14} cm^2/s [93, 94]. At 1250°C (flash annealing temperature), the diffusion coefficient increases to $6.3x\times10^{-13}$ cm^2/s [94]. The samples used in this experiments were used in several experiments. However, by flash annealing and post-annealing, the

clean Si(110)16×2 surface can be recovered, even after metal adsorption. This suggests that by flash annealing the metal-adsorbed Si(110) surfaces, the metal adsorbates are desorbed instead of being diffused into the bulk. This can be seen in the Bi 5d core level spectra taken from a Si(110)1×1-Bi surface and a clean Si(110)16×2 surface (Fig. 4.37) that was obtained after flash annealing the 1×1-Bi sample.

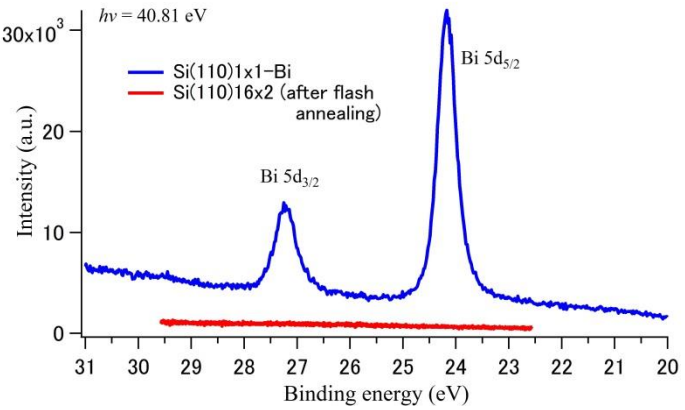

Figure 4.37. Bi 5d corelevel spectra taken from a (a)Si(110)1×1-Bi surface and (b) clean Si(110)16×2 surface after flash annealing the sample from (a).

Rashba effect

As seen in the ARPES spectra in the Section 4.3.2, Rashba-type splitting was not observed. For the low coverage Bi-adsorbed Si(110) surfaces, the 3×2, 3×"4" and 3×"6" reconstructions, three surface states were observed: the defect state S_1', and the two Bi-derived states S_2' and S_3'. However, as discussed in the previous section, these surface states are believed to originate from Bi-Si backbonds. These states have contributions from the both Si and Bi *p*-orbitals, and the effects of the spin-orbit coupling of Bi is not as strong. In Bi-adsorbed Ag(111) [95], GaAs(110) [67] and Si(111) [68] surfaces that exhibit Rashba-type spin splitting in the ARPES spectra, DFT calculations have shown that these spin-split state are derived from only from Bi orbitals. Furthermore, the low Bi coverage also reduces the contributions from the Bi atoms on these electronic states.

Furthermore, the numerical calculations and experimental observations of Rashba spin-split states on metal adsorbed semiconductor surfaces all reported metal coverages of at least 1 ML [19, 20, 67, 68]. On Si(110), Rashba spin-splitting has been reported for surfaces covered with 1 ML Pt [33], and Tl [96]. For the 1 ML Si(110)1×1-Bi surface, there is no long range order of the surface structure, and thus, any possible spin-splitting will not be resolved in the ARPES spectra.

Thus, to be able to observe Rashba split states on the Si(110) surface, the following requirements must be met:

- A well ordered 1 ML metal induced reconstruction must be possible.
- The surface states are derived from the orbitals of the metal adsorbate.

Furthermore, the use of a highly anisotropic structure, such as the Si(110) substrate, makes it possible to produce 1D Rashba spin split states as has been reported for the Pt [33] and Tl [96] adsorbed Si(110) surfaces.

4.4. Conclusions

In summary, from *in situ* RHEED observation of Bi adsorption on the Si(110) surface at various Bi coverage and substrate temperatures, the first complete phase diagram for the Bi/Si(110) system was obtained. This phase diagram summarized structural information over a wide range of Bi coverage and substrate temperatures (RT until Bi desorption temperature). Two new surface reconstructions were discovered and the unit cell vectors were derived from the diffraction patterns. The coexistence of streaks and spots on the RHEED patterns indicate strong structural correlation along one direction, and poor correlation along the orthogonal direction, suggesting a quasi one-dimensional structure. The electronic structures of the Bi-adsorbed Si(110) surfaces

were studied by ARPES and they were found to be semiconducting, with two Bi-Si backbond derived surface states. From the RHEED and ARPES data, structural models were proposed for the different Bi/Si(110) surfaces. These models can sufficiently explain both the RHEED and ARPES results. These structural models can serve as a basis for the understanding of similar reconstructions on Si(110) surfaces adsorbed with other metals.

Chapter 5. Atomic and electronic structures of In-adsorbed Si(110) Surfaces

Indium has consistently been the subject of scientific interest in the past few decades. Among the most common uses of Indium is in indium-tin-oxide (ITO) films, a transparent conducting film which has been shown to have wide applicability. More recently, it has attracted a lot of attention in amorphous-IGZO thin film transistors. In surface and interface science, indium on low index Si surfaces have been extensively studied, and used as templates for low-dimensional physics. In section 5.1, a short overview of indium on Si surfaces is presented.

In section 5.2, a short description of the experiments performed in this section is provided. This is followed by the presentation and discussion of the results in section 5.3.

Section 5.3.1 discusses the results of the experiments done on the growth of Indium on the Si(110) surface and the observed surface reconstructions.

Section 5.3.2 details the electronic structure of the surface structures discussed in section 5.3.1. From the band dispersions, as revealed by ARPES, non-dispersing surface states were observed and discussed. ARPES results also revealed the upward band bending caused by the In over-layer.

Section 5.3.3 discusses the results of the previous section in terms of possible surface structures on these reconstructions. Peak fitting of the In 4d core-level spectra revealed the presence of In-Si bonds on all In-adsorbed Si(110) surfaces studied. Additional peak components are observed on the surfaces with an indium coverage of 1 ML, and this component is attributed to In-In bonding of the adsorbates.

5.1.Introduction

5.1.1. Indium on Si surfaces

There has been a long history of interest on Indium adsorbed on low index silicon surfaces. The initial interest on In adsorbed Si surfaces was due to the numerous reconstructions observed on the surface and the desire to elucidate the surface structure. Short summaries of the properties of different In-induced superstructures on Si surfaces can be found in the anthology "*Surface Phases on Silicon*" by Lifshits, *et al.* [15].

On Si(001), there has been significant interest on In-adsorbed surfaces due to the formation of nanowire arrays on the surfaces. Well-ordered In nanowire arrays, ~0.8 nm wide, have been grown on the Si(001) surface [97]. Self-assembled metal nanowires have been of significant interest because of their potential to host 1D electron systems that could show unique transport behaviors. In-induced nanoclusters have also been investigated on Si(001) for their potential applications in nanoscale catalysts and sensors [98].

Aside from the interest in its surface structures, In-adsorbed Si(111) surfaces have been used to study novel one-dimensional and two-dimensional physics. Self-assembled In chains were grown on the Si(111) surface, and 1D charge density waves (CDW) were observed in real space by STM [16]. This Si(111)4×1-In surface had 1D metallic surface states at room temperature and the instability at lower temperatures results in the doubling of the periodicity and an opening of a band gap [16]. Chiral 1D topological edge states have also been shown on this 1D CDW system [99].

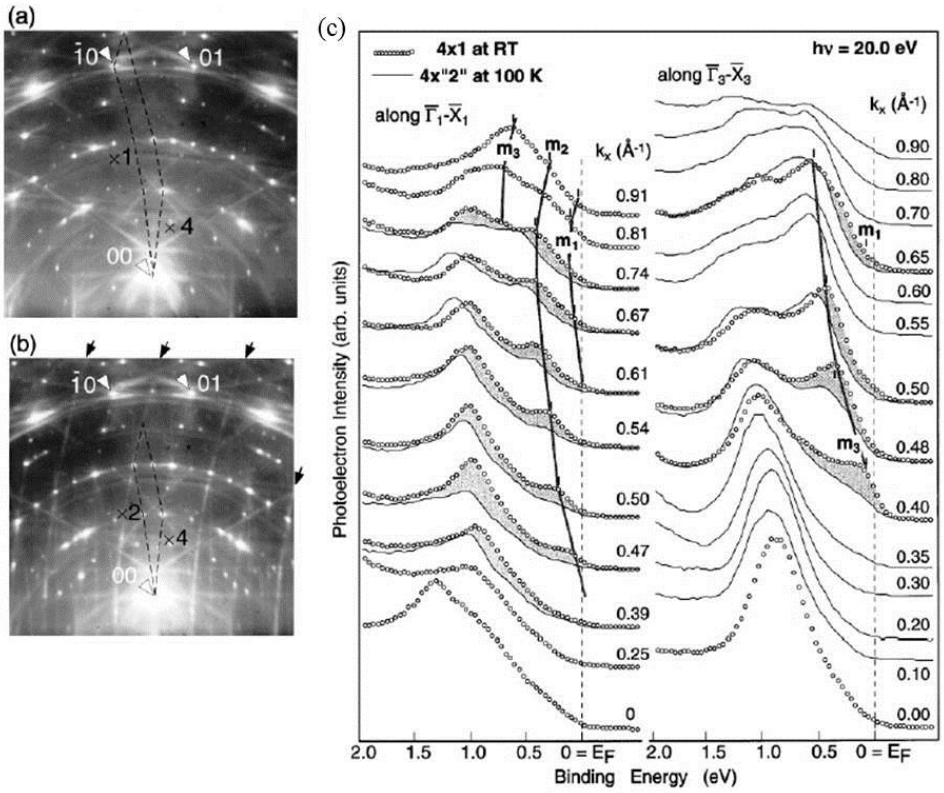

Figure 5.1. RHEED patterns of the (a) RT Si(111)4×1-In and (b) LT Si(111)4×2-In surfaces, and (c) the ARPES spectra of the two phases taken at RT and 100K. Figures are taken from [16].

For two-dimensional physics, the Si(111)√7×√3-In surface was used to demonstrate the first direct observation of the in-plane dispersion of hole subbands (HSB) by ARPES [17]. This started a series of theoretical and experimental studies about hole subbands in both Si(111) [100, 101] and Si(001) [102] surfaces. By tuning the metal adsorbate species and the surface reconstruction on the surface, an upward band bending in the space-charge layer can be formed. By forming an appropriate upward band bending, the electronic states are quantized in the surface-normal direction and have free electron-like parabolic dispersions in the in-plane direction.

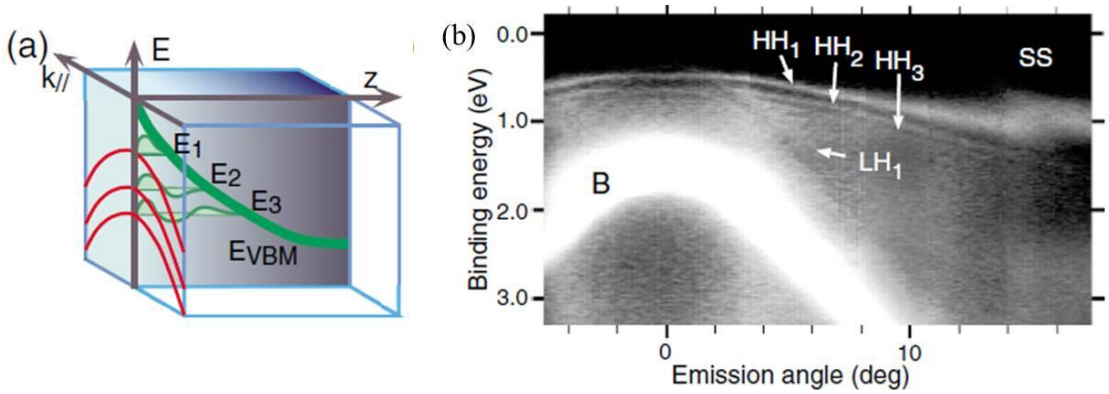

Figure 5.2. (a) Schematic diagram of hole subbands in a p-channel inversion layer and (b) ARPES spectra of the Si(111)√7×√3-In surface taken from [17].

5.1.2. Indium on the Si(110) surface

The interest on the Si(110) surface as a possible FET p-channel material has made it necessary to understand the properties of the inversion layer of the Si(110) surface. It has been shown that this inversion layer can be realized by using metal layers on the Si surface as electrodes, and the quantized HSB structures were experimentally observed [17, 100, 101, 102, 103]

Group III metals In [17] and Ga [100], and group IV Pb [102, 103], have been used as metal layers on Si surfaces to produce these HSB structures. In chapter 4, the surface and electronic structures of Bi-adsorbed Si(110) surfaces were reported and HSB structures were not observed. This was expected from the group V Bi layers on the surface. To investigate the inversion layer of the Si(110) surface, an acceptor type metal layer must be deposited on the surface.

There already has been some preliminary reports about the surface and electronic structures of the Pb-adsorbed Si(110) surfaces [104, 105, 106] and from the ARPES data, HSB structures could not clearly be observed [59, 105].

For In-adsorbed Si(110) surfaces, on the other hand, only structural studies have been done and several surface reconstructions have been reported [77, 107]. No results

about the electronic structures of these surfaces have been reported. Thus, in this thesis, the electronic structures of In-adsorbed Si(110) surfaces are investigated.

An early LEED study of the growth of In on Si(110) revealed the formation of three reconstructions, the so-called α or 3×4, β or $\begin{pmatrix} 4 & 3 \\ -2 & 2 \end{pmatrix}$, and γ or $\begin{pmatrix} 6 & 4 \\ -3 & 2 \end{pmatrix}$ surfaces [107]. A more recent RHEED study of the In/Si(110) system by Ichikawa, *et al.* [77], also observed three reconstructions, but two of these were different from the previous LEED study. They reported the observation of an α' or $\begin{pmatrix} 3 & 0 \\ -1 & 4 \end{pmatrix}$ structure with almost similar growth conditions (metal coverage and substrate temperature) as the α structure, and the γ' or $\begin{pmatrix} 3 & -2 \\ -2 & 4 \end{pmatrix}$ structure with a similar In coverage as the γ structure. They also confirmed the existence of the β structure, but reported different growth conditions. The α' structure, reported by Ichikawa, *et al.* [77], has the same unit cell vectors as the 3×"4" surface described in the previous chapter and will be referred to as the 3×"4" from this point on in this thesis. The β structure has similar unit cell vectors as the Si(110)"7×2"-Pb [104], and from this point on referred to as the 7×2 structure in this thesis. The growth conditions of the different reconstructions reported in these two studies are summarized in Fig. 5.3.

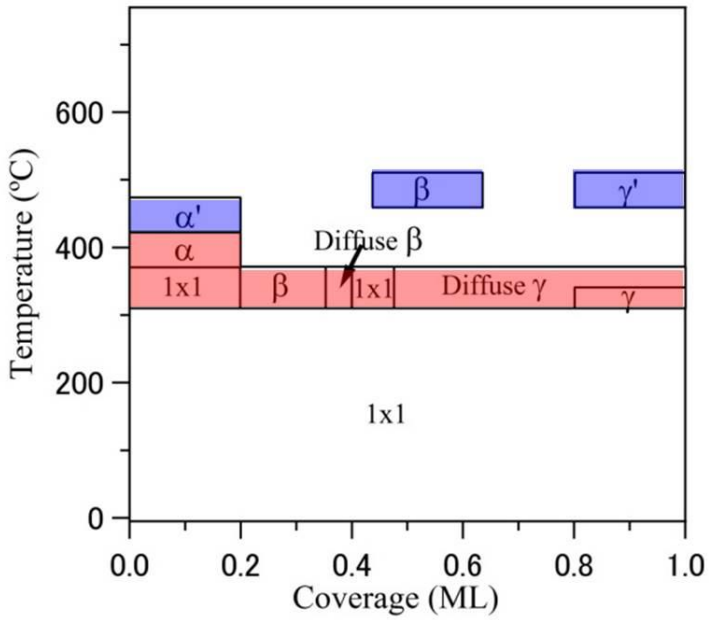

Figure 5.3. Phase diagram of the In/Si(110) system summarized from ref. [77], shown in blue, and [107], shown in red.

It should be noted, however, that despite the sharp RHEED patterns obtained by Ichikawa, *et al*., on the different In-adsorbed Si(110) surfaces, their STM images of the surface showed a poorly ordered surface, where domains with the periodicities of the α' structure and β structure coexist on the surface [77].

Aside from the surface structures reported in these studies, no other experimental results have been reported about the In/Si(110) surfaces.

This chapter attempts to clarify the conflicting reports about the phase diagram of the In/Si(110) system. To do this, the growth of In on the Si(110) surface was observed *in situ.* using RHEED at various In coverage and substrate temperatures. These surfaces were investigated using ARPES to reveal the band structures

5.2. Experimental procedures

The growth of In on Si(110) surfaces were studied by *in-situ* RHEED experiments. The clean Si(110)16×2 surfaces were prepared following the procedure

described in section 3.2. The samples were first flash annealed several times at 1250°C, followed by an annealing step at ~600°C. The clean Si(110)16×2 surface was confirmed by observing the RHEED patterns.

Indium was evaporated from a Knudsen cell and deposited on the Si(110)16×2 surface at various In coverages and substrate temperatures. The indium deposition rate was calibrated using the known 7×7-√3×√3 transition on the In/Si(111) system [15]. The substrate temperature was controlled using the annealing current. The current was calibrated with the temperature measured by an infrared pyrometer and an IR thermographic camera.

In the ARPES measurements, monochromatized light from a He discharge lamp (He I α, $h\nu$ = 21.21 eV) were used to access the bands close to the Fermi level. For In core-level photoelectron measurements, He II α ($h\nu$ = 40.81 eV) was used. All photoelectron experiments were done in ambient room temperature.

5.3. Results and discussion

5.3.1. In growth on Si(110) and surface reconstructions on Si(110)

The results of *in situ* RHEED experiments of In adsorbed on the Si(110) surface at various In coverage and substrate temperatures are summarized in the phase diagram in Fig. 5.4.

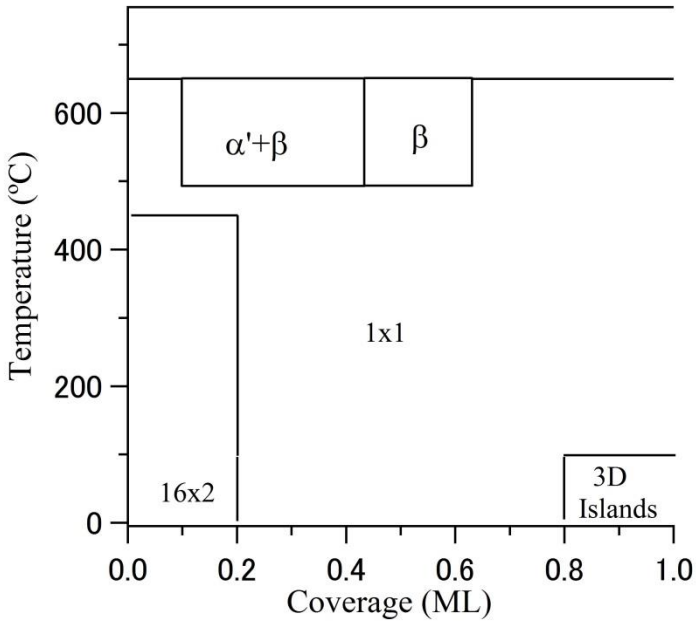

Figure 5.4. Phase diagram of In deposited on Si(110) at various In coverage and substrate temperatures from the RHEED results of this study.

At room temperature deposition, *in situ* RHEED observations showed the 16×2 streaks slowly disappearing until only the fundamental 1×1 spots remain. Upon further In deposition, at > 0.8 ML, the appearance of three-dimensional transmission spots begins. Further In deposition reveals no new surface structures after these 3D spots appear.

Annealing the substrate during deposition showed the formation of two-dimensional reconstructions on the surface. In this study however, the α, γ and γ' surfaces reported in ref. [77] and [107] could not be observed in the metal coverage and temperature formation ranges they reported. The metal coverage and substrate temperatures required for the formation of these surfaces are too narrow, and only Si 1×1 diffraction patterns were observed, even when the reported growth conditions (summarized in Fig. 5.3) of these surfaces were achieved.

At a substrate temperature of 300°C, the diffraction patterns only revealed the gradual disappearance of the 16×2 streaks until only the fundamental Si(110)1×1 streaks remain. Fig. 5.5 shows the diffraction patterns of Si(110)1×1-In after deposition of 1 ML of In at 300°C.

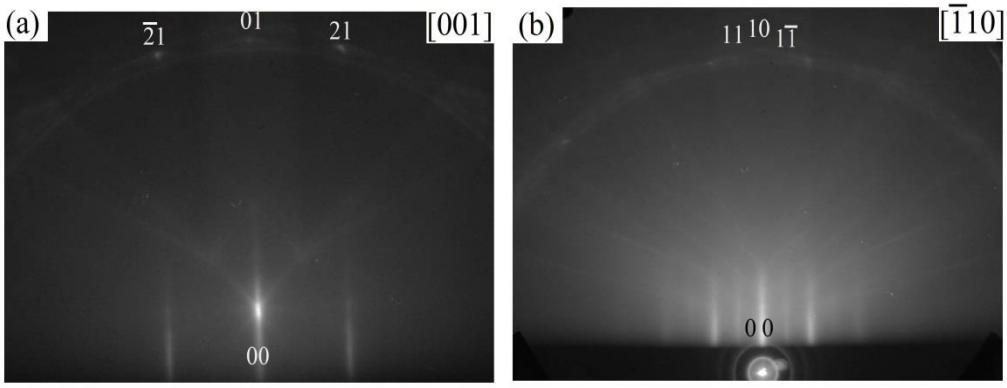

Figure 5.5. RHEED patterns of the Si(110)1×1-In surface taken at the (a) [001] and (b) [$\bar{1}$10] incidence directions.

At substrate temperatures above 500°C, *in situ* RHEED observation reveals the coexistence of the diffraction patterns of the 3×"4" (α') and 7×2 (β) structure, as shown in Fig. 5.6. In Fig. 5.6 (b), guidelines are overlaid to show the 7×2 streaks (black dashed lines), and 3×"4" (yellow dashed lines) streaks. Along the [$\bar{1}$10] incidence direction, 3×"4" streaks can be seen in the zeroth Laue zone (Fig. 5.6 (d)), while weak 7×2 streaks can also be seen in Fig. 5.6 (c).

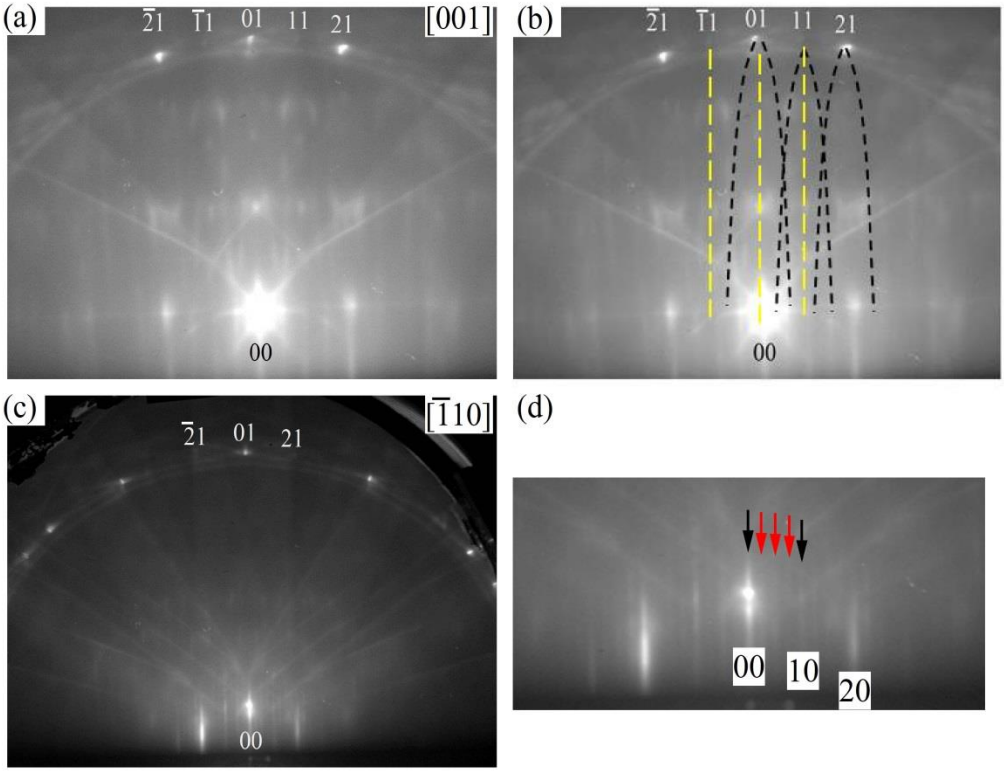

Figure 5.6 RHEED pattern taken from the 7×2+3×"4" -In surface (a) taken along the [001] incidence direction, (b) same RHEED pattern overlaid with black dashed lines for the 7×2 streaks and yellow dashed lines for the 3×"4" streaks, (c) along the [$\bar{1}$10] incidence direction, and (d) zoomed into the zeroth Laue zone of the diffraction pattern in (c).

Upon further deposition of In, the intensities of the 3×"4" features on the diffraction pattern fade until only the 7×2 remains on the diffraction pattern. Fig. 5.7 shows the diffraction patterns of the Si(110)7×2-In surface after deposition at a substrate temperature of 500°C. A double domain streak pattern similar to the 16×2 streaks are observed in the RHEED patterns.

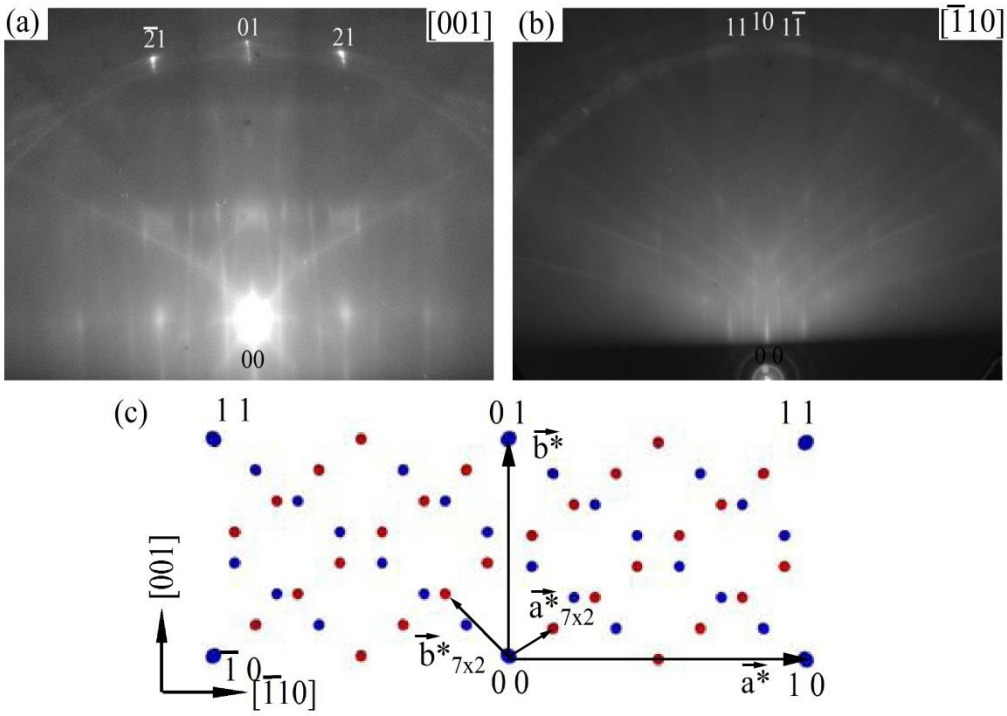

Figure 5.7. RHEED patterns of the Si(110)7×2-In surface taken at the (a) [001] and (b) [$\bar{1}$10] incidence directions, and (c) its corresponding reciprocal lattice, with the unit cells of the double domain structure.

From the analysis of the diffraction patterns in Fig. 5.7 (a) and Fig. 5.7 (b), the reciprocal lattice vectors of the 7×2-In surface can be given by,

$$\mathbf{a}^*_{\mathbf{7x2}} = \frac{1}{7}\mathbf{a}^* + \frac{1}{7}\mathbf{b}^* \text{ and } \mathbf{b}^*_{\mathbf{7x2}} = -\frac{3}{14}\mathbf{a}^* + \frac{2}{7}\mathbf{b}^* \qquad (41)$$

and the real space unit cell vectors are,

$$\mathbf{a}_{\mathbf{7x2}} = 4\mathbf{a} + 3\mathbf{b} \text{ and } \mathbf{b}_{\mathbf{7x2}} = -2\mathbf{a} + 2\mathbf{b} \qquad (42).$$

Sakama, *et al*. [107], suggested that the growth mode of the 7×2-In surface is highly dependent on the dangling bonds on the edges of the terraces of the 16×2 surface and this results in the unit cell vectors that lie parallel to the 16×2 vector **b**.

This surface has also been observed on the Pb- [104] and Sn- [90, 92] adsorbed Si(110) surfaces, however, there is still no clear structural models available.

5.3.2. Electronic structure of In induced superstructures

Fig. 5.8 shows the ARPES spectra obtained from the Si(110)7×2-In surface. The states B_1-B_6 reported in the previous chapters are also observed in this In/Si(110) surface. In the bulk band gap, two non-dispersing states are observed, I_3 at 1.1 eV and I_4 at 1.8 eV.

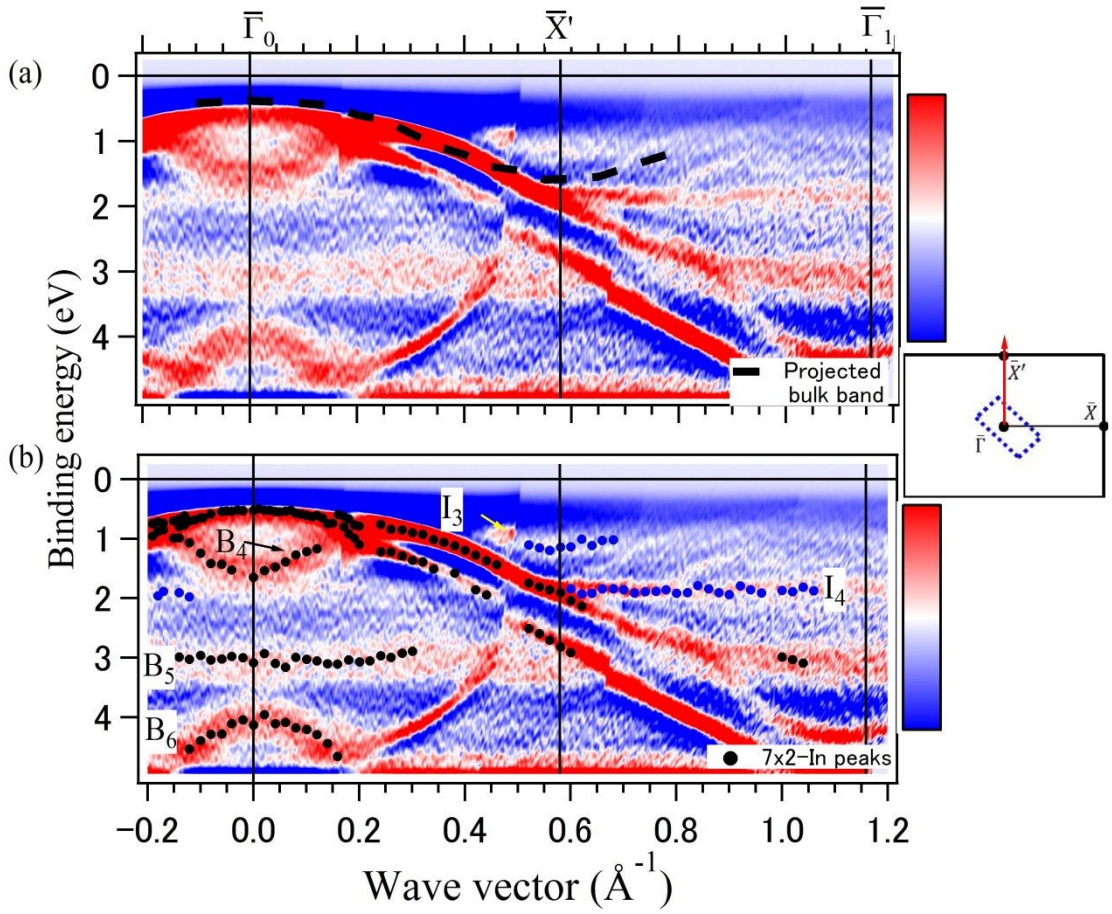

Figure 5.8. 2nd derivative intensity map of the ARPES spectra of the Si(110)7×2-In taken along the [001] direction with (a) the projected bulk band edge taken from [54] and (b) peak positions obtained from EDCs. Inset: SBZ of the 1×1 and 7×2 cells.

The position and dispersion characteristics of these states are close to the S_2' and S_3' states observed on Bi/Si(110) surfaces. In chapter 4, these surface states were thoroughly investigated and identified as Bi-Si backbond orbitals for Bi adatoms saturating three Si dangling bonds. The presence of such an electronic state suggests

that the In adatoms occupy the same adsorption site as the Bi-adsorbed surfaces, where In adatoms bonds with three Si atoms. As such, no metallic indium states were observed in the ARPES spectra.

On the 1 ML Si(110)1×1-In surface, ARPES experiments reveal four spectral features that can be observed in the bulk band gap (Fig. 5.9). These non-dispersing states are: I_1 at 0.50 eV, I_2 at 0.89 eV, I_3 at 1.25 eV and I_4 at 1.80 eV.

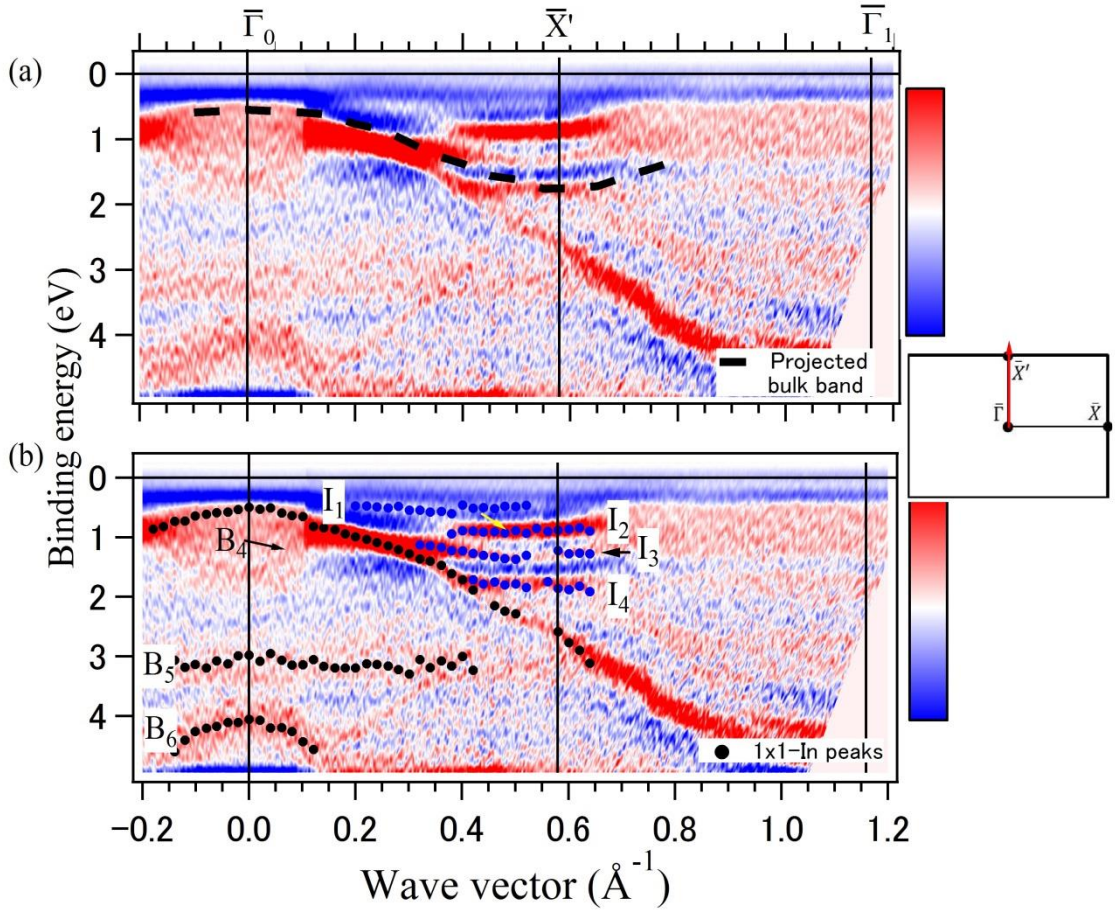

Figure 5.9 2nd derivative intensity map of the ARPES spectra of the Si(110)1×1-In along the [001] direction with (a) the projected bulk band edge taken from [54] and (b) peak positions obtained from EDCs. Inset: SBZ of the 1×1 cell.

Aside from the four surface states, a very weak non-dispersing state, I_0, close to the E_F (~0.1 eV) was also observed over a wide $k_{\parallel}$ range in Fig. 5.9 (b). Fig. 5.10 shows a closer look at the five states observed on the surface. At $k_{\parallel} = 0.45\text{Å}^{-1}$, the EDC in

Fig. 5.10 (b) shows that only the I_2 and I_4 states are observable in the raw ARPES spectra. I_1, I_3 and I_5 only became visible in the intensity map of the 2nd derivatives of the spectra.

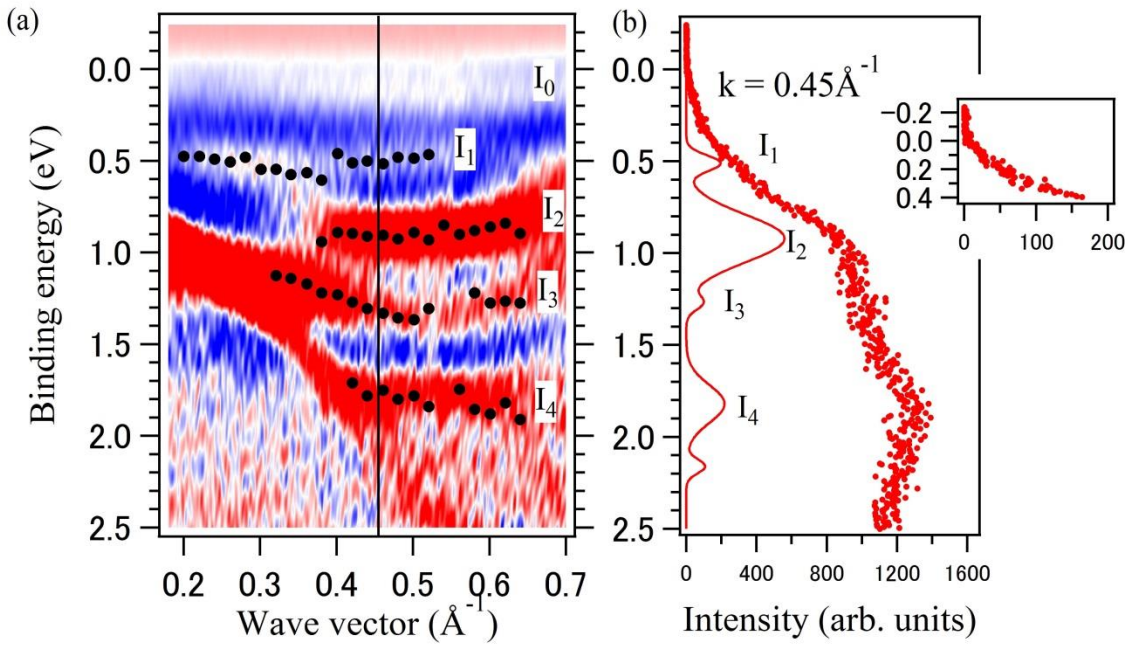

Figure 5.10. (a)A close up look at the ARPES spectra in the *E-k* region of the states observed in Fig. 5.8, (b) the raw spectra and the peak fitting components of the EDC taken at $k_{\parallel} = 0.45\text{Å}^{-1}$. Inset: closer look at I_0

In the ARPES measurements done in this study, I_0 was not clearly resolved and it cannot be observed whether I_0 crosses the Fermi level or is non-dispersing just right below E_F. This Si(110)1×1-In surface cannot be clearly identified as a metallic or semiconducting surface with a really small band gap based solely on the ARPES data.

A similar electronic state was observed at 1.5 eV below the E_F for the Si(111)√3×√3-In and was assigned as In-Si backbonds [108, 109]. A similar interpretation can be made for the I_3 peak observed in this study. States similar to I_1, I_2 and I_3 were also observed on the Si(111)4×1-In surface [108]. Aside from these

additional surface states, the 4×1-In was also reported to be more metallic, and that the surface states can be attributed to metallic bonds on the In overlayer and to In-Si covalent bonding [108, 110].

The EDCs of the 7×2-In and 1×1-In surfaces taken at the $\bar{\Gamma}$ point at $k_{\parallel} = 0$ and at $k_{\parallel} = 0.60\text{Å}^{-1}$ are compared in Fig. 5.11 (a) and (b). For the EDCs taken at the $\bar{\Gamma}$ point (Fig. 5.11 (a)), the VBM of the 1×1 surface is shifted closer to $E_{F.}$

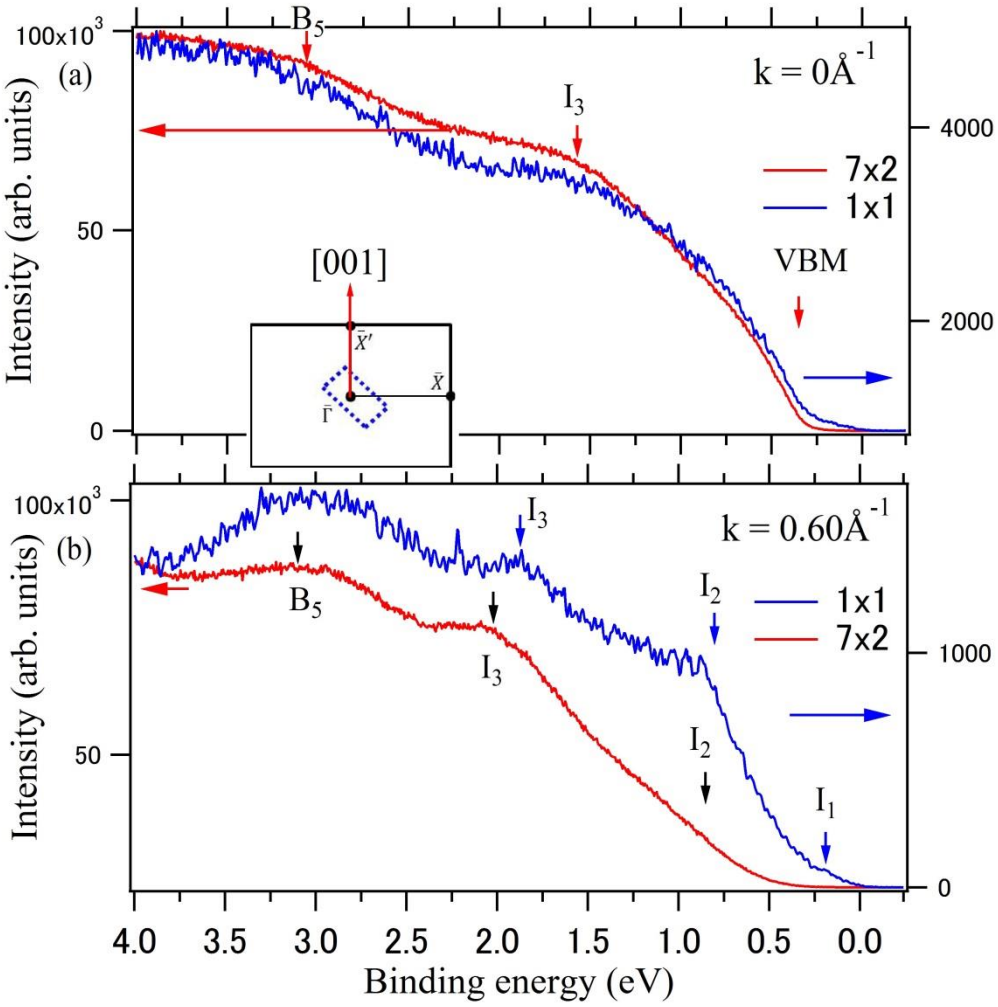

Figure 5.11. Comparisons of the EDCs of the Si(110)1×1-In and Si(110)7×2-In surfaces taken at (a) the $\bar{\Gamma}$ point at $k_{\parallel} = 0$ and (b) $k_{\parallel} = 0.60\text{Å}^{-1}$. Inset: SBZ of the 1×1 and 7×2-In surfaces.

This is indicative of upward band bending due to the In overlayer. This band bending can also be observed in the shift of I_3 towards E_F in Fig. 5.10 (b).

A closer look at the valence band maximum (VBM) of the 7×2- and 1×1-In surfaces further reveals this band bending. The energy of the VBM at the **Γ**-point ,V_0, of the Si(110)16×2, Si(110)7×2-In and Si(110)1×1-In surfaces are compared in Fig. 5.12 (a-c). Measured from the Fermi level, V_0 are located at 0.68 eV, 0.52 eV and 0.49 eV for the Si(110)16×2, Si(110)7×2-In and Si(110)1×1-In surfaces respectively, giving shifts of ~0.15 eV and ~0.2 eV for these surfaces, as summarized in Table 5-1.

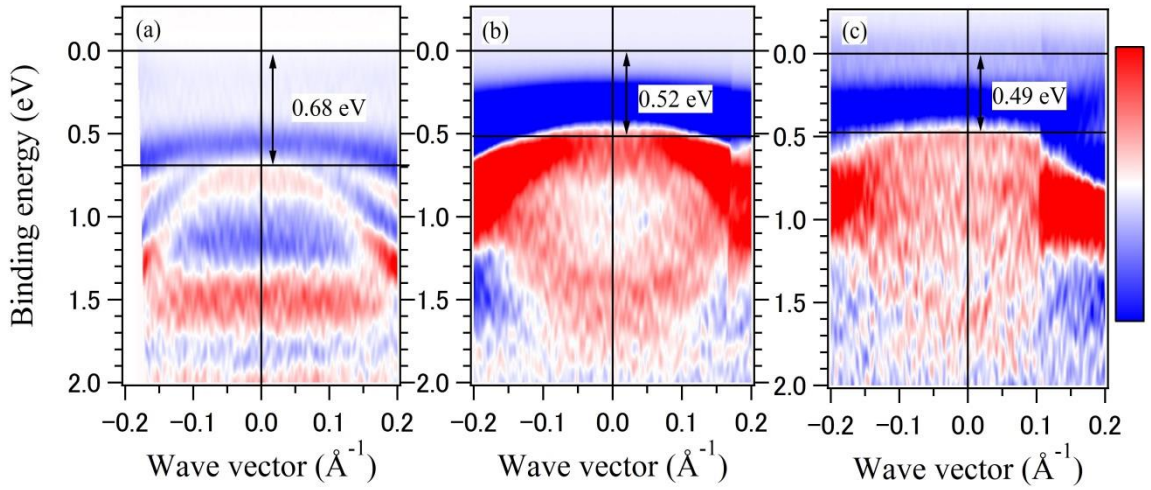

Figure 5.12. The ARPES spectra around the **Γ**-point along the [001] direction of the (a) Si(110)16×2, (b) Si(110)7×2-In and (c) Si(110)1×1-In surfaces and the energy position of the valence band maximum (V_0) relative to the Fermi level.

Table 5-1 compares the shifts in V_0 of the various Bi- and In-adsorbed surfaces investigated in this study with reported values of metal-adsorbed Si surfaces with hole-subband structures as observed by ARPES. The shifts in the Bi-adsorbed surfaces are almost negligible and subband structures are not expected to be formed. Upward band bending can be induced when the adsorbed metal on the surface is an acceptor-type and electron occupation of surface states occurs. For the In-adsorbed Si(110) surfaces, it was

observed that V_0 shifts towards the Fermi level, but the band bending is still not large enough, and hole subbands were not observed in the ARPES spectra.

Table 5-1. Comparison of the shifts in V_0 of the samples in this thesis (red) with reported surfaces with hole-subband structures observed by ARPES (black).

Surface	E_{VBM} shift (eV)
Si(110)3×2-, 3×4-, 3×6-Bi	~0.03
Si(110)1×1-Bi	0.07
Si(110)7×2-In	0.16
Si(111)3√3×3√3-PbGa [100]	0.18
Si(110)1×1-In	0.19
Si(001)2×1-Pb [102]	0.30
Si(110)-Pb [59]	0.30
Si(111)6.3×6.3-Ga [100]	0.31
Si(111)√7×√3-In [103]	0.34
Si(111)√3×√3 SIC –Pb [103]	0.59

5.3.3. Structural models

Figure 5.13 shows the In 4d core-level spectr taken from the two In-adsorbed Si(110) surfaces (7×2 and 1×1) reported in the previous sections. The spectra of 1ML of In with RHEED patterns showing 3D transmission spots (3D islands) are included as comparison. The spectra are fitted with a Doniac-Sunjic (DS) line shape convoluted with a Gaussian function to describe experimental resolution and thermal broadening [108, 111]. In the peak fitting procedure, the spin-orbit splitting was fixed at 0.88 eV, and the branching ratio was held in the range 1.4-1.6 eV.

The best fitting results for the In 4d spectra are shown in Fig. 5.13. All the In 4d spectra were deconvoluted into spin-split doublets of the DS-line shape. For the spectra taken from the 3D In islands on Si(110) (hereby referred to as In/Si(110)), two sets of spin-split DS line shapes were obtained, component B and S1. The B component was also observed on the 1×1-In surface (Enlarged view in Fig. 5.13(b)), while the S1

component is present on all three In-adsorbed surfaces. The curve fitting parameters for the best fittings are summarized in Table 5.2.

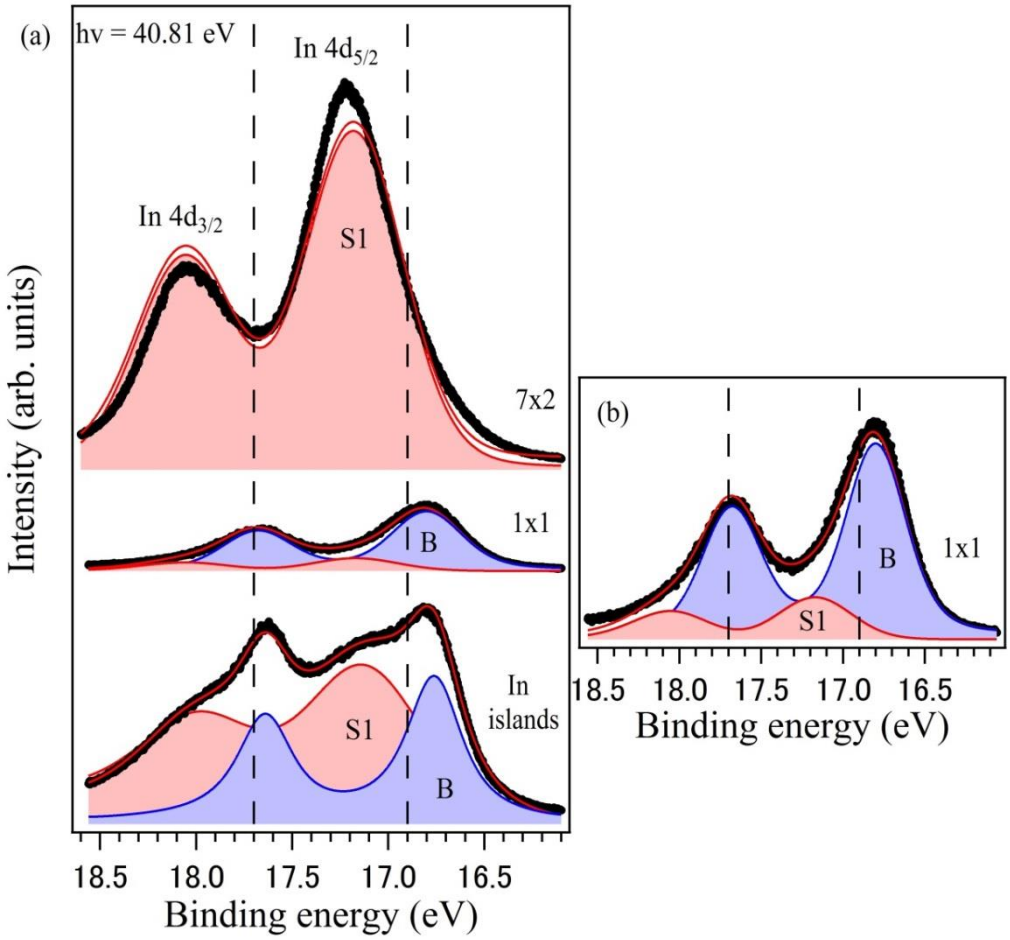

Figure 5.13. In 4d core-level spectra of the Si(110)7×2-In, Si(110)1×1-In and 3D In islands on Si(110) deposited at RT. Black dashed line indicates bulk In core-level peaks taken from ref. [112].

Table 5-2. Curve-fitting parameters for the components S1 and B used to fit In 4d photoemission spectra for the In-adsorbed Si(110) surfaces.

Surface	Component	Pos. (eV)	Gaus. Wid.	Lor. Wid.	Asym.	Splitting	Branching ratio
7x2	S1	17.18	0.56	0.08	0.00	0.88	1.6
1x1	S1	17.17	0.51	0.03	0.00	0.88	1.5
	B	16.80	0.33	0.19	0.00	0.88	1.5
In islands	S1	17.12	0.49	0.38	0.03	0.88	1.6
	B	16.76	0.12	0.30	0.03	0.88	1.4

Both the In/Si(110) and Si(110)1×1-In surfaces have an In coverage of 1 ML, the only difference being that the In/Si(110) was prepared at RT deposition. At 1 ML, there are the same number of metal adsorbates on the surface as the Si(110) areal density (9.6×10^{14} cm^{-2}). On the ideal Si(110)1×1 surface, each Si atom on the surface has one unsaturated dangling bond (DB). Thus, at an indium coverage of 1ML, two possible scenarios can occur. First, metal adatoms can occupy the sites of the (110) plane with a diamond structure, forming the same (110) zigzag chains oriented along the $[\bar{1}10]$ direction [67, 90]. This has been shown to be the energetically favorable structure for Si(110)1×1-Sb [88]. Fig. 5.14(b) shows the model proposed by Yamamoto [90] for the Si(110)1×1-Sn, where ideal Si(110)-like Sn zigzag chains are formed by 1ML of Sn. In this scenario, the metal adatom will form bonds with one Si atom, and two other metal adatoms, thus forming the zigzag chains.

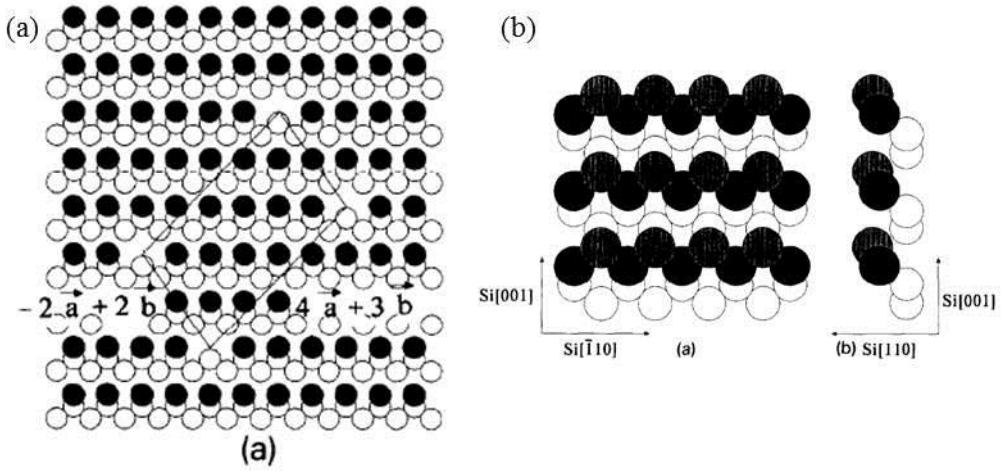

Figure 5.14. Structural models proposed by ref. [90] for the (a) Si(110)7×2-Sn and (b) Si(110)1×1-Sn, where the white circles are Si substrate atoms and black circles are Sn adatoms.

Another possible scenario is the formation of 3D structures where the structures can have metal adatoms saturating more than one Si DB. In the case of the In/Si(110)

surface, the room temperature deposition means that the In adatoms were adsorbed on the reconstructed 16×2 surface. The 16×2 surface is rough, with pentagon-shaped protrusions on a series of alternating up- and down- terraces.

This suggests that the B component in the peak fitting of the In 4d spectra are bulk-like In-In bonds, while the S1 component is from In-Si bonds.

In a similar In-adsorbed Si(111) surface, In 4d core-level spectra taken from the Si(111)√3×√3-In showed that two spin-split components were deconvoluted from the spectra [108]. The major component in their spectra was attributed to covalent In-Si bonding, while they suggested that the 2nd component, with higher binding energy is derived from In adatoms adsorbed on defect sites on the Si(111) such as on edge steps on the surface. Based on their proposed structural model the main peak fitting component is derived from In adatoms in the √3×√3 structure on the T_4 adsorption site of Si(111), where In adatoms are covalently bonded to 3 Si atoms, similar to the expected adsorption site of metal adatoms on the Si(110) surface.

As seen in the peak fitting results in table 5-2, the asymmetry parameters of both the 7×2- and 1×1-In surfaces are almost zero. Metallic core level spectrum produces asymmetric line shapes tailing towards the higher binding energy side [111]. This asymmetry is described by the asymmetry parameter, α, where it is generally accepted that $\alpha > 0.1$ indicates a metallic peak. This suggests that both the 7×2- and 1×1-In surfaces are semiconducting. For the 7×2-In surface, this agrees well with the ARPES spectra in Fig. 5.9, where no spectral features are observed crossing into the Fermi level. For the 1×1-In surface however, the asymmetry parameter indicates a semiconducting surface, but some ambiguity remain in the spectra feature (I_0 in Fig. 5.10) close to the

Fermi level. Further experiments will be necessary to confirm the semiconducting nature of the 1×1-In surface.

The experimental data collected in this study is not enough to propose a complete structural model for the Si(110)7×2-In surface. However, results from ARPES and core-level spectroscopy suggest that the In adatoms are covalently bonded to the Si atoms on the substrate. On the Si(110)1×1-In surface, the In adatoms are most likely to be adsorbed on ideal Si(110) sites and form zigzag In chains on the surface.

5.3.4. Further Discussions

Band bending

As seen in the ARPES spectra in Fig. 5.8 for the Si(110)7×2-In and Fig. 5.9 for the Si(110)1×1-In surfaces, quantized HSB structures were not observed. This is due to the small upward band bending in the space charge layers of these surfaces. The HSBs are formed when the mean free path is longer than the width of the confining potential well, in this case, the space charge layer [8, 17].

The space charge layer formed on the surface will depend on the type (charge character) and density of the surface states formed [8]. Schematic diagrams of different kinds of space charge layers on n- and p- type semiconductors are shown in Fig. 5.15. Acceptor type surface states (negatively charged if occupied) on an n-type semiconductor results in the modification of the band structure, where net neutrality requires a positive space charge layer formed by a strong band bending towards E_F [9]. This results in a depletion layer, where the density of the majority carriers (electrons in the case of n-type wafers) near the surface is lower than the bulk carrier density.

Higher densities of these acceptor surface states can result in stronger upward band bending, where the concentration of the minority carriers becomes higher than the majority carriers. This inversion layer is shown in Fig. 5.15 (a).

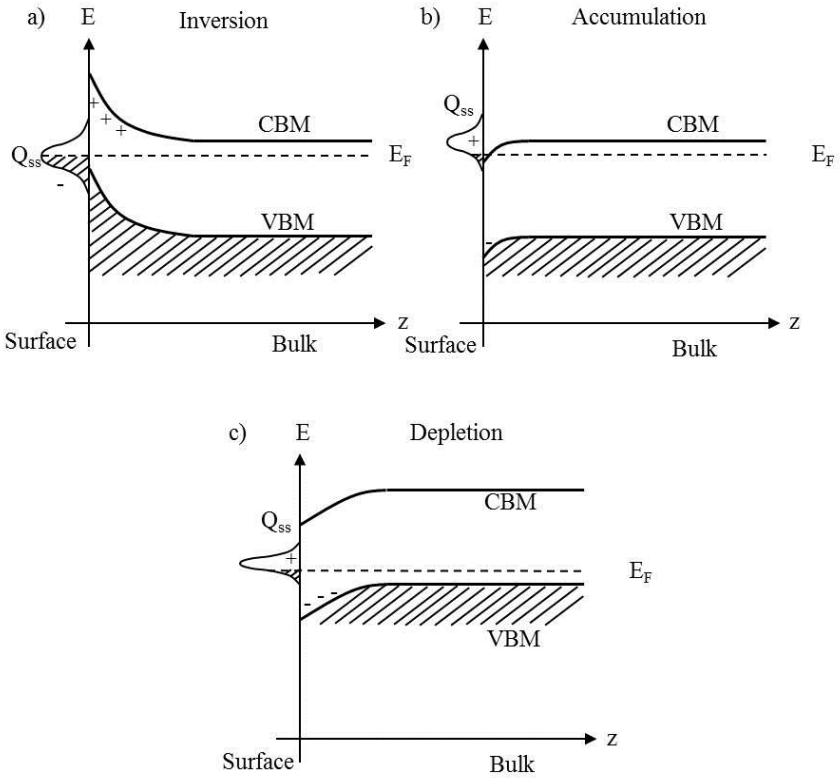

Figure 5.15 Schematic of space charge layers: (a) Inversion layer on an n-type semiconductor with acceptor type surface states, (b) accumulation layer on an n-type semiconductor with donor type surface states and (c) depletion layer on a p-type semiconductor with donor type surface states. Figures adapted from ref. [8].

Donor type surface states on n-type semiconductors (positively charged when occupied) results in an accumulation of the majority carriers near the surface, this accumulation layer is shown in Fig. 5.15 (b). A depletion layer (depletion of majority carriers, in this case, holes) for p-type semiconductors is shown in Fig. 5.15 (c).

n-type wafers are used in this thesis because the space charge layer produced by acceptor-type surface states will have stronger band bending. For p-type wafers, the VBM will be closer to E_F, thus, smaller band bending and a wider inversion layer is

necessary to maintain charge neutrality. Narrow inversion layers are necessary to get the quantization HSBs.

For In-adsorbed Si surfaces, the surface states are acceptor-type and induces upward band bending in n-type Si surfaces. This has resulted in strong upward band bending and the formation of quantized HSBs as reported for the Si(111)√7×√3-In [17].

If the same band bending is applied on the Si(110) surface, similar quantized states are expected to be observed. Schematic diagrams of the formation of the hole subband structures are shown in Fig. 5.16. The dispersion of the HSBs are shown in Fig. 5.16 (a), while the band bending, quantized energy levels, and the wavefunctions involved are shown schematically in Fig. 5.16 (b). To approximate the quantized energy levels from these inversion layers, the confining potential well can be simplified as a linear function (red dashed lines in Fig. 5.16 (c)) in the triangular potential approximation [113]. In this approximation, the potential $V(z)$ can be expressed as,

$$V(z) = eFz \qquad (43),$$

where eF is the slope of the triangular potential.

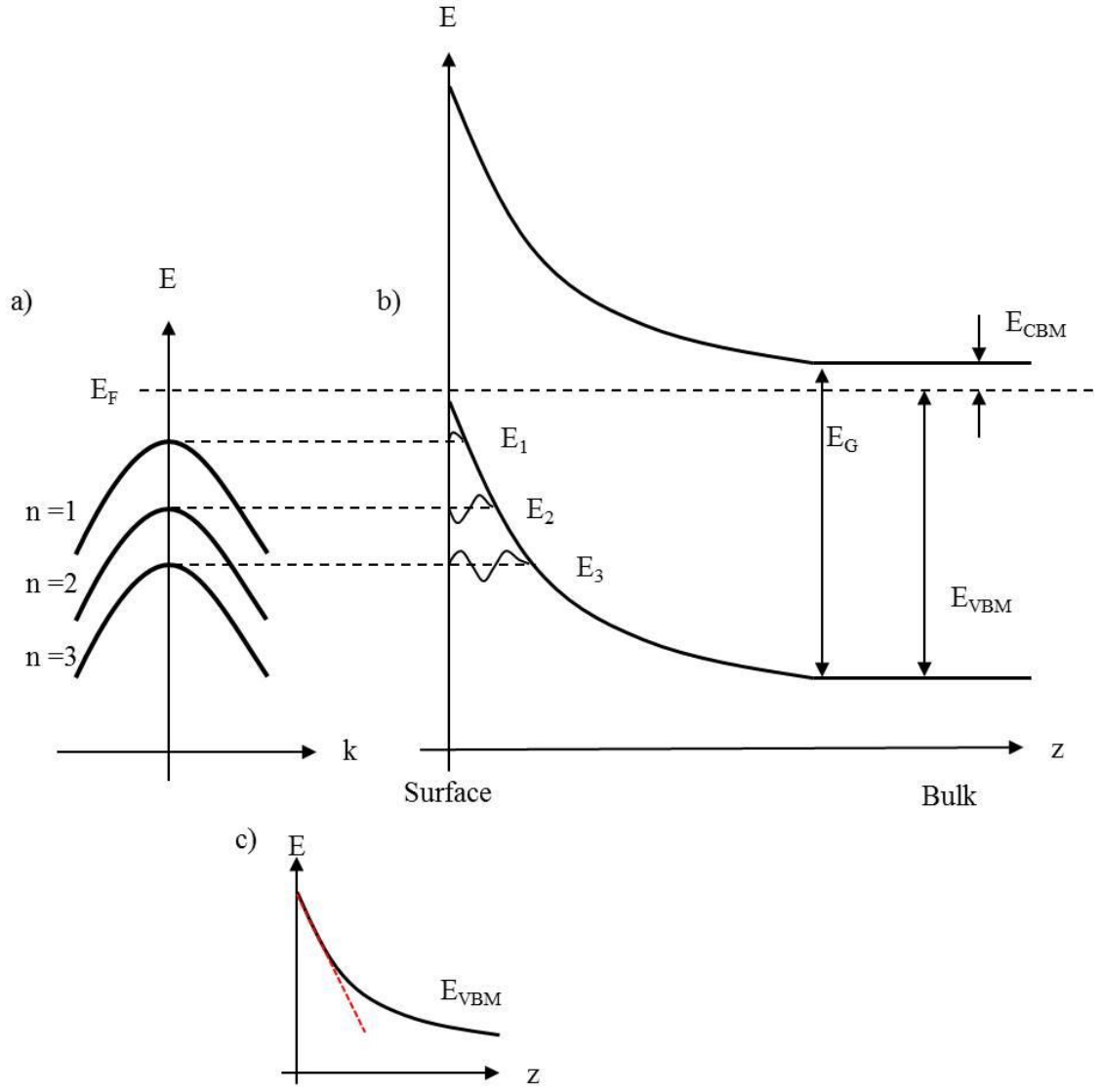

Figure 5.16 Schematic diagrams of (a) the dispersion of the hole subband structures, (b) the band bending on the surface and the quantized wave functions and (c) the triangular potential approximation (red dashed line).

From this linear potential, the quantized energy levels can be approximated as,

$$E_n = \left(\frac{\hbar^2}{2m_z^*}\right)^{1/3}\left[\frac{3\pi eF}{2}\left(n+\frac{3}{4}\right)\right]^{2/3} \qquad (44),$$

where m_z^* is the effective mass along the quantization direction (perpendicular to the surface) and n is an integer [17, 113]. From this approximation, it can be seen that the quantized energy levels of the HSBs can be affected by two factors, the effective mass m_z^* and the slope of the triangular potential eF. Table 5-3 compares the effective

masses perpendicular to the surfaces of the Si(110) and Si(111) surfaces using the $k{\cdot}p$ approximation [114], and the Luttinger parameters for Si, A = -4.28, |B| = 0.68 and $|C|^2$ = 24 [115].

Table 5-3. Effective masses perpendicular to the surfaces of the Si(110) and SiS(111) surfaces calculated from the $k{\cdot}p$ approximation.

	Si(110) [110]	**Si(111) [111]**
$\boldsymbol{m^*_{hh}}$	$0.57m_0$	$0.72m_0$
$\boldsymbol{m^*_{lh}}$	$0.15m_0$	$0.14m_0$

Eq. (44) can be expressed as,

$$E_n = \left(n+\frac{3}{4}\right)^{2/3}\left(\frac{1}{m_z^*}\right)^{1/3}\left(\frac{\hbar^2}{2}\right)^{1/3}\left[\frac{3\pi eF}{2}\right]^{2/3}$$

$$= \left(n+\tfrac{3}{4}\right)^{2/3}\left(\tfrac{1}{m_z^*}\right)^{1/3}\gamma \qquad (45),$$

where $\gamma = \left(\frac{\hbar^2}{2}\right)^{1/3}\left[\frac{3\pi eF}{2}\right]^{2/3}$. Assuming the same band bending for both surfaces (the same slope for the triangular potential), the quantized energy levels of the subbands, and the energy separations are similar. Using the heavy hole effective masses, m_z^*, in Table 5-3 for both the Si(110) and Si(111), and applying these to eq. (45), Table 5-4 shows the quantized energy levels and the energy separations for the Si(110) and Si(111) surfaces.

Table 5-4. Quantized energy levels and energy separations for the Si(110) and Si(111) surfaces using the heavy hole masses.

	Si(110)		Si(111)	
	E_n	$E_n - E_{n-1}$	E_n	$E_n - E_{n-1}$
n = 0	0.99 γ		0.91 γ	
n = 1	1.75 γ	0.76	1.61 γ	0.70
n = 2	2.36 γ	0.61	2.18 γ	0.57
n = 3	2.90 γ	0.54	2.68 γ	0.50
n = 4	3.40 γ	0.50	3.14 γ	0.46

In 2005, Takeda, *et al.,* [17] reported the experimental observation of quantized hole subbands on the Si(111)√7×√3-In. In Fig. 5.17, the shape of the inversion layer of this Si(111)√7×√3-In surface (red line), as calculated in ref. [17] is shown. The shape of the inversion layer of the Si(110)1×1-In was estimated from the energy position of the valence band maximum (V_0), and from the calculated bulk E_{CBM} and E_{VBM} [114]. Both experiments used highly doped Si wafers, 1×10^{18} cm^{-3} for the Si(111)√7×√3-In [17] and 8.5×10^{19} cm^{-3} for the Si(110)1×1-In surfaces. This similarity in the dopant concentration should result in similar widths of the inversion layers for both surfaces. From these approximations, the shape of the inversion layer for the Si(110)1×1-In surface was estimated and is shown as the blue line in Fig. 5.17.

From the shape of the inversion layers, it can be seen that the Si(111)√7×√3-In [17] exhibits a much stronger upward band bending then the surfaces reported in this thesis. Rotenberg, *et al.,* [116] reported observing a nearly ideal 2D electron gas (2DEG) on the Si(111)√7×√3-In surface, with nearly all electrons participating in the 2DEG. Aside from these metallic states, 3 more surface states (S_1-S_3) were observed below the Fermi level [116]. These metallic and nonmetallic surface states produce a highly negatively charged surface, inducing a strong upward bending.

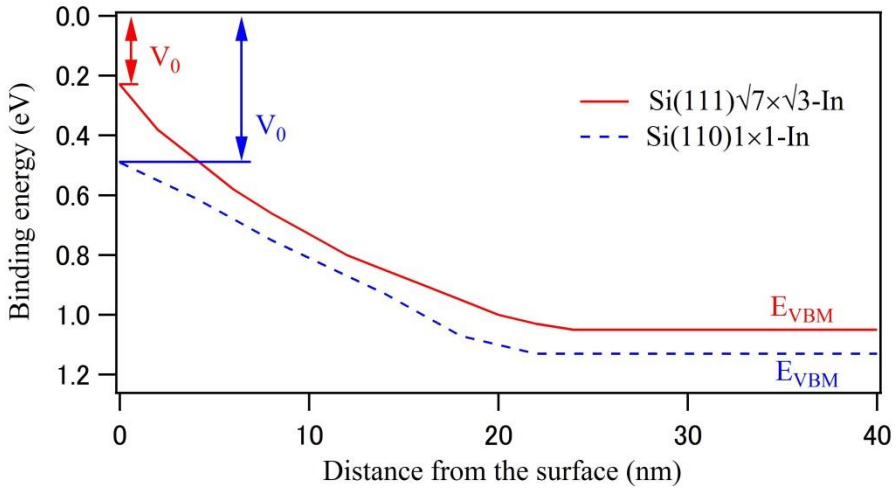

Figure 5.17. Shapes of the inversion layer of the Si(111)√7×√3-In from the calculations in ref. [17] and a schematic of the inversion layer of the Si(110)1×1-In.

From the ARPES spectra taken from the Si(110)1×1-In (Fig. 5.19), the 5 surface states observed (I_0-I_5) below the Fermi level are observed in the same energy region as the surface states (S_1-S_3) in the Si(111)√7×√3-In [116]. However, no metallic states were observed on this Si(111)1×1-In surface. Rotenberg, *et al.,* [116] concluded that nearly all the electrons (In valence and Si DB electrons) participated in the 2DEG. This 2DEG contributed significantly more to the upward band bending on the surface, explaining the stronger band bending observed on the Si(111)√7×√3-In surface.

Another factor that can affect the band bending is the surface charge concentration on the surface. The flash annealing done to prepare the clean Si(110) surface has been shown to result in the out-diffusion of dopants on As- [117, 118] and Sb- [118] doped Si wafers. This could lead to a non-uniform distribution of dopants that could affect the shape of the inversion layer on these surfaces [100, 117, 118]. Further investigations are necessary to explain absence of the HSB on the In-adsorbed Si(110) surfaces.

5.4. Conclusions

In summary, the growth and surface reconstructions of In on the Si(110) was investigated by RHEED in an attempt to clarify the conflicting reports about the phase diagram of the In/Si(110) surface. These reports were not completely reproduced in this study, where only the Si(110)7×2-In and Si(110)1×1-In surfaces were observed. These two surfaces are also the only agreement between the conflicting reports in the literature. The electronic structures of these surfaces were investigated by ARPES and a surface state derived from In-Si backbonding was observed on both the 7×2- and 1×1-In surfaces. Additional states were observed on the 1×1 surface, suggesting a possible metallic surface. Furthermore, shifts of the E_{VBM} towards the Fermi level indicate band bending on the surface, which was still too small to produce quantized hole subband structures. Results from the In 4d core-level spectroscopy suggests some possible bonding configuration for theses In-adsorbed surfaces. While these results are not enough to provide a detailed structural model for these surfaces, the results of this study provides vital information necessary for surface structure determination.

Chapter 6. Summary and conclusions

6.1. Conclusions

Recent developments in surface science and semiconductor device technology has renewed the interest on the Si(110) surface. New physics observed on low dimensional systems have made the anisotropic surface of the Si(110) surface an interesting template for one-dimensional metallic growth. Furthermore, the development of new FET device architecture, the emergence of strained-Si based FET devices, and the prospect of hybrid-orientation devices has suddenly made the Si(110) surface an interesting material for semiconductor devices. Despite all these possible applications, there is still a significant lack of understanding of the Si(110) surface. Thus, there is a need to investigate the surface and electronic structure of the Si(110) surface.

The most significant results that this study contributes are as follows: first, the previously unidentified electronic states in the projected bulk bands of the Si(110)16×2 surface were determined to be surface resonance states. It was shown through ARPES experiments that these electronic states were highly surface sensitive, disappearing or changing after the surface was modified by adsorbate-induced reconstructions. This experimental result is a significant contribution to the still on-going search for the structural model of the complicated Si(110)16×2 reconstruction. One way to verify these structural models are by comparing the results of theoretical calculations based on these models with actual experimental results.

Aside from the clean Si(110) surface, metal-adsorbed Si surfaces have also shown significant promise of hosting novel physical phenomena. Bismuth on silicon surfaces, for instance, have shown the Rashba effect, where the degeneracy of the bands is lifted even without an applied external magnetic field. In chapter 4, the first

comprehensive study of the surface and electronic structures of Bi-adsorbed Si(110) surfaces was presented. The growth and the different surface reconstructions of Bi on the Si(110) surface

were investigated by RHEED. A complete phase diagram of Bi on Si(110) was experimentally determined by studying Bi-adsorbed surfaces prepared with various metal coverage and at different substrate temperatures. Two new surface reconstructions, the Si(110)3×“4”-Bi and Si(110)3×“6”-Bi, were observed and identified by RHEED. ARPES results revealed semiconducting surfaces and the presence of electronic states that were identified as surface states derived from Bi-Si backbonding. For these surfaces, structural models that could sufficiently explain the experimental results were proposed based on RHEED, ARPES and Bi core-level spectroscopy. These surface reconstructions are proposed to be made up of rows of Bi adatoms with anisotropic structural correlation on the surface. This quasi one-dimensional model can also be adapted and used to explain similar surface reconstructions found on Si(110) surfaces adsorbed by other metals. These quasi 1D structures have the potential to host novel 1D electronic systems that could be used to study new physics.

In chapter 5, the first investigation of the electronic structure of In-adsorbed Si(110) surfaces was presented. Indium on other silicon surfaces have shown unique electronic properties, and this study provides the first experimental investigation of the electronic structure of Indium on the Si(110) surface. ARPES results on both the Si(110)7×2-In and Si(110)1×1-In surfaces showed p-type band bending, that can be used to study quantized electronic states that have already been shown on the other Si surfaces. Furthermore, In core-level spectroscopy provided information about the

bonding configuration of the Indium adatoms on these two surfaces. These are vital information needed in structural determination of these reconstructions.

6.2. Suggestions for future work

This study has investigated the surface and electronic structures of the clean, Bi-adsorbed and In-adsorbed Si(110) surfaces. However, there is still so much unknown about the Si(110) surface. Some key questions that need to be clarified include:

1.) *Verification of band structure calculations using band structures derived from ARPES experiments.*

This study provided experimental identification of surface resonance states of the Si(110)16×2 surface. A key question now is: Can the different proposed structural models for the 16×2 surface explain these surface resonances? Further experiments will be needed to completely reveal the atomic structure of this surface, and once this structure has been determined, band structure calculations can be compared to the experimental band dispersions.

2.) *Investigation of similar quasi-1D surface reconstructions on Si(110) surfaces adsorbed by other metals.*

There has been several preliminary studies on the different metal-adsorbed Si(110) surfaces. Several of these reconstructions exhibited similar diffraction patterns as the Bi-adsorbed Si(110) surfaces investigated in this thesis. STM studies have also shown the self-assembly of these metal adsorbates into zigzag chains on the Si(110) surface. Some key questions are: Do these quasi-1D structures support 1D electronic states? Can they support novel 1D phenomena such as 1D Rashba-spin splitting, the formation of charge density waves, etc.

3.) *Use of the pseudo 1D structures reported here as templates for 1D growth.*

In this thesis, it was shown that the Si(110)3×“4”-Bi and Si(110)3×“6”-Bi reconstructions form pseudo 1D structures on the surface. These surfaces can also be used as templates for 1D growth of other structures. These Bi-adsorbed surfaces are flat compared to the clean Si(110)16×2 surface and should promote 1D growth along the $[\bar{1}10]$ direction.

4.) Investigation of 2D electronic structures on Si(110) surfaces by inducing strong band bending.

It has already been shown on the Si(111) and Si(001) surfaces that by using a metal overlayer to produce an inversion layer, hole subband structures can be formed. Experimental investigations of these hole subband structure can provide significant information about carrier transport in the p-channels of future Si(110) based FET devices.

List of Publications

Academic Journals

1. Artoni Kevin Roquero Ang, Sakura Nishino Takeda and Hiroshi Daimon, "Bi induced superstructures on Si(110)", J. Vac. Sci. Technol. A., Submitted: 2016/04/19. Accepted: 2016/06/28.
2. Sakura Nishino Takeda, Haruka Kumeda, Kohei Maeda, Hiroki Momono, Harushige Nakao, Katsuyuki. Takeuchi, Artoni Kevin Roquero Ang, Tomohiro Sakata, Hiroshi Daimon, "Development of UHV Raman Spectroscopy for the Evaluation of Strain and Electronic Structure of Strained crystals." Hyomen Kagaku, **36**, (2015) 474.

Presented works

A. Presentations at international conferences

1. Artoni Kevin Roquero Ang, Sakura Nishino Takeda and Hiroshi Daimon, "Surface and electronic structure of Bi adsorbed Si(110) surfaces." 1st International Symposium of the Vacuum Society of the Philippines, Manila, Philippines, Jan. 2016.
2. Artoni Kevin Roquero Ang, Sakura Nishino Takeda and Hiroshi Daimon, "Bismuth induced superstructures on Si(110)", International Conference on the Formation of Semiconductor Interfaces 2015, Hiroshima, Japan, Nov. 2015.
3. Artoni Kevin Roquero Ang, Sakura Nishino Takeda and Hiroshi Daimon, "ARPES investigation of Si(110)"3×4"-Bi and Si(110)"3×6"-Bi",

International Conference on Electronic Structure and Spectroscopy 2015, New York, USA, Sept. 2015.

4. Artoni Kevin Roquero Ang, Sakura Nishino Takeda and Hiroshi Daimon. "RHEED and ARPES study of Si(110)"3×6"-Bi", 7th International Symposium on Surface Science, Matsue, Japan, Nov. 2014.
5. Artoni Kevin Roquero Ang, Sakura Nishino Takeda, Tomohiro Sakata and Hiroshi Daimon. "Angle resolved photoemission spectroscopy of Bi/Si(110)" 30th European Conference on Surface Science, Antalya, Turkey, Sept. 2014.

B. Presentations at Domestic Conferences

1. Artoni Kevin Roquero Ang, Sakura Nishino Takeda, Tomohiro Sakata and Hiroshi Daimon, "Bismuth on Si(110): RHEED and ARPES investigation". 2014 Japanese Physical Society Fall Meeting (JSPS Fall 2015), Nagoya, Japan, Sept. 2014

Supplementary materials

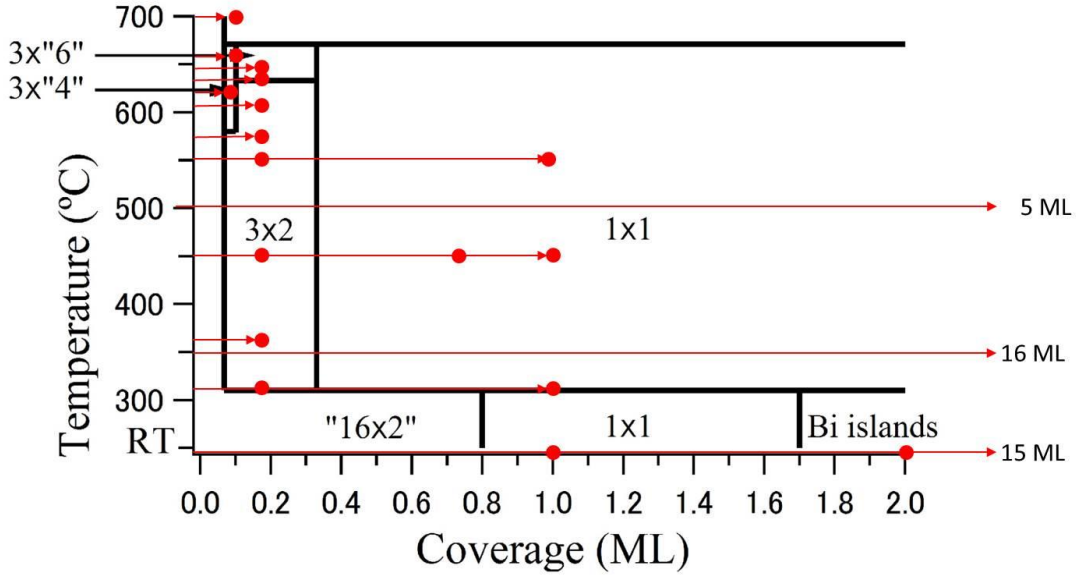

Fig. S-1. Phase diagram of Bi adsorbed on the Si(110) surface overlaid with the experimental measurement points. Red arrows indicate *in-situ* RHEED observations. Red dots indicate points on the phase diagram where the Bi deposition was stopped, the substrate temperature was lowered to RT and the surface was observed with RHEED along various incidence directions.

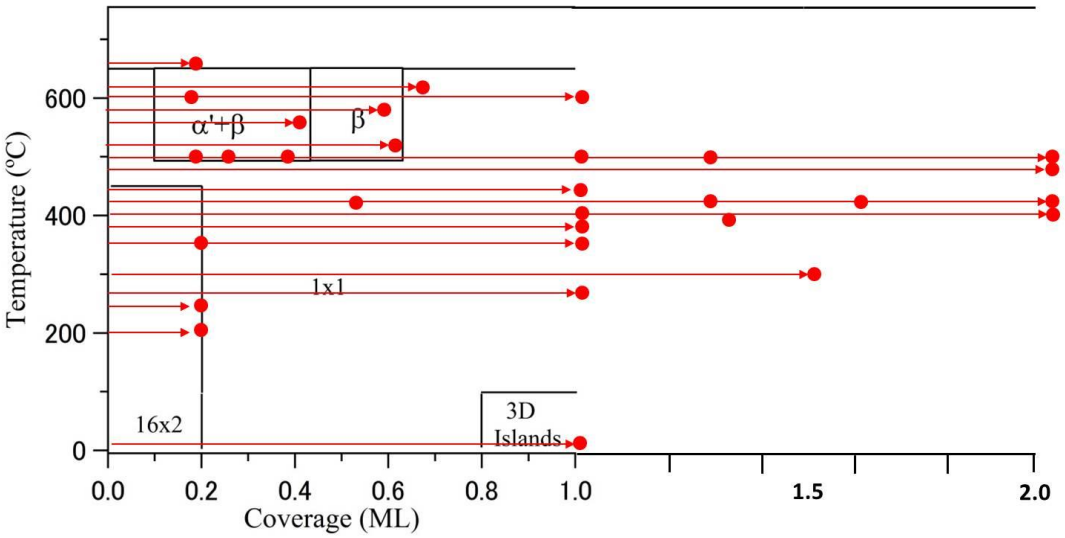

Fig. S-2. Phase diagram of In adsorbed on the Si(110) surface overlaid with the experimental measurement points. Red arrows indicate *in-situ* RHEED observations. Red dots indicate points on the phase diagram where the In deposition was stopped, the substrate temperature was lowered to RT and the surface was observed with RHEED along various incidence directions

Table S-1. A list of all two-dimensional superstructures observed on the Si(110) surface, listed by metal adsorbate. Included are the metal adsorbate species, the metal coverage, substrate temperatures during deposition, and the real and reciprocal lattice vectors. A 1994 summary can be found in the anthology "*Surface Phases on Silicon*" by Lifshits, *et al.* [15]. $\mathbf{a}$, $\mathbf{b}$ and $\mathbf{a}^*$, $\mathbf{b}^*$ are the real and reciprocal lattice vectors of the ideal Si(110)1×1 surface, while $\mathbf{a}_s$, $\mathbf{b}_s$ and $\mathbf{a}_s^*$, $\mathbf{b}_s^*$ are the real and reciprocal lattice vectors of the various surface reconstructions.

Metal	Structure	Metal coverage (ML)	Substrate temperature (°C)	Real space unit cell vectors	Reciprocal lattice vectors	Notes
	Ideal Si(110)1×1	N/A	N/A	$\mathbf{a} = \frac{a}{\sqrt{2}}(\hat{\mathrm{x}} + \hat{\mathrm{y}})$ $\mathbf{b} = a\hat{\mathrm{z}}$	$\mathbf{a}^* = 2\sqrt{2}\pi/a\,(\hat{\mathrm{x}} + \hat{\mathrm{y}})$ $\mathbf{b}^* = 2\pi/a\,\hat{\mathrm{z}}$	$a = 0.543\ nm$ See Fig. 3.1.
	Si(110) 16×2	N/A	N/A	$\mathbf{a}_s = 11\mathbf{a} + 5\mathbf{b}$ $\mathbf{b}_s = -2\mathbf{a} + 2\mathbf{b}$	$\mathbf{a}_s^* = \frac{1}{16}\mathbf{a}^* + \frac{1}{16}\mathbf{b}^*$ $\mathbf{b}_s^* = \frac{-5}{32}\mathbf{a}^* + \frac{11}{32}\mathbf{b}^*$	Double domain
Ag	$\begin{pmatrix} 9 & 3 \\ \bar{9} & 3 \end{pmatrix}$ or c(18×6) [119]	0.14-0.44	300-660	$\mathbf{a}_s = 9\mathbf{a} + 3\mathbf{b}$ $\mathbf{b}_s = -9\mathbf{a} + 3\mathbf{b}$	$\mathbf{a}_s^* = \frac{1}{3}\mathbf{a}^* + \frac{1}{12}\mathbf{b}^*$ $\mathbf{b}_s^* = \frac{1}{3}\mathbf{a}^* + \frac{1}{12}\mathbf{b}^*$	
	5×4 [119]	0.44-1.0	300-580	$\mathbf{a}_s = 5\mathbf{a}$ $\mathbf{b}_s = 4\mathbf{b}$	$\mathbf{a}_s^* = \frac{1}{5}\mathbf{a}^*$ $\mathbf{b}_s^* = \frac{1}{4}\mathbf{b}^*$	Sharp spots+ streaks
	1×2 [120]		340-500	$\mathbf{a}_s = \mathbf{a}$ $\mathbf{b}_s = 2\mathbf{b}$	$\mathbf{a}_s^* = \frac{1}{5}\mathbf{a}^*$ $\mathbf{b}_s^* = \frac{1}{2}\mathbf{b}^*$	
	$\begin{pmatrix} \bar{1} & 6 \\ \bar{7} & 0 \end{pmatrix}$ [120]		500-600	$\mathbf{a}_s = -\mathbf{a} + 6\mathbf{b}$ $\mathbf{b}_s = -7\mathbf{a}$	$\mathbf{a}_s^* = \frac{1}{6}\mathbf{a}^*$ $\mathbf{b}_s^* = \frac{1}{7}\mathbf{a}^* - \frac{1}{42}\mathbf{b}^*$	

Metal	Structure	Metal coverage (ML)	Substrate temperature (°C)	Real space unit cell vectors	Reciprocal lattice vectors	Notes
Al	$\begin{pmatrix} 3 & 0 \\ \bar{1} & 4 \end{pmatrix}$ [76]	0.16-0.3	600-700	$\mathbf{a_s} = 3\mathbf{a}$ $\mathbf{b_s} = -\mathbf{a} + 4\mathbf{b}$	$\mathbf{a_s^*} = \frac{1}{3}\mathbf{a}^* + \frac{1}{12}\mathbf{b}^*$ $\mathbf{b_s^*} = \frac{1}{4}\mathbf{b}^*$	Same as $\begin{pmatrix} 3 & 0 \\ \bar{1} & 4 \end{pmatrix}$–In and –Bi
	$\begin{pmatrix} 9 & 0 \\ \bar{2} & 1 \end{pmatrix}$ [76]	0.5	600-700	$\mathbf{a_s} = 9\mathbf{a}$ $\mathbf{b_s} = -2\mathbf{a} + \mathbf{b}$	$\mathbf{a_s^*} = \frac{1}{9}\mathbf{a}^* + \frac{2}{9}\mathbf{b}^*$ $\mathbf{b_s^*} = \mathbf{b}^*$	Double domain
	1×2 [76]	0.5-1	430-460	$\mathbf{a_s} = \mathbf{a}$ $\mathbf{b_s} = 2\mathbf{b}$	$\mathbf{a_s^*} = \mathbf{a}^*$ $\mathbf{b_s^*} = \frac{1}{2}\mathbf{b}^*$	
	1×1 [76]	0.5-2	< 430	$\mathbf{a_s} = \mathbf{a}$ $\mathbf{b_s} = \mathbf{b}$	$\mathbf{a_s^*} = \mathbf{a}^*$ $\mathbf{b_s^*} = \mathbf{b}^*$	
	$\begin{pmatrix} 3 & 3 \\ \bar{2} & 2 \end{pmatrix}$ [75]	0.6	780	$\mathbf{a_s} = 3\mathbf{a} + 3\mathbf{b}$ $\mathbf{b_s} = -2\mathbf{a} + 2\mathbf{b}$	$\mathbf{a_s^*} = \frac{1}{9}\mathbf{a}^* + \frac{2}{9}\mathbf{b}^*$ $\mathbf{b_s^*} = -\frac{1}{3}\mathbf{a}^* + \frac{1}{3}\mathbf{b}^*$	Same as $\begin{pmatrix} 9 & 0 \\ \bar{2} & 1 \end{pmatrix}$ –Al Double domain
	3×8 [75]		880	$\mathbf{a_s} = 3\mathbf{a}$ $\mathbf{b_s} = 8\mathbf{b}$	$\mathbf{a_s^*} = \frac{1}{3}\mathbf{a}^*$ $\mathbf{b_s^*} = \frac{1}{8}\mathbf{b}^*$	Same as $\begin{pmatrix} 3 & 0 \\ \bar{1} & 4 \end{pmatrix}$ –Al, –In and –Bi Double domain Sharp spots+ streaks
Au	1×2 [121]	0.08-0.28	440-970	$\mathbf{a_s} = \mathbf{a}$ $\mathbf{b_s} = 2\mathbf{b}$	$\mathbf{a_s^*} = \mathbf{a}^*$ $\mathbf{b_s^*} = \frac{1}{2}\mathbf{b}^*$	
	2×5 [121]	0.28-0.46	440-750	$\mathbf{a_s} = 2\mathbf{a}$ $\mathbf{b_s} = 5\mathbf{b}$	$\mathbf{a_s^*} = \frac{1}{2}\mathbf{a}^*$ $\mathbf{b_s^*} = \frac{1}{5}\mathbf{b}^*$	Sharp spots+ streaks [32, 121]

Metal	Structure	Metal coverage (ML)	Substrate temperature (°C)	Real space unit cell vectors	Reciprocal lattice vectors	Notes
Au	$\begin{pmatrix} 4 & 0 \\ \bar{1} & 3 \end{pmatrix}$ [121]	0.46-1.23	440-850	$\mathbf{a_s} = 4\mathbf{a}$ $\mathbf{b_s} = -\mathbf{a} + 3\mathbf{b}$	$\mathbf{a_s^*} = \frac{1}{4}\mathbf{a}^* + \frac{1}{12}\mathbf{b}^*$ $\mathbf{b_s^*} = \frac{1}{3}\mathbf{b}^*$	Double domain [32]
	1×1 [121]	0.3~	<440	$\mathbf{a_s} = \mathbf{a}$ $\mathbf{b_s} = \mathbf{b}$	$\mathbf{a_s^*} = \mathbf{a}^*$ $\mathbf{b_s^*} = \mathbf{b}^*$	
B	$\begin{pmatrix} 10 & 0 \\ \bar{2} & 1 \end{pmatrix}$ [122]	0.01-0.07	900	$\mathbf{a_s} = 10\mathbf{a}$ $\mathbf{b_s} = -2\mathbf{a} + 1\mathbf{b}$	$\mathbf{a_s^*} = \frac{1}{10}\mathbf{a}^* + \frac{1}{5}\mathbf{b}^*$ $\mathbf{b_s^*} = \mathbf{b}^*$	Annealing of highly B–doped wafers
Bi	3×2 [71]			$\mathbf{a_s} = 3\mathbf{a}$ $\mathbf{b_s} = 2\mathbf{b}$	$\mathbf{a_s^*} = \frac{1}{3}\mathbf{a}^*$ $\mathbf{b_s^*} = \frac{1}{2}\mathbf{b}^*$	
	$\begin{pmatrix} 3 & 0 \\ \bar{1} & 4 \end{pmatrix}$ or 3×"4" [Chap. 4]			$\mathbf{a_s} = 3\mathbf{a}$ $\mathbf{b_s} = -\mathbf{a} + 4\mathbf{b}$	$\mathbf{a_s^*} = \frac{1}{3}\mathbf{a}^* + \frac{1}{12}\mathbf{b}^*$ $\mathbf{b_s^*} = \frac{1}{4}\mathbf{b}^*$	Same as $\begin{pmatrix} 3 & 0 \\ \bar{1} & 4 \end{pmatrix}$–In and –Al Double domain Sharp spots+ streaks
	$\begin{pmatrix} 3 & 0 \\ \bar{1} & 6 \end{pmatrix}$ or 3×"6" [Chap. 4]			$\mathbf{a_s} = 3\mathbf{a}$ $\mathbf{b_s} = -\mathbf{a} + 6\mathbf{b}$	$\mathbf{a_s^*} = \frac{1}{3}\mathbf{a}^* + \frac{1}{18}\mathbf{b}^*$ $\mathbf{b_s^*} = \frac{1}{6}\mathbf{b}^*$	Double domain Sharp spots+ streaks
	1×1 [71]			$\mathbf{a_s} = \mathbf{a}$ $\mathbf{b_s} = \mathbf{b}$	$\mathbf{a_s^*} = \mathbf{a}^*$ $\mathbf{b_s^*} = \mathbf{b}^*$	
Ca	1×2 [123]			$\mathbf{a_s} = \mathbf{a}$ $\mathbf{b_s} = 2\mathbf{b}$	$\mathbf{a_s^*} = \mathbf{a}^*$ $\mathbf{b_s^*} = \frac{1}{2}\mathbf{b}^*$	Predicted by DFT calculations

Metal	Structure	Metal coverage (ML)	Substrate temperature (°C)	Real space unit cell vectors	Reciprocal lattice vectors	Notes
Cs	2×2 [124]	0.05-0.10		$\mathbf{a_s} = 2\mathbf{a}$ $\mathbf{b_s} = 2\mathbf{b}$	$\mathbf{a_s^*} = \frac{1}{2}\mathbf{a}^*$ $\mathbf{b_s^*} = \frac{1}{2}\mathbf{b}^*$	
	5×4 [124]	0.15-0.2		$\mathbf{a_s} = 5\mathbf{a}$ $\mathbf{b_s} = 4\mathbf{b}$	$\mathbf{a_s^*} = \frac{1}{5}\mathbf{a}^*$ $\mathbf{b_s^*} = \frac{1}{4}\mathbf{b}^*$	
	1×1 [124]	0.5~		$\mathbf{a_s} = \mathbf{a}$ $\mathbf{b_s} = \mathbf{b}$	$\mathbf{a_s^*} = \mathbf{a}^*$ $\mathbf{b_s^*} = \mathbf{b}^*$	
Ga	$\begin{pmatrix} 2 & 1 \\ \bar{3} & 3 \end{pmatrix}$ [125]	0.08-0.11	527-597	$\mathbf{a_s} = 2\mathbf{a} + \mathbf{b}$ $\mathbf{b_s} = -3\mathbf{a} + 3\mathbf{b}$	$\mathbf{a_s^*} = \frac{1}{3}\mathbf{a}^* + \frac{1}{3}\mathbf{b}^*$ $\mathbf{b_s^*} = -\frac{1}{9}\mathbf{a}^* + \frac{2}{9}\mathbf{b}^*$	Double domain
	$\begin{pmatrix} 2 & 1 \\ \bar{4} & 4 \end{pmatrix}$ [125]	0.11-0.17	482-527	$\mathbf{a_s} = 2\mathbf{a} + \mathbf{b}$ $\mathbf{b_s} = -4\mathbf{a} + 4\mathbf{b}$	$\mathbf{a_s^*} = \frac{1}{3}\mathbf{a}^* + \frac{1}{3}\mathbf{b}^*$ $\mathbf{b_s^*} = -\frac{1}{12}\mathbf{a}^* + \frac{1}{6}\mathbf{b}^*$	Double domain
Ge	$\begin{pmatrix} 10 & \bar{1} \\ 3 & 4 \end{pmatrix}$ [90, 126]	0.4-0.9 [90] 0.3-0.7 [126]	300-730 [90] 550-650 [126]	$\mathbf{a_s} = 10\mathbf{a} - \mathbf{b}$ $\mathbf{b_s} = 3\mathbf{a} + 4\mathbf{b}$	$\mathbf{a_s^*} = \frac{4}{43}\mathbf{a}^* - \frac{3}{43}\mathbf{b}^*$ $\mathbf{b_s^*} = \frac{1}{43}\mathbf{a}^* + \frac{10}{43}\mathbf{b}^*$	Double domain
	1×1 [126]	0.7-0.8	550-650	$\mathbf{a_s} = \mathbf{a}$ $\mathbf{b_s} = \mathbf{b}$	$\mathbf{a_s^*} = \mathbf{a}^*$ $\mathbf{b_s^*} = \mathbf{b}^*$	
	$\begin{pmatrix} 8 & 0 \\ 2 & 1 \end{pmatrix}$ [126]	0.8~	450-620	$\mathbf{a_s} = 8\mathbf{a}$ $\mathbf{b_s} = 2\mathbf{a} + \mathbf{b}$	$\mathbf{a_s^*} = \frac{1}{8}\mathbf{a}^* - \frac{1}{4}\mathbf{b}^*$ $\mathbf{b_s^*} = \mathbf{b}^*$	Double domain Same as $\begin{pmatrix} 2 & 3 \\ \bar{2} & 1 \end{pmatrix}$-Ge

Metal	Structure	Metal coverage (ML)	Substrate temperature (°C)	Real space unit cell vectors	Reciprocal lattice vectors	Notes
Ge	$\begin{pmatrix} 2 & 3 \\ \bar{2} & 1 \end{pmatrix}$ [90]	0.9 ~	300-730	$\mathbf{a_s} = 2\mathbf{a} + \mathbf{3b}$ $\mathbf{b_s} = -2\mathbf{a} + \mathbf{b}$	$\mathbf{a_s^*} = \frac{1}{8}\mathbf{a}^* + \frac{1}{4}\mathbf{b}^*$ $\mathbf{b_s^*} = \frac{-3}{8}\mathbf{a}^* + \frac{1}{4}\mathbf{b}^*$	Double domain Same as $\begin{pmatrix} 8 & 0 \\ 2 & 1 \end{pmatrix}$–Ge
In	3×4 or α [107]	0.02-0.2	400-440	$\mathbf{a_s} = 3\mathbf{a}$ $\mathbf{b_s} = 4\mathbf{b}$	$\mathbf{a_s^*} = \frac{1}{3}\mathbf{a}^*$ $\mathbf{b_s^*} = \frac{1}{4}\mathbf{b}^*$	
	$\begin{pmatrix} 3 & 0 \\ \bar{1} & 4 \end{pmatrix}$ or α' [77]	0.2	500~	$\mathbf{a_s} = 3\mathbf{a}$ $\mathbf{b_s} = -\mathbf{a} + 4\mathbf{b}$	$\mathbf{a_s^*} = \frac{1}{3}\mathbf{a}^* + \frac{1}{12}\mathbf{b}^*$ $\mathbf{b_s^*} = \frac{1}{4}\mathbf{b}^*$	Same as $\begin{pmatrix} 3 & 0 \\ \bar{1} & 4 \end{pmatrix}$–Bi and –Al Double domain Sharp spots+ streaks
	$\begin{pmatrix} 4 & 3 \\ \bar{2} & 2 \end{pmatrix}$ or β [77, 107]	0.2-0.35 [107] 0.47 [77]	377-427 [107] 460 [77]	$\mathbf{a_s} = 4\mathbf{a} + 3\mathbf{b}$ $\mathbf{b_s} = -2\mathbf{a} + 2\mathbf{b}$	$\mathbf{a_s^*} = \frac{1}{3}\mathbf{a}^* + \frac{1}{18}\mathbf{b}^*$ $\mathbf{b_s^*} = \frac{1}{6}\mathbf{b}^*$	Double domain Same as $\begin{pmatrix} 4 & 3 \\ \bar{2} & 2 \end{pmatrix}$–Pb, –Sn
	$\begin{pmatrix} 6 & 4 \\ \bar{3} & 2 \end{pmatrix}$ or γ [107]	0.8-4.0	377-427	$\mathbf{a_s} = 6\mathbf{a} + 4\mathbf{b}$ $\mathbf{b_s} = -3\mathbf{a} + 2\mathbf{b}$	$\mathbf{a_s^*} = \frac{1}{12}\mathbf{a}^* + \frac{1}{8}\mathbf{b}^*$ $\mathbf{b_s^*} = -\frac{1}{6}\mathbf{a}^* + \frac{1}{4}\mathbf{b}^*$	Double domain
	$\begin{pmatrix} 3 & \bar{2} \\ \bar{2} & 4 \end{pmatrix}$ or γ' [77]	0.94	460	$\mathbf{a_s} = 3\mathbf{a} - 2\mathbf{b}$ $\mathbf{b_s} = -2\mathbf{a} + 4\mathbf{b}$	$\mathbf{a_s^*} = \frac{1}{5}\mathbf{a}^* + \frac{1}{5}\mathbf{b}^*$ $\mathbf{b_s^*} = \frac{-1}{25}\mathbf{a}^* + \frac{3}{25}\mathbf{b}^*$	Double domain

Metal	Structure	Metal coverage (ML)	Substrate temperature (°C)	Real space unit cell vectors	Reciprocal lattice vectors	Notes
Ni	4×5 [22]	0.1-0.2		$\mathbf{a_s} = 4\mathbf{a}$ $\mathbf{b_s} = 5\mathbf{b}$	$\mathbf{a_s^*} = \frac{1}{4}\mathbf{a}^*$ $\mathbf{b_s^*} = \frac{1}{5}\mathbf{b}^*$	
	1×5 [22]	0.2-0.3	700	$\mathbf{a_s} = \mathbf{a}$ $\mathbf{b_s} = 5\mathbf{b}$	$\mathbf{a_s^*} = \mathbf{a}^*$ $\mathbf{b_s^*} = \frac{1}{5}\mathbf{b}^*$	
	1×2 [22]	0.3-0.5	650	$\mathbf{a_s} = \mathbf{a}$ $\mathbf{b_s} = 2\mathbf{b}$	$\mathbf{a_s^*} = \mathbf{a}^*$ $\mathbf{b_s^*} = \frac{1}{2}\mathbf{b}^*$	
	5×4 [22]	0.5-1.0	700	$\mathbf{a_s} = 5\mathbf{a}$ $\mathbf{b_s} = 4\mathbf{b}$	$\mathbf{a_s^*} = \frac{1}{5}\mathbf{a}^*$ $\mathbf{b_s^*} = \frac{1}{4}\mathbf{b}^*$	
	1×9 [22]		770	$\mathbf{a_s} = \mathbf{a}$ $\mathbf{b_s} = 9\mathbf{b}$	$\mathbf{a_s^*} = \mathbf{a}^*$ $\mathbf{b_s^*} = \frac{1}{9}\mathbf{b}^*$	
	1×7 [22]		790	$\mathbf{a_s} = \mathbf{a}$ $\mathbf{b_s} = 7\mathbf{b}$	$\mathbf{a_s^*} = \mathbf{a}^*$ $\mathbf{b_s^*} = \frac{1}{7}\mathbf{b}^*$	

Metal	Structure	Metal coverage (ML)	Substrate temperature (°C)	Real space unit cell vectors	Reciprocal lattice vectors	Notes
Pb	1×1 [104, 105]		RT [104] 270 [105]	$\mathbf{a_s} = \mathbf{a}$ $\mathbf{b_s} = \mathbf{b}$	$\mathbf{a_s^*} = \mathbf{a}^*$ $\mathbf{b_s^*} = \mathbf{b}^*$	Well defined and streaky 1×1 structures exist
	$\begin{pmatrix} 4 & 3 \\ \bar{2} & 2 \end{pmatrix}$ or "7×2" [104]	0.2-0.55	410	$\mathbf{a_s} = 4\mathbf{a} + 3\mathbf{b}$ $\mathbf{b_s} = -2\mathbf{a} + 2\mathbf{b}$	$\mathbf{a_s^*} = \frac{1}{7}\mathbf{a}^* + \frac{1}{7}\mathbf{b}^*$ $\mathbf{b_s^*} = -\frac{3}{14}\mathbf{a}^* + \frac{2}{7}\mathbf{b}^*$	Double domain Same as $\begin{pmatrix} 4 & 3 \\ \bar{2} & 2 \end{pmatrix}$ or β– In, –Sn
	4×2 [105]	0.25-0.75	150 K	$\mathbf{a_s} = 4\mathbf{a}$ $\mathbf{b_s} = 2\mathbf{b}$	$\mathbf{a_s^*} = \frac{1}{4}\mathbf{a}^*$ $\mathbf{b_s^*} = \frac{1}{2}\mathbf{b}^*$	Sharp spots+ streaks
Pt	"5×4" [91]	0.35	~750			STM results only
	"13×2" [91]	0.5-0.6	~750			STM results only
	"6×5" [33, 91]	1.0-2.0	~750			Competing ×3 and ×2 periodicities along $[\bar{1}10]$
Sb	$\begin{pmatrix} 14 & 0 \\ \bar{2} & 1 \end{pmatrix}$ [87]	<0.3	650-850	$\mathbf{a_s} = 14\mathbf{a}$ $\mathbf{b_s} = -2\mathbf{a} + \mathbf{b}$	$\mathbf{a_s^*} = \frac{1}{14}\mathbf{a}^* + \frac{1}{7}\mathbf{b}^*$ $\mathbf{b_s^*} = \mathbf{b}^*$	Double domain
	3×2-α [87]	0.5	650-850	$\mathbf{a_s} = 3\mathbf{a}$ $\mathbf{b_s} = 2\mathbf{b}$	$\mathbf{a_s^*} = \frac{1}{3}\mathbf{a}^*$ $\mathbf{b_s^*} = \frac{1}{2}\mathbf{b}^*$	
	1×2 [87]	0.85	650-850	$\mathbf{a_s} = \mathbf{a}$ $\mathbf{b_s} = 2\mathbf{b}$	$\mathbf{a_s^*} = \mathbf{a}^*$ $\mathbf{b_s^*} = \frac{1}{2}\mathbf{b}^*$	
	3×2-β [81, 87]	1	650	$\mathbf{a_s} = 3\mathbf{a}$ $\mathbf{b_s} = 2\mathbf{b}$	$\mathbf{a_s^*} = \frac{1}{3}\mathbf{a}^*$ $\mathbf{b_s^*} = \frac{1}{2}\mathbf{b}^*$	

Metal	Structure	Metal coverage (ML)	Substrate temperature (°C)	Real space unit cell vectors	Reciprocal lattice vectors	Notes
Sn	$\begin{pmatrix} 4 & 3 \\ \bar{2} & 2 \end{pmatrix}$ [90]	0.14-0.44	800	$\mathbf{a_s} = 4\mathbf{a} + 3\mathbf{b}$ $\mathbf{b_s} = -2\mathbf{a} + 2\mathbf{b}$	$\mathbf{a_s^*} = \frac{1}{7}\mathbf{a}^* + \frac{1}{7}\mathbf{b}^*$ $\mathbf{b_s^*} = -\frac{3}{14}\mathbf{a}^* + \frac{2}{7}\mathbf{b}^*$	Double domain Same as $\begin{pmatrix} 4 & 3 \\ \bar{2} & 2 \end{pmatrix}$ or β– In, –Pb
	$\begin{pmatrix} 2 & 0 \\ \bar{1} & 4 \end{pmatrix}$ [92]	0.25	730	$\mathbf{a_s} = 2\mathbf{a}$ $\mathbf{b_s} = -\mathbf{a} + 4\mathbf{b}$		STM results only
	$\begin{pmatrix} 3 & 0 \\ \bar{1} & 3 \end{pmatrix}$ [90]	0.44-0.63	800	$\mathbf{a_s} = 3\mathbf{a}$ $\mathbf{b_s} = -\mathbf{a} + 3\mathbf{b}$	$\mathbf{a_s^*} = \frac{1}{3}\mathbf{a}^* + \frac{1}{9}\mathbf{b}^*$ $\mathbf{b_s^*} = \frac{1}{3}\mathbf{b}^*$	Double domain
	$\begin{pmatrix} 3 & 3 \\ \bar{2} & 1 \end{pmatrix}$ [90]	0.63-0.92	800	$\mathbf{a_s} = 3\mathbf{a} + 3\mathbf{b}$ $\mathbf{b_s} = -2\mathbf{a} + \mathbf{b}$	$\mathbf{a_s^*} = \frac{1}{9}\mathbf{a}^* + \frac{2}{9}\mathbf{b}^*$ $\mathbf{b_s^*} = -\frac{1}{3}\mathbf{a}^* + \frac{1}{3}\mathbf{b}^*$	Double domain
	$\begin{pmatrix} 3 & 3 \\ \bar{4} & 2 \end{pmatrix}$ [92]	>0.9	620	$\mathbf{a_s} = 3\mathbf{a} + 3\mathbf{b}$ $\mathbf{b_s} = -4\mathbf{a} + 2\mathbf{b}$	$\mathbf{a_s^*} = \frac{1}{9}\mathbf{a}^* + \frac{2}{9}\mathbf{b}^*$ $\mathbf{b_s^*} = -\frac{1}{6}\mathbf{a}^* + \frac{1}{6}\mathbf{b}^*$	STM results only
	c(4×2) [92]					STM results only
Tl	1×1 [96]	1	170	$\mathbf{a_s} = \mathbf{a}$ $\mathbf{b_s} = \mathbf{b}$	$\mathbf{a_s^*} = \mathbf{a}^*$ $\mathbf{b_s^*} = \mathbf{b}^*$	

Bibliography

[1] K. Novoselov, A. Geim, S. Morozov, D. Jiang, Y. Zhang, S. Dubonos, I. Grigorieva and A. Firsov, "Electric field effect in atomically thin carbon films," *Science,* vol. 306, p. 666, 2004.

[2] E. Stolyarova, K. Rim, S. Ryu, J. Maultzsch, P. Kim, L. Brus, T. Heinz, M. Hybersten and G. Flynn, "High-resolution scanning tunneling microscopy imaging of mesoscopic graphene sheets on an insulating surface," *P. Natl. A. Sci. USA,* vol. 104, p. 9209, 2007.

[3] P. Sutter, J. Sadowski and E. Sutter, "Graphene on Pt(111); Growth and substrate interaction," *Phys. Rev. B,* vol. 80, p. 245411, 2009.

[4] A. Castro Neto, F. Guinea, N. Peres, K. Novoselov and A. Geim, "The electronic properties of graphene," *Rev. of Mod. Phys.* , vol. 81, p. 109, 2009.

[5] M. Hasan and C. Kane, "Colloquium: Topological Insulators," *Rev. of Mod. Phys.*, vol. 82, p. 3045, 2010.

[6] S.-Y. Yu, *et al.*, "Discovery of a Weyl fermion semimetal and topological Fermi arcs," *Science,* vol. 349, p. 613, 2015.

[7] C. Pauly, *et al.*, "Subnanometre-wide electron channels protected by topology," *Nat. Phys.*, vol. 11, p. 338, 2015.

[8] H. Lüth, *Solid Surfaces, Interfaces and Thin Films, 5th ed.*, Heidelberg: Springer, 2010.

[9] W. Mönch, *Semiconductor surfaces and interfaces,* Berlin: Springer-Verlag, 1995.

[10] G. Moore, "Cramming more components onto integrated circuits," *Electronics,* vol. 38, no. 8, 1965.

[11] G. Moore, "No exponential is forever: But "Forever" can be delayed," in *IEEE International Solid-State Circuits conference, Digest of Technical papers*, San Francisco, 2003.

[12] K. Takayanagi, Y. Tanishiro, S. Takahashi and M. Takahashi, "Structure analysis of Si(111)7×7 reconstructed surface by transmission electron diffraction," *Surf. Sci.*, vol. 164, p. 367, 1985.

[13] P. Mårtensson, W. Ni and G. Hansson, "Surface electronic structure of Si(111)7×7-Ge and Si(111)5×5-Ge studied with photoemission and inverse photoemission," *Phys. Rev. B,* vol. 36, p. 5974, 1987.

[14] P. Mårtensson, A. Cricenti and G. Hansson, "Photoemission study of the surface states that pin the Fermi level at Si(001)2×1 surfaces," *Phys. Rev. B,* vol. 33, p. 8855, 1986.

[15] V. Lifshits, A. Saranin and A. Zotov, *Surface Phases on Silicon: Preparation, Structures and Properties*, Chichester, England: John Wiley & Sons, Ltd., 1994.

[16] H. Yeom, S. Takeda, E. Rotenberg, I. Matsuda, K. Horikoshi, J. Schaefer, C. Lee, S. Kevan, T. Ohta, T. Nagao and S. Hasegawa, "Instability and Charge Density Wave of Metallic Quantum Chains on Silicon Surface," *Phys. Rev. Lett.*, vol. 82,

p. 4898, 1999.

[17] S. Takeda, N. Higashi and H. Daimon, "Visualization of In-plane dispersion of Hole Subbands by Photelectron Spectroscopy," *Phys. Rev. Lett.,* vol. 94, p. 037401, 2005.

[18] K. Miki, D. Bowler, J. Owen, G. Briggs and K. Sakamoto, "Atomically perfect bismuth lines on Si(001)," *Phys. Rev. B,* vol. 59, p. 14868, 1999.

[19] T. Hirahara, "The Rashba and quantum size effects in ultrathin Bi films," *J. Electron Spectrosc. Relat. Phenom.,* vol. 201, p. 98, 2015.

[20] A. Takayama, T. Sato, S. Souma, T. Oguchi and T. Takahashi, "One-dimensional Edge states with giant spin splitting in a Bismuth thin film," *Phys. Rev. Lett.,* vol. 114, p. 066402, 2015.

[21] Y. Yamamoto, S. Ino and T. Ichikawa, "Surface reconstruction on a clean Si(110) surface observed by RHEED," *Jpn. J. Appl. Phys.,* vol. 25, no. 4, 1986.

[22] Y. Yamamoto, "Superstructures Induced by Ni Adsorption on a clean Si(110) Surface Studied by Reflection High-Energy Electron Diffraction-Total Reflection Angle X-Ray Spectroscopy," *Jpn. J. Appl. Phys.,* vol. 31, no. 8, p. 2544, 1992.

[23] T. Sato, Y. Takeishi and H. Hara, "Effects of crystallographic orientation on mobility, surface state density, and noise in p-type inversion layers on oxidized Silicon surfaces," *Jpn. J. Appl. Phys.,* vol. 8, p. 588, 1969.

[24] T. Sato, Y. Takeishi, H. Hara and Y. Okamoto, "Mobility anisotropy of electrons in inversion layers on oxidized Silicon surfaces," *Phys. Rev. B,* vol. 4, p. 1950, 1971.

[25] B. Yu, *et al.*, "FinFET scaling to 10 nm gate length," *Electron devices meeting: IEDM'02,* p. 251, 2002.

[26] M. Chu, Y. Sun, U. Aghoram and S. Thompson, "Strain: A solution for higher carrier mobility in nanoscale MOSFETs," *Annu. Rev. Matr. Res. ,* vol. 39, p. 203, 2009.

[27] A. Teramoto, *et al.*, "Very high carrier mobility for high-performance CMOS on a Si(110) surface," *IEEE Transactions on Electron devices,* vol. 54, no. 6, p. 1438, 2007.

[28] H. Nakamura, "Effects of selecting channel direction in improving performance of sub-100 nm MOSFETs fabricated on (110) surface Si substrate," *Jpn. J. Appl. Phys.,* vol. 43, p. 1723, 2004.

[29] W. Cheng, A. Teramoto, M. Hirayama, S. Sugawa and T. Ohmi, "Impact of improved high-performance Si(110)-oriented metal-oxide-semiconductor field-effect transistors using acuumulation-mode fully depleted Silicon-on-insulator devices," *Jpn. J. Appl. Phys.,* vol. 45, p. 3110, 2006.

[30] R. Iijima, L. Edge, J. Bruley, V. Paruchuri and M. Takayanagi, "Intrinsic effects of the crystal orientation difference between (100) and (110) Silicon substrates on characteristics of high-k/metal gate metal-oxide-semiconductor field-effect transistors," *Jpn.J. Appl. Phys.,* vol. 50, p. 061503, 2011.

[31] Y. Yamada, A. Girard, H. Asaoka, H. Yamamoto and S.-I. Shamoto, "Single-domain Si(110)-16×2 surface fabricated by electromigration," *Physical Review B,* vol. 76, no. 153309, 2007.

[32] S. Kang, K. Kim and H. Yeom, "Electronic structure of Au-induced surface phases on Si(110): LEED and angle-resolved photoemission measurements," *Phys. Rev. B,* vol. 78, p. 075315, 2008.

[33] J. Park, S. Jung, M. Jung, H. Yamane, N. Kosugi and H. Yeom, "Self-assembled nanowires with giant Rashba spin split bands," *Phys. Rev. Lett.,* vol. 110, p. 036801 , 2013.

[34] D. Gruznev, *et al.*, "A strategy to create spin-split metallic bands on Silicon using a dense alloy layer," *Nature Scientific reports,* vol. 4, p. 4742, 2014.

[35] S. Hüfner, *Photoelectron Spectroscopy: Principles and Applications,* Berlin: Springer-Verlag, 2003.

[36] A. Damascelli, "Probing the electronic structure of complex systems by ARPES," *Phys. Scripta,* vol. T109, p. 61, 2004.

[37] S. Hüfner, S. Schmidt and F. Reinert, "Photoelectron spectroscopy-An overview," *Nucl. Instr. Meth. Phys. Res. A,* vol. 547, p. 8, 2005.

[38] Figure prepared by T. Sakata.

[39] A. Ichiyama and P. I. Cohen, Reflection High Energy Electron Diffraction, New York: Cambridge University Press, 2004.

[40] *The Vacuum Technology Book: Know how book vol II*, Asslar, Germany: Pfeiffer Vacuum GmbH, 2013.

[41] H. Yamatani, *et al.*, "Total Analysis of Surface Structure and Properties by UHV Transfer System," *Surf. Sci.,* vol. 601, pp. 5284-5288, 2007.

[42] F. Jona, "Observations of clean surfaces of Si, Ge and GaAs by low-energy electron diffraction," *IBM J. Res and develop.,* vol. 9, no. 5, 1965.

[43] H. D. Hagstrum and G. E. Becker, "Energy-level spectra of electrons at the (111), (110) and (100) surfaces of silicon and germanium by Ion-neutralization spectroscopy," *Phys. Rev. B,* vol. 8, no. 4, 1973.

[44] B. Z. Olshanetsky and A. A. Shklyaev, "Phase transitions on clean Si(110) surfaces," *Surf. Sci.*, vol. 67, no. 2, 1977.

[45] T. Ichinokawa, H. Ampo, S. Miura and A. Tamura, "Formation of surface superstructures by heat treatments on Ni-contaminted surface of Si(110)," *Phys. Rev. B,* vol. 31, no. 8, 1985.

[46] Y. Yamada, A. Girard, H. Asaoka, H. Yamamoto and S.-I. Shamoto, "Controlling the surface chirality of Si(110)," *Phys. Rev. B,* vol. 77, p. 153305, 2008.

[47] Y. Yamamoto, S.-I. Kitamura and M. Iwatsuki, "Scanning tunneling microscopy study of the 16-structure appearing on a Si(110) surface," *Jpn. J. Appl. Phys. ,* vol. 31, pp. L635-L637, 1992.

[48] Y. Yamamoto, T. Sueyoshi, T. Sato and M. Iwatsuki, "High-temperature scanning tunneling microscopy study of the phase transition of the 16-structure appearing on a Si(110) surface," *Jpn. J. Appl. Phys.,* vol. 32, pp. L552-L535, 1993.

[49] T. An, M. Yoshimura, I. Ono and K. Ueda, "Elemental structure in Si(110)-"16×2" revealed by scanning tunneling microscopy," *Phys. Rev. B,* vol. 61, p. 3006, 2000.

[50] M. Setvín, V. Brázdová, D. R. Bowler, K. Tomatsu, K. Nakatsuji, F. Komori and

K. Miki, "Electronic structure of Si(110)-(16×2) studied by scanning tunneling spectroscopy and density functional theory," *Phys. Rev. B,* vol. 84, p. 115317, 2011.

[51] A. Stekolnikov, J. Furthmüller and F. Beschstedt, "Structural elements on reconstructed Si ang Ge(110) surfaces," *Phys. Rev. B,* vol. 70, p. 045305, 2004.

[52] A. Cricenti, B. Nesterenko, P. Perfetti, G. LeLay and C. Sebenne, "Electronic states of a clean Si(110)16×2 surface studied by angle resolved photoemission and surface differential reflectivity," *J. Vac. Sci. Technol. A,* vol. 14, p. 2448, 1996.

[53] N. Kim, Y. Kim, C.-Y. Park, H. Yeom, H. Koh, E. Rotenberg and J. Ahn, "High-resolution photoemission spectroscopy of the single-domain Si(110)-16×2 surface," *Phys. Rev. B,* vol. 75, p. 125309, 2007.

[54] K. Sakamoto, M. Setvin, K. Mawatari, P. Eriksson, K. Miki and R. Uhrberg, "Electronic structure of the Si(110)-(16×2) surface: High-resolution ARPES and STM investigation," *Phys. Rev. B,* vol. 79, p. 045304, 2009.

[55] A. Stekolnikov, J. Furthmüller and F. Bechstedt, "Long-range surface reconstruction: Si(110)-(16×2)," *Phys. Rev. Lett.,* vol. 93, p. 13, 2004.

[56] E. Ferraro, C. Hogan, M. Palummo and R. Del Sole, "Optical properties of the long range Si(110)-(16×2) reconstruction from first principles," *Phys. Status Solidi B,* vol. 249, p. 1148, 2012.

[57] Y. Yokoyama, H. Asaoka, A. Sinsarp and M. Sasaki, "One-dimensional nanotemplate structure of a Si(110) substrate," *e-J. Surf. Sci. and Nanotechnol.,* vol. 10, p. 509, 2012.

[58] I. Ivanov, A. Mazur and J. Pollmann, "The ideal (111), (110) and (100) surfaces of Si, Ge and GaAs; A comparison of their electronic structure," *Surf. Sci.,* vol. 92, no. 2-3, p. 365, 1980.

[59] 山中佑一郎, "角度分解光電子分光法による Pb 吸着 Si(110)表面近傍の電子状態測定," MS thesis. Nara Institute of Science and Technology, 2010.

[60] P. Hofmann, "The Surfaces of Bismuth: Structural and electronic properties," *Prog. Surf. Sci.,* vol. 81, p. 191, 2006.

[61] T. Hirahara, G. Bihlmayer, Y. Sakamoto, M. Yamada, H. Miyazaki, S.-I. Kimura, S. Blugel and S. Hasegawa, "Interfacing 2D and 3D Topological insulators: Bi(111) bilayer on Bi_2Te_3," *Phys. Rev. Lett.,* vol. 107, p. 166801, 2011.

[62] Y. Liu and R. Allen, "Electronic structure of the semimetals Bi and Sb," *Phys. Rev. B ,* vol. 52, p. 1566, 1995.

[63] X. Gonze, J.-P. Michenaud and J.-P. Vigneron, "First-principles study of As, Sb and Bi electronic properties," *Phys. Rev. B,* vol. 41, p. 11827, 1990.

[64] Y. Koroteev, G. Bihlmayer, J. Gayone, E. Chulkov, S. Blügel, P. Echenique and P. Hofmann, "Strong Spin-Orbit Splitting on Bi Surfaces," *Phys. Rev. Lett. ,* vol. 93, p. 046403, 2004.

[65] L.V. Bondarenko, *et al.,* "Large spin splitting of metallic surface-state bands at adsorbate-modified gold/silicon surfaces," *Sci. Rep.,* vol. 3, p. 01826, 2013.

[66] S. LaShell, B. A. McDougall and E. Jensen, "Spin splitting of an Au(111) surface

state band observed with angle resolved photoelectron spectroscopy," *Phys. Rev. Lett.,* vol. 77, p. 3419, 1996.

[67] H.-J. Kim and J.-H. Cho, "Giant spin-orbit-inducd spin splitting in Bi zigzag chains on GaAs(110)," *Phys. Rev. B,* vol. 92, p. 085303, 2015.

[68] K. Sakamoto, *et al.*, "Peculiar Rashba splitting originating from the two-dimensional symmetry of the surface," *Phys. Rev. Lett.,* vol. 103, p. 156801, 2009.

[69] R. M. Lutchyn, J. Sau and S. Das Sarma, "Majorana Fermions and a topological phase transition in semiconductor-superconductor heterostructures," *Phys. Rev. Lett. ,* vol. 105, p. 077001, 2010.

[70] Y. Oreg, G. Refael and F. von Oppen, "Helical liquids and Majorana bound states in quantum wells," *Phys. Rev. Lett.,* vol. 105, p. 177002, 2010.

[71] T. Oyama, S. Ohi, A. Kawazu and G. Tominaga, "Adsorption of Bismuth on Si(110) Surfaces," *Surf. Sci.,* vol. 109, p. 82, 1981.

[72] H. Sakama, A. Kawazu, T. Sueyoshi, T. Sato and M. Iwatsuki, "Adsorption of Bismuth on Si(110) Surfaces Studied by Scanning Tunneling Microscopy," *Jpn. J. Appl. Phys.,* vol. 32, p. 2929, 1993.

[73] H. Sakama and A. Kawazu, "The structural properties of Si(110)1×1 surfaces.," *Surf. Sci.,* vol. 342, p. 199, 1995.

[74] T. Nagao, J. Sadowski, M. Saito, S. Yaginuma, Y. Fujikawa, T. Kogure, T. Ohno, Y. Hasegawa, S. Hasegawa and T. Sakurai, "Nanofilm Allotrope and Phase Transformation of Ultrathin Bi Film on Si(111)7×7," *Phys. Rev. Lett.,* vol. 93, p. 105501, 2004.

[75] Y. Yamamoto, "Reflection High Energy Electron Diffraction Study of Superstructures Induced on a Si(110) Surface by Al Adsorption," *Jpn. J. Appl. Phys. ,* vol. 31, p. L53, 1992.

[76] A. Zotov, E. Khramstova, V. Lifshits, A. Kharchenko, S. Ryzhkov and A. Demidchik, "Growth of extra-thin ordered aluminum films on Si(110) surfaces," *Surf. Sci. Lett.,* vol. 277, p. L77, 1992.

[77] T. Ichikawa and T. Waragaya, "Indium-induced superstructures formed on Si(110) surfaces," *Appl. Surf. Sci. ,* vol. 256, p. 1136, 2009.

[78] H. Daimon, C. Chung, S. Ino and Y. Watanabe, "A study of Si(111)5×2-Au structures by Li adsoprtion and their coadsorbed superstructures," *Surf. Sci.,* vol. 235, p. 142, 1990.

[79] A. Cricenti, G. LeLay, B. Nesterenko, P. Perfetti and C. Sebenne, "Si(110)2×3-Sb surface studied with angle-resolved photoemission," *J. Vac. Sci. Technol. A,* vol. 15, p. 133, 1997.

[80] A. Cricenti, C. Ottaviani, C. Comicioli and P. Perfetti, "Sb/Si(110)2×3 surface studied by high-resolution Si 2p core-level photoemission spectroscopy," *Phys. Rev. B,* vol. 58, p. 7086, 1998.

[81] A. Cricenti, P. Perfetti, G. Le Lay, J. Zeysing, G. Falkenberg, L. Seehofer and L. Johnson, "Sb/Si(110)2×3 Surface Studied with Scanning Tunneling Microscopy: Evidence for Adatom Reconstruction," *Phys. Rev. B,* vol. 60, p. 13280, 1999.

[82] N. Takeuchi, "First-Principles Calculations of the Si(110)(2×3)Sb Surface," *Phys.*

Rev. B, vol. 61, p. 16704, 2000.

[83] Y. Kim, J. Kim, C. Hwang, S. Shrestha and C. Park, "Angle-resolved ultraviolet photoelectron spectroscopy study of the Si(111)α√3×√3-Bi surface," *Surf. Sci.*, vol. 498, p. 116, 2002.

[84] J. Nicholls, P. Martensson and G. Hansson, "Surface states on Si(111)√3x√3-In: Experiment and Theory," *Phys. Rev. B*, vol. 32, p. 1333, 1985.

[85] J. Northrup, "SI(111)√3×√3-Al: An adatom-induced reconstruction," *Phys. Rev. Lett.*, vol. 53, p. 684, 1984.

[86] H.-J. Kim, *Private communication (collaborator)*, Korea Institute for Advanced Study.

[87] A. Zotov, V. Lifshits and A. Demidchik, "Ordered surface phases in Sb/Si(110) systems," *Surf. Sci. Lett.*, vol. 274, p. L583, 1992.

[88] A. Huitzil-Tepanecati, G. Cocoletzi and N. Takeuchi, "Ab Initio Study of the Adsorption of Antimony and Arsenic on the Si(110) Surface," *Thin Solid Films*, vol. 519, p. 265, 2010.

[89] J. Joyce, J. Anderson, M. Nelson and G. Lapeyre, "Growth morphology and electronic structure of the Bi/GaAs(110) interface," *Phys. Rev. B*, vol. 40, p. 10412, 1989.

[90] Y. Yamamoto, "RHEED-TRAXS study of superstructures inducd by Ge and Sn adsorption on a Si(110) surface," *Surf. Sci.*, vol. 281, p. 253, 1993.

[91] A. Visikovskiy, M. Yoshimura and K. Ueda, "Pt-induced structures on Si(110) studied by STM," *Appl. Surf. Sci.*, vol. 254, p. 7626, 2008.

[92] T. An, M. Yoshimura and K. Ueda, "Scanning tunneling microscopy on Sn/Si(110) system," *Appl. Surf. Sci.*, Vols. 130-132, p. 118, 1998.

[93] Y. Ishikawa, K. Yazaki and I. Nakamichi, "The diffusion of Bismuth in Silicon," *Jpn. J. Appl. Phys.*, vol. 28, p. 1272, 1989.

[94] C. Fuller and J. Ditzenberger, "Diffusion of donor and acceptor elements in Silicon," *J. Appl. Phys.*, vol. 27, p. 544, 1956.

[95] G. Bihlmayer, S. Blügel and E. Chulkov, "Enhanced Rashba spin-oribt splitting in Bi/Ag(111) and Pb/Ag(111) surface alloys from first principles," *Phys. Rev. B*, vol. 75, p. 195414, 2007.

[96] E. Annese, *et. al.*, "Nonvortical Rashba Spin Structure on a Surface with C1h Symmetry," *Phys. Rev. Lett.*, vol. 117, p. 016803, 2016.

[97] J.-L. Li, X.-J. Liang, J.-F. Jia, X. Liu, J.-Z. Wang, E.-G. Wang and Q.-K. Xue, "Spontaneous formation of ordered Indium nanowire arrays on Si(001)", *Appl. Phys. Lett.* vol. 79, p. 2826, 2001.

[98] V. Kotlyar, A. Zotov, A. Saranin, E. Chukurov, T. Kasyanova, M. Cherevik, I. Pisarenko, H. Okado, M. Katayama, K. Oura and V. Lifshits, "Doping of Magic Nanoclusters in the submonolayer In/Si(100) system," *Phys. Rev. Lett.*, vol. 91, p. 026104, 2003.

[99] S. Cheon, T.-H. Kim, S.-H. Lee and H. Yeom, "Chiral solitons in a coupled double Peierls chain," *Science*, vol. 350, p. 182, 2015.

[100] M. Morita, S. Takeda, M. Yoshikawa, A. Kuwako, Y. Kato and H. Daimon,

"ARPES measurements on Si(111) hole subband induced by Pb and Ga adsorption," *Appl. Surf. Sci.,* vol. 254, p. 7872, 2008.

[101] S. Takeda, A. Kuwako, M. Nishide and H. Daimon, "Disentangling hole subbands dispersion in Si(111): In- and out-of-plane effective masses and anisotropy," *Phys. Rev. B,* vol. 93, p. 125418, 2016.

[102] Y. Tanigawa, S. Takeda, M. Morita, T. Ohsugi, Y. Kato, H. Daimon, M. Yoshimaru and T. Imamura, "Hole subband dispersion in space charge layers in Pb/Si(001) surfaces measured by Angle-resolevd photoelectron spectroscopy," *e-J. Surf. Sci. and Nanotechnol.,* vol. 7, p. 641, 2009.

[103] S. Takeda, N. Higashi and H. Daimon, "Effect of surface carrier concentration on valence subbands on Si(111) p-type inversion layers: Angle-resolved photoemission spectroscopy," *Phys. Rev. B,* vol. 82, p. 035318, 2010.

[104] H. Oyama and T. Ichikawa, "Structural study of reconstructions at Si(110)-Pb surfaces," *Surf. Sci.,* Vols. 357-358, p. 476, 1996.

[105] Y. Kim, J. Ahn, E. Cho, K.-S. An, H. Yeom, H. Koh, E. Rotenberg and C. Park, "Order-disorder phase transition on the Pb-adsorbed Si(110) surface," *Surf. Sci. Lett.,* vol. 596, p. L325, 2005.

[106] M. Kopciuszyński, R. Zdyb, P. Nita, M. Dachniewicz and P. Dyniec, "Quasi one-dimensional lead ribbons on the Si(110) surface," *Appl. Surf. Sci.,* vol. 373, p. 8, 2016.

[107] H. Sakama, K. Watanabe and A. Kawazu, "Structure of Indium-adsorbed Si(110) surface," *Surf. Sci.* , vol. 298, p. 63, 1993.

[108] D. Vlachos, M. Kamaratos, S. Foulias, F. Bondino, E. Magnano and M. Malvestuto, "Indium growth on reconsctured Si(111)√3×√3 and 4×1 In surfaces," *J. Phys. Chem. C,* vol. 114, p. 17693, 2010.

[109] E. Landemark, C. Karlsson and R. Uhrgberg, "Ideal unreconstructed hydrogen termination of the Si(111) surface obtained by hydrogen exposure of the √3×√3-In surface," *Phys. Rev. B,* vol. 44, p. 1951, 1991.

[110] J. Nakamura, S. Watanabe and M. Aono, "Anisotropic electronic structure of the Si(111)-4x1 In surface," *Phys. Rev. B,* vol. 63, p. 193307, 2001.

[111] S. Doniach and M. Sunjic, "Many-electron singularity in X-ray photoemission and x-ray spectra from metals," *J. Phys. C: Solid state phys.*, vol. 3, p. 285, 1970.

[112] A. Thompson, *et al., Center for X-ray Optics and Advanced light source: X-ray data booklet*, Berkeley, California: Lawrence Berkeley National Laboratory, University of California, 2009.

[113] T. Ando, A. Fowler and F. Stern, "Electronic properties of two-dimensional systems," *Rev. of Mod. Phys.* , vol. 54, p. 437, 1982.

[114] C. Kittel, *Introduction to Solid State Physics, 8th ed.*, New Jersey: John Wiley & Sons, Inc., 2005.

[115] P. Yu and M. Cardona, *Fundamentals of Semiconductors: Physics and Materials Properties, 4th ed.*, Heidelberg: Springer, 2010.

[116] E. Rotenberg, H. Koh, K. Rossnagel, H. Yeom, J. Schafer, B. Krenzer, M. Rocha and S. Kevan, "Indium √7×√3 on Si(111): A nearly free electron metal in two

dimensions," *Phys. Rev. Lett.,* vol. 91, p. 246404, 2003.

[117] T. Sakata, S. Takeda, N. Idayu Ayob and H. Daimon, "Effect of the flash annealing on the impurity distribution and the electronc structure in the inversion layer," *e-J. Surf. Sci. Nanotechnol.,* vol. 13, p. 75, 2015.

[118] N. Idayu Ayob, S. Takeda, T. Sakata, M. Yoshikawa, M. Morita and H. Daimon, "Unusual energy separation of subbands in Si(111) p-channels induced by In adsorption," *Jpn. J. Appl. Phys.,* vol. 54, pp. 065702-1, 2015.

[119] Y. Yamamoto, "Observation of Superstructures Induced by Ag Adsorption on a Si(110) Surface," *Jpn. J. Appl. Phys.,* vol. 31, no. 7, pp. 2241-2242, 1992.

[120] E.-S. Cho, H. Hur, N.-H. Kim, J.-Y. Baik, J.-Y. Kim, K.-S. An, H.-S. Lee, C.-Y. Park and S.-B. Lee, "Phases of Ag-adsorbed Si surfaces studied by low energy electron diffraction and Auger electron spectroscopy," *Jpn. J. Appl. Phys.* , vol. 42, 2003.

[121] Y. Yamamoto, " RHEED-TRAXS study of superstructures induced by Au on a Si(110) surface," *Surf. Sci.,* vol. 271, p. 407, 1992.

[122] A. Zotov, S. Ryzhkov and V. Lifshits, "Formation of ordered surface phases in submonolayer Bi/Si(110) and (Al, B)/Si(110) systems," *Surf. Sci. Lett.,* vol. 295, p. L1005, 1993.

[123] A. Alzharani, "Theoretical investivation of atomic structure and electronic properties of Ca/Si(110)-(2×1) reconstruction," *Thin Solid Films,* vol. 519, p. 5467, 2011.

[124] E. Michel, V. Eteläniemi and G. Materlik, "The adsorption geometry of Cs on Si(110)," *Appl. Surf. Sci.,* Vols. 56-58, p. 457, 1992.

[125] H. Sakama and A. Kawazu, "Adsorption of gallium on Si(110) surfaces," *Appl. Surf. Sci.,* Vols. 60-61, p. 159, 1992.

[126] S. Miura, K. Kato, T. Ide and T. Ichinokawa, "Formation of superstructures in Ge-deposited surfaces of Si(110) by annealing," *Surf. Sci.,* vol. 191, p. 259, 1987.

Acknowledgements

I would like to thank the following people for their various help and contributions to this thesis.

First and foremost, I'd like to thank my principal supervisor, Prof. Hiroshi Daimon, who provided valuable guidance throughout this study and for giving me the opportunity to do this research, for being kind, patient and always available for discussions despite his busy schedule. His keen attention to even the smallest detail has greatly influenced how I conduct my research, how I write and even how I live my life outside the laboratory.

I would also like to express my sincere gratitude to Asst. Prof. Sakura Takeda, who provided the initial idea for the topic of this thesis and for supervising every step of this thesis, for all the discussions about the data and possible next steps in the experiments and for all the random discussions we have had throughout my stay in the laboratory.

I am also very grateful to the other members of my thesis supervisory committee, Prof. Jun Ohta and Assoc. Prof. Yasuaki Ishikawa for providing valuable insights and comments to improve this thesis.

I would also like to thank the other members of our laboratory, Assoc. Prof. K. Hattori, Assoc. Prof. F. Matsui, Asst. Prof. M. Taguchi and Asst. Prof. H. Matsuda, for their valuable comments about my thesis and for their various help throughout this PhD study.

I would also like to thank the Japanese government Ministry of Education, Culture, Sports, Science and Technology (MEXT) for the scholarship grant, and the Murata Science Foundation for the International travel grant.

I would like to thank Dr. H-J. Kim of the Korea Institute for Advance Study for the DFT calculations of the band structure of the Si(110)3x2-Bi surface and his valuable insights.

I am also very grateful to Dr. T. Sakata for his tremendous help and patience when I first arrived in the laboratory as an intern, and later on as a student. He has helped me tremendously with everything, from government and bank related paperwork, to teaching me how to use the equipment in the laboratory and the various data analysis methods and software used in this thesis.

I am also very thankful for all the help of the Mr. T. Nakano and everyone in the International Student Affairs section of our university for all their help in my adjustment to life in Japan. I am also very grateful to Ms. H. Nakatani and everyone in the Graduate School of Materials Science office, and Ms. M. Nagata of our laboratory for all their various assistance.

I would also like to thank all the current students and the alumni of the Surface and Materials Science laboratory. Everyone has been of great help, from small things like Japanese-English translations to assistance in electrical and mechanical repairs and maintenance of the UHV transfer system. It has been great working with all of you.

I also want to especially thank all the past and current members of the Scienta group of our laboratory:

- H. Kumeda, K. Kitagawa and K. Kokui for their great assistance during my internship in the lab before my PhD and during the first few months of my PhD.
- H. Momono, H. Nakao, K. Maeda, and K. Takeuchi for their great assistance in maintaining the Scienta and Taiyo-1 chambers.
- K. Irie for our discussions about Bi deposition and his work in the calibration of the Bi and indium deposition sources.
- T. Ebato, M. Yoneda for their great help in maintaining the chambers and taking some of my lab responsibilities when I was writing my paper and this thesis.
- And the new students in our group, for their great help in the maintenance of the Scienta chamber.

I would also like to thank all my friends in NAIST for helping keep me sane during these 3 years by allowing me to maintain an appropriate life-work balance. I'd like to especially thank the other Filipino students in NAIST, for helping me in the transition into this university and being my family away from my family.

Finally, I would like to thank my family for being supportive and patient with me.